Low-Cost Interrogation of Optical Fibre Bragg Grating Sensors

Andrew Stuart Main
Doctor of Philosophy

Aston University
November 2007

Aston University

Low-Cost Interrogation of Optical Fibre Bragg Grating Sensors

Andrew Stuart Main
November 2007

The aim of the work described in this thesis was to investigate and devise low cost methods of interrogating fibre Bragg grating sensors. Through the application of novel signal processing techniques we are able to measure physical measurands with both high accuracy and low noise susceptibility.

The first interrogation scheme is based upon a CCD spectrometer. We compare different algorithms for resolving the Bragg wavelength from a low resolution discrete representation of the reflected spectrum, and present optimal processing methods for providing a high integrity measurement from the reflection image.

Our second sensing scheme uses a novel network of sensors to measure the distributive strain response of a mechanical system. Using neural network processing methods we demonstrate the measurement capabilities of a scalable low-cost fibre Bragg grating sensor network. This network has been shown to be comparable with the performance of existing fibre Bragg grating sensing techniques, at a greatly reduced implementation cost.

Keywords

Fibre Bragg grating sensors, Neural Networks, Distributive Tactile Sensing

Acknowledgements

I would like to thank the Engineering and Physical Sciences Research Council and the Smart Optics Faraday Partnership for funding this PhD, and the Royal Academy of Engineering for financial assistance towards overseas travel.

I would particularly like to thank my supervisor Dr David Webb for his continuous advice and guidance throughout the course of this PhD, and Professor Ian Bennion for his encouragement in instigating this PhD in the first place.

My thanks also are extended to the various members of the Photonics Research Group at Aston University for continued support, advice, and stimulating discussion. In particular I must single out Dr Tom Allsop who has been a good friend and sounding board throughout the course of this PhD. Thanks must also be paid to Mr Bert Biggs whose dedication ensures world class laboratory facilities, and Mr Richard Reeves who has helped beyond the call of duty on numerous occasions.

To my parents who have always supported my decisions in life, and have helped me at each and every step.

It is my wife Priyanka who deserves the most thanks. Her continued and unending support and belief forms the foundation of this thesis, and without this I would have never have made it this far.

Contents

List of Figures

List of Tables

Chapter 1

Introduction

The advantages the fibre optic sensing discipline has over more mature measurement methods are the inherent immunity to electromagnetic interference, the size and weight of devices, the high sensitivity, and the ease of multiplexing sensors together [6].

The fibre Bragg grating has been at the forefront of fibre optic sensing for many years due to the ease of manufacture, small physical size, inherent multiplexing capabilities, and near linear measurement response to both temperature and strain [7].

However fibre optic sensing remains prohibitively expensive for many applications, and is typically only marketable in niche applications where conventional sensing methods are inadequate or inoperable. However in application areas operating in large electromagnetic fields or flammable atmospheres, or those requiring large numbers of light weight sensors, or for high sensitivity biomedical and chemical applications, fibre optic sensing is a suitable and appealing technology.

In order to open this technology to fresh markets and compete with established conventional on a level plain a concerted effort is required to reduce the cost of implementation. The fundamental objective of the research work described in this thesis is to explore and devise fibre Bragg grating based sensing systems that are low in implementation cost. By exploiting commercial 'off-the shelf' equipment and applying novel processing techniques

we aim to reduce average implementation cost whilst retain the high resolution, stability, and integrity expected of such devices.

1.1 Thesis Outline

Chapter 2 introduces the theory of fibre Bragg gratings, discussing underlying principles and how we can design and predict their behaviour. We present ways to fabricate them, specifically focussing on UV interference pattern based methods and how this inscription can be enhanced. We discuss issues relating to device longevity with specific focus on reliability and stability for temperature sensing applications. Finally we present their application as sensors, their mode of operation, and typical system topologies in use.

Chapter 3 outlines concepts and general methods behind machine learning and function approximation. Such methods are used as tools throughout the work contained within this thesis and this chapter aims to clarify the underlying processes and philosophy behind them.

Chapter 4 presents the underlying background work behind the creation of a custom commercial temperature measurement system for an electricity generator. This project was commissioned by ALSTOM (Switzerland) Ltd to create a low cost stable and reliable turnkey measurement system that provided sufficient flexibility for the development of integrated temperature monitoring within the stator assembly of their generator products. In order to provide such a device we designed a system employing a CCD spectrometer to measure the reflection spectra from a series of fibre Bragg gratings separated by wavelength. Given the relatively low resolution measured spectrum we investigated the application of image processing techniques to enhance resolution and increase stability and noise suppression. Initially focussing on the evaluation of known methods we then used the results of our analysis to evolve the techniques and increase both reliability and stability.

In Chapter 5 we investigate the discipline of Distributive Tactile Sensing. We introduce the philosophy behind the concept compared to competitive techniques, and we describe methods of implementation. We then describe a proof of principle study where we apply this philosophy to a distributive fibre Bragg grating sensor system, developing a novel low cost scaleable architecture we name an Overlapping Grating Sensor Network (OGSN).

Chapter 6 focuses upon evaluating the novel OGSN distributive architecture and developing techniques to aid its implementation. We simplify the design to an easily analysable system before performing both simulative and experimental characterisation to determine system performance and identify implementation philosophy.

Chapter 7 finishes the thesis with a summary and suggestions for future work.

Chapter 2

Fibre Bragg Grating Sensors

Fibre Bragg gratings (FBGs) were first discovered by Hill et al. [8] alongside the discovery of fibre photosensitivity. These two simultaneous discoveries have transformed modern fibre optics, and decades later still provides both novel research and commercial opportunities [4, 7, 9, 5, 6].

Even in this very early work the importance for physical sensing applications was realised, and FBGs have been and continue to be used in a wide range of sensing roles.

This chapter focuses upon introducing the devices and the theory behind them. We start by presenting the theory behind them. We then look at how they are made. Finally we look at their use as sensors, and the systems they can be employed in.

2.1 Fibre Bragg Grating Theory

A fibre Bragg grating (FBG) is a region of periodic refractive index modulation within the core of an optical fibre. It can be expressed as [10]:

$$\delta n_{\text{eff}}(z) = \overline{\delta n_{\text{eff}}}(z)\left(1 + v\cos\left[\frac{2\pi}{\Lambda}z + \phi(z)\right]\right) \tag{2.1}$$

Where $\delta n_{\text{eff}}(z)$ is the effective refractive index change with respect to position z, v is the fringe visibility, Λ the modulation period, and ϕ is the chirp or deviation from this period.

Light propagating in the fibre core is scattered by each grating plane, each contributing a very weak reflection back down the core of the fibre. The cumulative reflection from the entire grating consists of light with a phase relative to the grating's periodicity. Light that does not match the periodicity of the structure is cancelled out by the phase mismatch. This creates dominant reflections at specific resonant wavelengths matching this condition, known as the Bragg condition, given as:

$$\lambda_B = \frac{2n_{\text{eff}}\Lambda}{m} \quad \text{for } m = 1, 2, 3 \ldots \tag{2.2}$$

Where λ_B denotes the Bragg wavelength, and m denotes the phase multiple (also known as the grating order).

This *'multiple-mirror'* analogy helps to illustrate another key attribute of fibre Bragg gratings; they have a reflection coherence and strength proportional to their length, or more specifically the number of grating planes. The reflection spectrum both narrows and gets stronger with increasing length until a saturation limit is reached. At phase multiples other than the fundamental order, the reflection is both weaker and broader due to the larger geometry and wider range of affected wavelength.

Coupled Mode Theory

The preceding approximation is sufficient for rudimentary analysis as a narrow band mirror or notch-filter, however in order to understand the interactions between modes in greater detail we must apply more rigourous techniques.

Coupled mode theory is a widely used technique capable of fine resolution analysis of the interaction between different guided modes, whilst remaining easy to use. The work

of Yariv [11] and Erdogan [10] describe in great detail the application of coupled mode theory to guided optics and gratings. We shall present an abridged and applied account from these texts, collating information relevant to the work in this thesis. For a full a detailed explanation the reader is directed to this referenced work.

We shall consider two modes; the forward propagating mode $A(z)$, and the counter propagating mode $B(z)$. Normally these are orthogonal and do not interact, however in a region of dielectric perturbation energy is transferred between modes such that the respective resultant modes $R(z)$ and $S(z)$ can be described by:

$$R(z) \equiv A(z)e^{i\delta z - \frac{\phi}{2}} \tag{2.3}$$

$$S(z) \equiv B(z)e^{-i\delta z + \frac{\phi}{2}} \tag{2.4}$$

where δ represents the detuning from the designed peak wavelength λ_D given by:

$$\begin{aligned} \delta &\equiv \beta - \frac{\pi}{\Lambda} \\ &= \beta - \beta_D \\ &= 2\pi n_{\text{eff}} \left(\frac{1}{\lambda} - \frac{1}{\lambda_D} \right) \end{aligned} \tag{2.5}$$

If we assume that all power is transferred between modes:

$$\frac{dR}{dz} = i\hat{\sigma}R(z) + i\kappa S(z) \tag{2.6}$$

$$\frac{dS}{dz} = -i\hat{\sigma}S(z) - i\kappa^* R(z) \tag{2.7}$$

where κ is the 'AC' self-coupling coefficient given by

$$\kappa = \kappa^* = \frac{\pi}{\lambda}\overline{\delta n_{\text{eff}}} \tag{2.8}$$

and $\hat{\sigma}$ is the 'DC' self-coupling coefficient defined as

$$\hat{\sigma} \equiv \delta + \sigma - \frac{1}{2}\frac{d\phi}{dz} \tag{2.9}$$

From equations 2.6 and 2.7 we can calculate the cumulative effect of a grating's index profile on both the transmission and reflection spectra.

Uniform Fibre Bragg Grating

A uniform fibre Bragg grating is an FBG where both δn_{eff} and ϕ are constant over the entire length of the grating. Therefore κ, σ, and $\hat{\sigma}$ are constant with respect to z, which means R and S have closed form solutions [10].

If we assume that the wave originates from $z = -\infty$ (or $R(-L/2) = 1$) and there is no reflection beyond $z \geq L/2$ (or $S(L/2) = 0$). The reflection amplitude $\rho = S(-L/2)/R(-L/2)$ is given by:

$$\rho = \frac{-\kappa \sinh\left(\sqrt{\kappa^2 - \hat{\sigma}^2}L\right)}{\hat{\sigma}\sinh\left(\sqrt{\kappa^2 - \hat{\sigma}^2}L\right) + i\sqrt{\kappa^2 - \hat{\sigma}^2}\cosh\left(\sqrt{\kappa^2 - \hat{\sigma}^2}L\right)} \tag{2.10}$$

and the reflection power $r = |\rho|^2$:

$$r = \frac{\sinh^2\left(\sqrt{\kappa^2 - \hat{\sigma}^2}L\right)}{\cosh^2\left(\sqrt{\kappa^2 - \hat{\sigma}^2}L\right) - \frac{\hat{\sigma}^2}{\kappa^2}} \tag{2.11}$$

Figure 2.1 illustrates the reflection spectra with respect to the normalised wavelength:

$$\frac{\lambda}{\lambda_{\max}} = \frac{1}{1 + \frac{\hat{\sigma}L}{\pi N}} \tag{2.12}$$

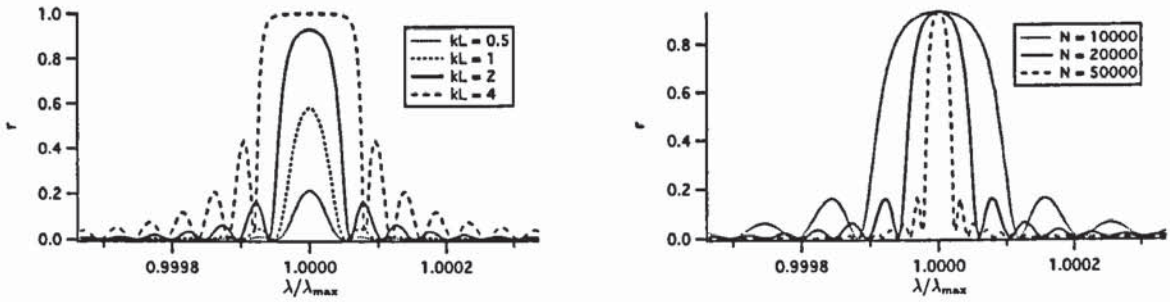

(a) Effect of coupling strength ($N = 2000$)

(b) Effect of grating length ($\kappa L = 2$)

Figure 2.1: Uniform fibre Bragg grating reflection spectra: The characteristics of uniform fibre Bragg gratings show that an increase in coupling strength increases the grating strength until it reaches a point of saturation and begins to broaden. Increasing the grating length whilst keeping the coupling strength length product (κL) constant narrows the reflected spectral width.

where the maximum amplitude occurs at $\hat{\sigma} = 0$ or

$$\lambda_{\max} = \left(1 + \frac{\overline{\delta n_{\text{eff}}}}{n_{\text{eff}}}\right) \lambda_D \tag{2.13}$$

There are some significant features that we can see from Figure 2.1. Firstly as expected the grating's width changes with respect to the number of grating planes N in the device (Fig. 2.1(b)).

Secondly from Figure 2.1(a) we see that with strong gratings the reflection becomes wider, independent of any change in grating length. This is because the light does not penetrate the full length of the grating, thus reducing the effective length of the device and linking the width to $\overline{\delta n_{\text{eff}}}$.

Lastly we note the presence of resonances outside the primary Bragg reflection. These are known as sidelobes and can be attributed to the abrupt index change at the ends of the FBG creating a Fabry-Pérot like cavity over the length of the grating [12].

Non-Uniform Fibre Bragg Grating

The analysis detailed in the preceding section is only valid for a uniform FBG, where both δn_{eff} and ϕ are constant over the entire length of the grating. For the majority of devices this is not the case, either by design or by effect. Gratings are often designed to have a certain profile so that it has a specific response. In addition to this they may have a certain index profile caused by the manufacture method.

In order to evaluate these non-uniform structures we need to evaluate equations 2.6 and 2.7 piece-wise, either through numerical integration or evaluation as a combination of many uniform gratings [10]. Here we present the piecewise uniform method [13].

For reflection spectra we evaluate the following matrix

$$\begin{bmatrix} R_i \\ S_i \end{bmatrix} = F_i \begin{bmatrix} R_{i-1} \\ S_{i-1} \end{bmatrix} \tag{2.14}$$

where

$$F_i = \begin{bmatrix} \cosh(\gamma \Delta z) - i\frac{\hat{\sigma}}{\gamma}\sinh(\gamma \Delta z) & -i\frac{\kappa}{\gamma}\sinh(\gamma \Delta z) \\ i\frac{\kappa}{\gamma}\sinh(\gamma \Delta z) & cosh(\gamma \Delta z) + i\frac{\hat{\sigma}}{\gamma}\sinh(\gamma \Delta z) \end{bmatrix} \tag{2.15}$$

and

$$\gamma = \sqrt{\kappa^2 - \hat{\sigma}^2} \tag{2.16}$$

where κ and $\hat{\sigma}$ are as given by 2.8 and 2.9 respectively.

We start at $R_0 = R(L/2) = 1$ and $S_0 = S(L/2) = 0$. Then calculate through to $R(-L/2)$ and $S(-L/2)$, where again we can calculate the amplitude reflection $\rho = S(-L/2)/R(-L/2)$, and the reflection power $r = |\rho|^2$.

This allows us calculate the reflection spectrum for any arbitrary grating profile. Transmission and group delay can be calculated in a similar manner using a different matrix [10].

2.2 Inscription

As one might expect from over 30 years of research, the knowledge in the area of fibre Bragg grating inscription and manufacture is deep and wide ranging. The realisation of a link between the 240-250nm absorption band in germanosilicate fibre and long-lasting index change has been integral to FBG development.

Exposure to a continuos interference pattern of UV light is the dominant manufacture method for fibre Bragg grating manufacture. However inscription with high intensity pulsed sources such as KrF excimer or more recently TiSaphire femtosecond lasers enable inscription methods that can manufacture devices during the fibre drawing process [14] or negate the requirement to strip an already coated fibre [15].

Ultra-Violet Photosensitivity

The 240-250nm absorption band in germanosilicate fibre has been linked to GeO defects created during the fibre manufacture process [4]. These defects form weak covalent bonds with other Ge or Si atoms present in the silica lattice (Fig. 2.2). This weak bond has an absorption peak at 242nm which when excited breaks and releases the electron into the conduction band, forming a negatively charged GeE′ trap. This electron diffuses into the lattice and becomes trapped by a neighbouring GeE′ site.

This molecular change alters the absorption characteristics, which in turn changes the refractive index through the Kramers-Kronig relationship [4]:

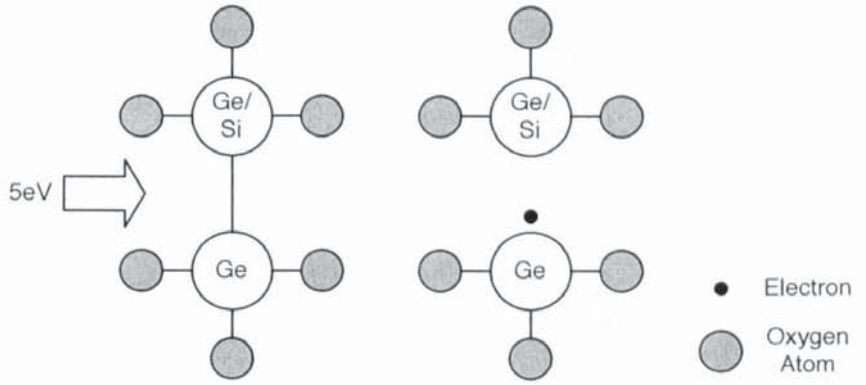

Figure 2.2: UV index change mechanism: Sufficient excitation of the weak covalent bond releases an electron which is free to diffuse into the silica lattice. The resultant molecular change alters the absorption characteristics which in turn changes the refractive index.

$$\Delta n_{\text{eff}}(\lambda) = \frac{1}{2\pi^2} P \int_0^\infty \frac{\Delta\alpha_{\text{eff}}(\lambda)}{1 - \left(\frac{\lambda}{\lambda'}\right)^2} d\lambda \tag{2.17}$$

Where P is the principal part of the integral, λ is the wavelength, and $\alpha_{\text{eff}}(\lambda)$ is the effective change in the absorption coefficient of the defect.

Hydrogen-loading has been shown to have a significant effect upon photosensitivity [16]. The presence of GeH molecules in the lattice is thought to increase the efficiency of GeE′ generation when exposed to UV light. This provides an easy and efficient method of creating highly photosensitive fibre from standard germanosilicate fibre type without the need for co-doping.

Longevity and Reliability

One of the primary concerns for sensing applications is how reliable the sensor is. With this in mind it is important to recognise that the index modification described in the preceding section is not permanent. The trapped electrons are readily thermally excitable, and the speed of their return to their original un-trapped state is accelerated by elevated temperature.

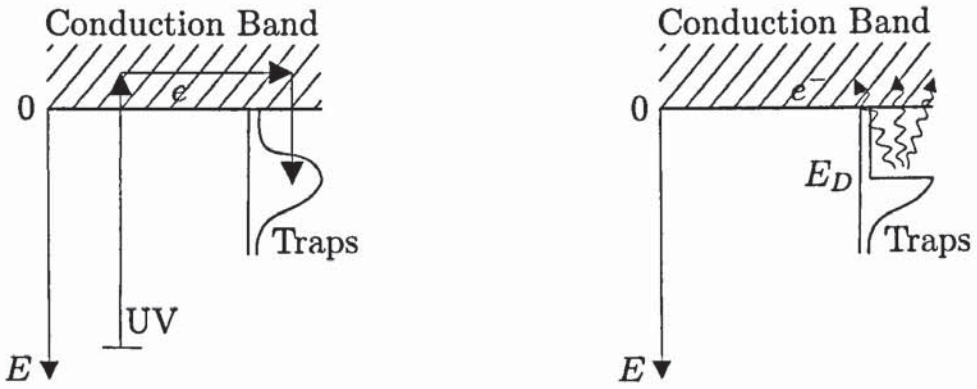

(a) Inscription (b) Annealing

Figure 2.3: Conduction Diagram: During inscription electrons are excited to the conduction band and trapped by neighbouring negatively charged GeE′ traps at a distributed energy level. Electrons at an energy below the *demarcation* energy level E_D, a function of time and temperature 2.18, are freed to the conduction band to return to their original location.

Erdogan et al. [17] demonstrate for germanosilicate fibre that the trapped state is at a distributed energy level (Fig. 2.3(a)). This is significant because trapped electrons at an energy below the *demarcation* energy level E_D are freed to the conduction band and return to their original location (Fig. 2.3(b)).

This demarcation energy is a function of both temperature and time and for non-hydrogenated germanosilicate fibre has been modelled as linear with respect to temperature T and logarithmic with respect to time t:

$$E_D(T,t) = k_B T \ln(v_0 t) \tag{2.18}$$

Where k_B is the Boltzman constant and v_0 is a fibre specific constant scaling the fibre's energy release rate v at energy level E with respect to temperature, given by:

$$v(E) = v_0 \exp\left(-\frac{E}{k_B T}\right) \tag{2.19}$$

For hydrogenated fibre the energy level has a wider distribution reaching closer to the conduction band. This has been shown not to obey the same model as non-hydrogenated

germanosilicate fibre [18, 19], however still demonstrates a similar logarithmic relationship with respect to time.

The significance of these relationships is twofold. Firstly it is clear that for stable and predictable operation throughout a specific temperature range, the device must be annealed to at least the maximum temperature for a sufficient time such the all trapped electrons below $E = k_B T$ have been freed. Otherwise both reflection strength and wavelength are susceptible to change whilst in operation.

Secondly we introduce the concept of accelerated ageing. Given that the rate of change of E_D is proportional to the temperature, it is possible to accelerate the annealing process by exposure to an elevated temperature. Whilst not always a recommended method for high temperature operation, this method is particular useful for ambient temperature operation where electron diffusion is otherwise slow.

Inscription Techniques

Whilst direct point-by-point inscription processes for fibre Bragg gratings have been developed [20, 21], the manufacture of a consistent, high quality core index modulation typically requires a stable interference pattern.

The holographic inscription method [22] (Fig. 2.4) is a flexible method capable of generating inscription patterns with a periodicity governed by the geometry of the beam path. Specifically the rotation of the mirrors varies the angle of the beams such that a pattern of period Λ is created, where

$$\Lambda = \frac{\lambda_{UV}}{2 \sin \theta} \tag{2.20}$$

which would inscribe a grating at

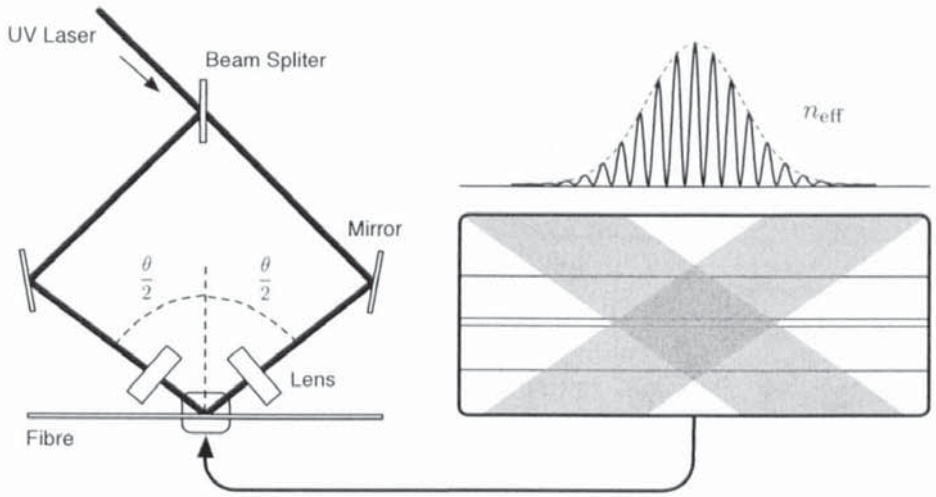

Figure 2.4: Holographic grating inscription: The fine interference pattern required for fibre Bragg grating inscription is created by the intersection of two coherent beams at a specific angle. The resulting inscribed structure has a refractive index profile shaped relative to the inscription beam.

$$\lambda_B = \frac{n_{\text{eff}}\lambda_{\text{UV}}}{\sin\theta} \tag{2.21}$$

Although this method has clear benefits in terms of wavelength flexibility it does have its drawbacks. The beam path is very long, and is aligned by skill and judgement. It is very difficult to create an exact interference pattern in line with the fibre and therefore there can be slight tilt to the grating plane which may result in an undesired grating response from light scattering into radiation modes [23].

Additionally the grating length and profile is limited to the spot size of the inscription beam. Whilst the sidelobes are suppressed by not having an abrupt index change, FBGs with a Gaussian index profile have a resonance on the short wavelength edge (Fig. 2.5). This is a different Fabry-Pérot effect between the edges of the grating, occurring because the central region has a higher effective index and has therefore shifted to a longer wavelength than the weaker edges, creating a cavity [12].

The phase mask method (Fig. 2.6)[24, 25, 26] uses the interference pattern created

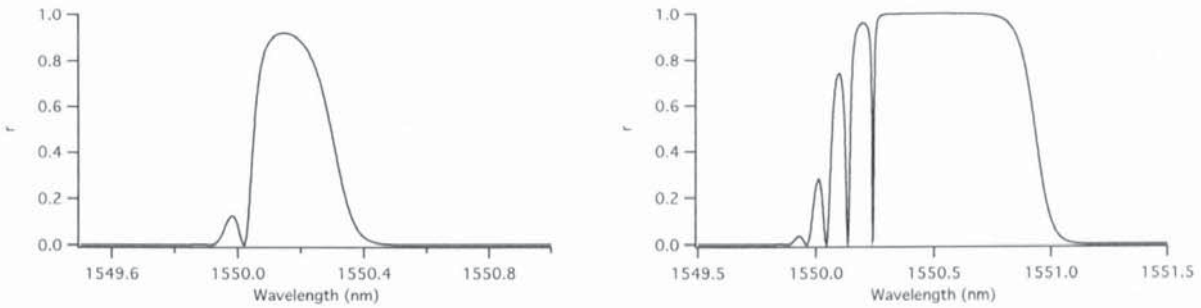

(a) $\kappa L_{\mathrm{FWHM}} = 2$ (b) $\kappa L_{\mathrm{FWHM}} = 6$

Figure 2.5: Reflection spectra for fibre Bragg gratings inscribed with a Gaussian index profile: Gaussian profiled gratings suffer from a short wavelength resonance on the short wavelength side caused by the creation of a Fabry-Pérot structure between the edges of the grating. This feature is more pronounced with stronger gratings.

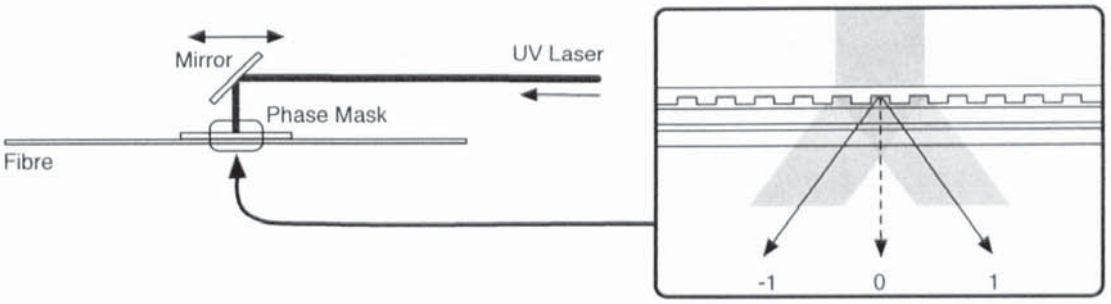

Figure 2.6: Phasemask grating inscription: A phase grating can be used to create the inscription interference pattern out of the two first order diffraction modes. Such a grating can act as a mask allowing a fibre placed immediately behind the grating to be exposed to a reliable and repeatable interference pattern, inscribing a fibre Bragg grating at twice the period of the phase grating

immediately behind a phase grating. The phase mask is designed such that the zero order is weak, with the majority of the light diffracted to the 1st order modes. This inscribes a grating at twice the period of the phase mask.

The primary advantages of this inscription technique are the simplified and reduced free-space alignment, the ability to write long gratings by scanning the inscription beam, and the ability to inscribe complex grating structures repeatedly. Whilst phase masks remain expensive to manufacture, they can be used to replicate identical gratings on a mass scale.

Since FBG inscription phase masks are designed to concentrate the majority of an incoming beam into the 1st order modes, we can use it as the beam splitting element in the preceding holographic inscription system. In doing so we create a Talbot interferometer out of the ± 1 order beams which can be used to replicate an image of the phase mask [27], adjustable in scale by the mirror angle. This allows scanning of the inscription beam to inscribe long gratings at arbitrary wavelengths as dictated by the beam geometry. This method has also been shown to inscribe chirped gratings using a chirped phase mask [28]. It should be recognised however the alignment difficulties still remain with this inscription method.

Some subtle adjustment to wavelength can be made by straining the fibre prior to inscription, however it has also been shown that dithering the phase mask position relative to the fibre enables a fine and continuous control over both the index profile (known as *apodisation*) and also the grating periodicity [29]. Using a modulated laser beam to achieve this dither has shown to be particularly successful [30, 31] as it ensures minimal moving parts and thus alignment. By precise fibre translation and beam modulation it is possible to inscribe arbitrary apodisation profiles, phase shifts, and create chirped period profiles. Chirped profiles do however incur an apodisation profile relative to the beam width due to the increased overlapping of the out of phase fringes [29, 31].

High-Intensity Pulsed Laser Inscription

Because of their optimal wavelength and stable characteristics, KrF Excimer pulsed laser sources have been used alongside continuous wave lasers throughout the history of fibre Bragg grating inscription. However in more recent years interest has grown in the inscription of devices by ultra-short high-power laser pulses at wavelengths away from the 240-250nm absorption band, introducing an alternative inscription mechanism.

Commonly fibre Bragg gratings are inscribed using the described UV absorption mech-

Grating type	Cumulative fluence (J/cm^2)	Typical pulse energies (mJ/cm^2)	Writing conditions		Obervations
			CW	Pulsed	
Type I	Up to 500	100	Y	Y	
Type IIA	> 500	100	Y	Y	Associated with compaction of the glass matrix
Type II	NA	1000	N	Y	Associated with fusion of the glass matrix

Table 2.1: Key Differences between Types I, II, and IIA Bragg Gratings [4]

anism, modifying the refractive index of the germanium doped core and forming what are known as Type I fibre Bragg gratings [4]. Changes to the inscription power and duration allow the inscription of alternative structures each with different thermal characteristics (Table 2.1)[4, 32]. However this is still reliant on presence of Ge-Ge or Ge-Si bonds in the specific region of inscription, making grating manufacture within speciality fibre such as photonic crystal fibre or erbium doped fibre difficult.

Another problem directly related to UV inscription is that the grating region must have the fibre's protective buffer removed, since this is typically sensitive to UV light. Removal of this buffer can result in surface strength degradation, the extent of which depends on the stripping mechanism used. Hydrogen loading to increase the photosensitivity of the fibres has also been shown to decrease the mechanical strength of the fibre [33].

Direct inscription in a variety of optical materials at wavelengths away from absorption peaks has been demonstrated using high powered lasers with a pulse duration in the order of femtoseconds. The effected region of multi-photon absorption from a focused beam becomes is highly localised using sub picosecond pulse width [34], and the highly non-linear relationship to beam intensity enables three-dimensionally localised refractive index modification at arbitrary depths in a dielectric medium [35, 36].

Application of this inscription process to fibre Bragg grating manufacture has been highly successful. Inscription has been demonstrated using the phase mask technique at a variety of wavelengths [37, 38], and also by direct point-by-point illumination [15] with the

ability to inscribe at arbitrary positions within the core [39]. Significantly it has enabled inscription of multiple fibre types including rare earth mineral doped fibres [40, 41] and photonic crystal fibre [42], and being wavelength independent the manufacture method is readily able to inscribe through the protective polymer buffer [15], negating the need to strip away any coating.

Beyond the manufacturing advantages, fibre Bragg gratings inscribed by femtosecond laser have been demonstrated to survive and provide stable long-term functionality at significantly elevated temperatures [43, 40]. This is indicative of Type II behaviour and the possibility of a partially 'damage written' grating, and is a significant advantage for temperature sensing applications.

It is perhaps the temperature response of femtosecond inscribed structures that illustrate the fact that there are still unknowns. Whilst it is generally accepted that there are regions of damage and regions of index change, the complete makeup and its relation to the beam profile and strength is still not fully understood. Cyclic annealing studies of both long-period and fibre Bragg gratings have failed to fully separate regions of increased stress, quenching, and damage [44]. In addition to this high-power transmission through regions of inscription have highlighted unknown self heating and potential fibre fusing effects [45].

Ultimately however it can be seen that the use of femtosecond inscription will prove significant to the future of fibre optic sensing. The ability to provide reliable, stable, and easily produced structures in different fibre types will bring forward the entire discipline, and the ability to combine these structures with micro-machining techniques [46] will undoubtedly benefit the entire fibre optic sensing industry.

2.3 Fibre Bragg Gratings As Sensors

Fibre Bragg gratings make ideal optical fibre sensors. Since the Bragg wavelength is proportional to changes in both refractive index n_{eff} and grating period Λ, there are two mechanisms that are exploitable for physical measurement sensing. We can denote this as:

$$\Delta\lambda_B = 2\left[\Lambda\frac{\delta n_{\text{eff}}}{\delta M} + n_{\text{eff}}\frac{\delta\Lambda}{\delta M}\right]\Delta M \tag{2.22}$$

where M represents the measurand, and $\delta n_{\text{eff}}/\delta M$ and $\delta\Lambda/\delta M$ the measurand's respective index and expansion coefficients.

From this it is clear that a change in physical property that has an effect on either n_{eff} or Λ will change the Bragg wavelength proportionally. This wavelength encoded measurement is a distinct advantage over other optical fibre sensors, as the measurement is impervious to source fluctuation, connector losses, and other such problems affecting the DC light level.

For FBG sensors the primary sensing mechanisms are strain and temperature. A small polarisation dependent sensitivity to dynamic magnetic field can be detected [5], however the effects of magnetic fields can generally be discounted in comparison with the fore mentioned quantities. Secondary measurands can exploit these primary mechanisms to change the Bragg wavelength, enabling sensors such as pressure [47, 48] or chemical sensors [49]. The effect upon wavelength is shown in Table 2.2.

Measurement Systems

Key to the use of fibre Bragg gratings as sensors are the systems that employ them. This is representative on two levels. Firstly the uncertainty with which the Bragg wavelength

Wavelength (μ m)	Strain sensitivity (pm $\mu\epsilon^{-1}$)	Temperature sensitivity (pm $^{\circ}C^{-1}$)
0.83	~ 0.64	~ 6.8
1.3	~ 1	~ 10
1.55	~ 1.2	~ 13

Table 2.2: Strain and temperature sensitivities of FBG sensors at different operation wavelengths [5]

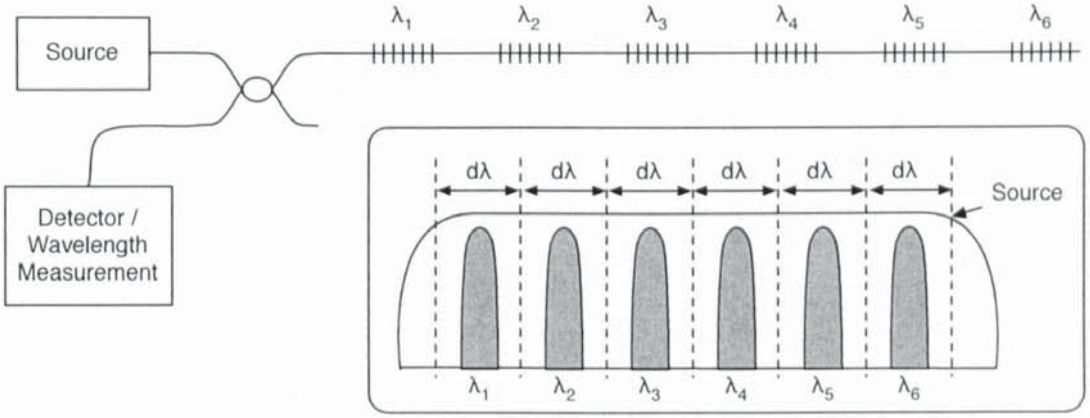

Figure 2.7: Wavelength Division Multiplexed (WDM) FBG sensor topology: A WDM topology separates each fibre Bragg grating into specific regions of operating wavelength, with the maximum number of grating sensors being dictated by width of the source and the required operating range for each grating

is measured is the limiting factor to a measurement system's accuracy. Secondly the envision of multiplexed systems containing multiple sensors reduces the 'per sensor' cost and makes a system commercially viable.

Several different multiplexing topologies have been demonstrated for FBG sensing. Time Division Multiplexing (TDM) [50, 51, 52, 53], Code Division Multiplexing (CDM) [54], and Wavelength Division Multiplexing (WDM) [7] topologies are all realisable within FBG sensor systems. Of these WDM based schemes are possibly the easiest to realise and form the basis for work contained inside this thesis.

Figure 2.7 shows a simple generic WDM topology for use with FBG sensors. Each sensor is separated by and works within a specified operation range $d\lambda$. The number of

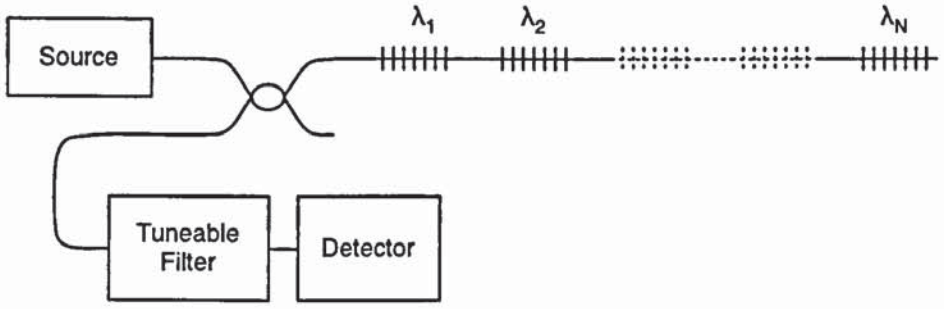

(a) Scanning filter technique

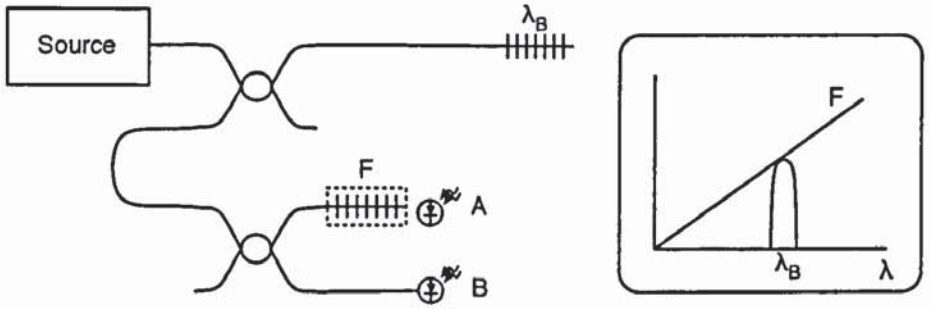

(b) Edge-filter interrogation technique

Figure 2.8: Filter based interrogation methods

sensors that may be used within the system is dictated by the width of this range in relation to the width or range of the illuminating source.

It is the wavelength measuring device that dictates the accuracy of the system. For high precision measurement scanning tuneable laser systems have proven to have optimal accuracy [55]. As the source has a very narrow line width the technique can be employed directly in the illustrated scheme without further modification, however the cost is prohibitive for low-cost systems.

An analogous method would be to use a scanning filter in combination with a broadband source (Fig. 2.8(a)). This has proven successful and can be implemented using a variety of different filter types including Fabry-Pérot [7], acousto-optic [56], and fibre Bragg gratings [57].

Scanning methods are however inherently slow, especially for systems with mechanical moving parts. Edge-filter interrogation [3, 58](Fig. 2.8(b)) uses a wavelength dependent

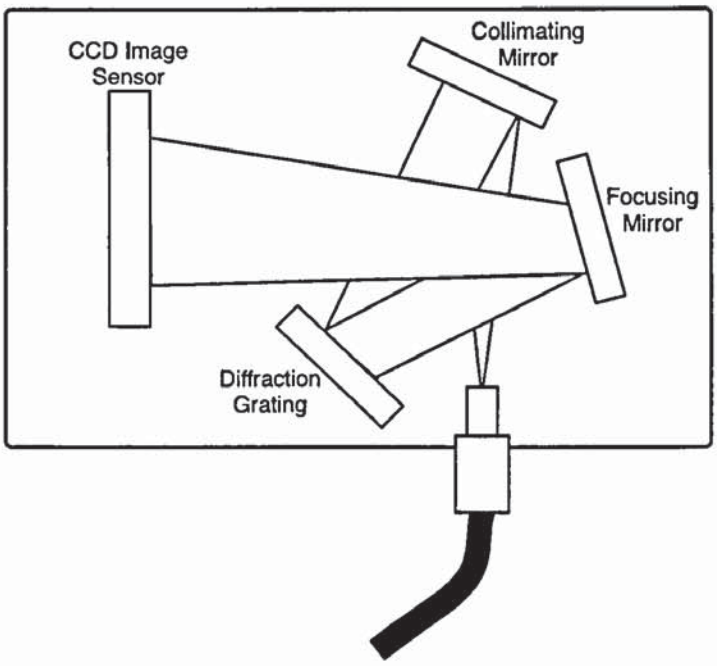

Figure 2.9: CCD Spectrometer: CCD spectrometers diffract the incoming light such that different wavelengths are focused at different points on a CCD image sensor, creating a low resolution optical spectrum analyser

filter F in series with the reflected spectra to create an intensity relative to the FBG wavelength. By comparing this intensity against a non-filtered signal it is able to measure the FBG wavelength in realtime. Since this method measures the relative response against a non filtered signal it is immune to source fluctuation, however the edge filter must be of known function and must be stable throughout measurement. Unfortunately this method is difficult to apply to WDM systems and although solutions exist [59], it is difficult to scale due to the large number of custom filters which each require environmental stabilisation.

Diffraction based CCD spectrometers (Fig. 2.9) offer a low cost alternative to laboratory optical spectrum analysers (OSAs). These devices measure a low resolution image of the spectra by diffracting the beam such that the different wavelengths are spread across a CCD image sensor. Whilst design primarily for biomedical spectroscopy applications they have been demonstrated applied to FBG interrogation [60]. These devices are commercially available in bulk optic form, and devices based upon tilted FBGs [61, 62] and

planar optical waveguides [63] have shown potential for continued improvement and cost reduction.

2.4 Conclusion

We have presented a comprehensive overview of fibre Bragg grating technology, outlining aspects of theory and practice. Using coupled mode theory we presented an insight into how a FBG works, and the subtlety of design. We have also described techniques to characterise and model any arbitrary device.

Methods of inscription have been presented and a explanation for index change mechanisms has been offered. We have outlined concerns about device stability and longevity, and offered a solution as to how accelerated ageing might ensure stable operation. Finally we presented the mechanisms behind FBG sensing, and described methods for integration into measurement systems.

Chapter 3

Function Approximation and Machine Learning

Finding and modelling patterns within measured data is an important scientific discipline with wide ranging application. Being able to statistically recognise and identify underlying relationships is a fundamental part of scientific activity.

Research in the area of machine-learning is both wide ranging and fast moving. Within this thesis we limit the scope to the application of established methods from the area of neural networks, which are arithmetic networks designed to mimic the biological nervous system and its parallel computational architecture.

In this chapter we present the fundamental concepts required for understanding of neural networks and their application for function approximation. We attempt to give an overview and insight into the different models and learning methods available, and describe the underlying methods used throughout the remainder of this thesis.

3.1 Machine Learning Principles

Machine learning is the process of fitting a mathematical model to an unknown system. This is an iterative process based on two factors; the minimisation of *error* as the quantitative measure of the fit, and the improvement of *generalisation* as the qualitative measure.

In order to illustrate the key concepts associated with machine learning we present a polynomial curve fitting [64], demonstrating the approximation of a single sine wave cycle using an Mth order polynomial model with weighting vector w:

$$y(x) = w_0 + w_1 x \dots w_M x^M = \sum_{j=0}^{M} w_j x^j \tag{3.1}$$

The first part of all machine learning methods is to collect independent sets of data; a *training* set, and a *validation* set. These set contain both inputs x and targets y. In this particular example we construct a training set of N evenly spaced samples from the function $y = \sin 2\pi x$ with the addition of random Gaussian distributed noise. The testing set shall comprise samples from the same function without the additional noise.

Error is measured with an error function, such as the *sum of the error squared* function:

$$E(\mathrm{w}) = \sum_{n=0}^{N} \{y(x_n; \mathrm{w}) - t_n\}^2 \tag{3.2}$$

The learning or *training* stage is the systematic manipulation of the weighting vector w such that the error against a set of target values (the training data set) is minimised. Upon minimisation against the training data we test the prototype model with the validation data set.

The results of different minimised polynomial models with increasing complexity M can be seen in Figure 3.1(a). Here we can see the effect of over-fitting a function to the

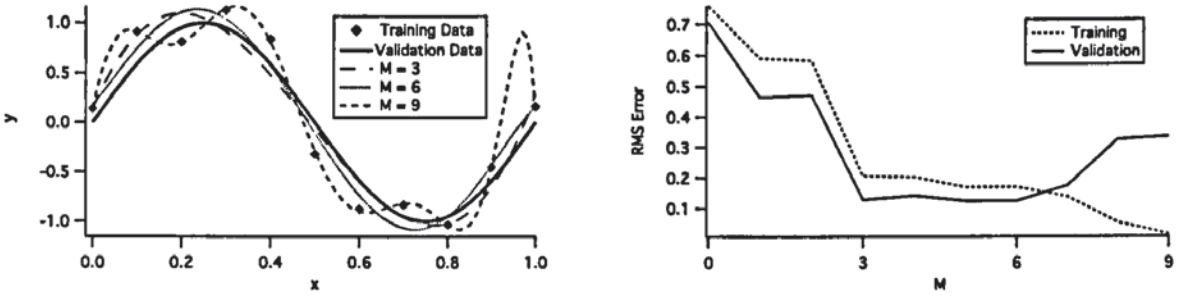

(a) Validation (b) Generalisation

Figure 3.1: Demonstration of the effects of model complexity for function approximation. As the model polynomial order M is increased we start to see the model 'over-fit' the data (Fig. 3.1(a)). The use of a secondary validation data set to test the trained model illustrates the point of model over-fit (Fig. 3.1(b)).

data (as with $M = 9$). Regularisation or *Generalisation* is the prevention of this and refers to the ability of the model to produce reasonable outputs for inputs it hasn't seen before. This can be thought of as the application of 'Occam's Razor' to the problem [65], where the least complex solution is usually the best.

One measured approach to achieving optimal generalisation is to test the network with a secondary validation data set. Increasing the complexity whilst monitoring error from a trained model with this independent validation data set allows us to gauge when the model is starting to over-fit the data (Fig. 3.1(b)).

This use of independent data to check the model is key to machine learning and is a requirement of many learning algorithms.

3.2 Linear Models

The polynomial model used in the preceding section is an example of a linear model. It follows the form of

$$y(x) = \sum_{j=1}^{N} w_j \phi_j(x) \tag{3.3}$$

where ϕ_j represents fixed functions of x, known as *basis functions.* These functions do not need to be related to each other nor be linear functions of x. Models of this form are denoted as linear models even if the vector ϕ contains non-linear functions because they represent a linear summation of weighted models that are themselves fixed.

For linear models the sum of squares error function 3.2 forms one single minimum and can be found by when $dE/d\mathbf{w} = 0$.

This can be solved using a matrix representation of the system and its weights:

$$\mathbf{y(x)} = \mathbf{W}\phi \tag{3.4}$$

which can be solved for target vector $\mathbf{T}$ and $\Phi = \phi_j(\mathbf{x^n})$ by [66]:

$$\mathbf{W^T} = \mathbf{\Phi^\dagger T} \tag{3.5}$$

where $\Phi^\dagger$ denotes the pseudo inverse of Φ

Press [67] provide an implementation of this calculation with increased reliability and accuracy though use of Singular Value Decomposition.

This linear optimisation process is denoted as linear least squares regression.

Linear Neuron Model

The Adaptive Linear Element (ADALINE) (Fig. 3.2) [1] is a linear model of the form:

$$y = \sum_{j=0}^{N} w_j i_j \tag{3.6}$$

where N represents the total number of inputs.

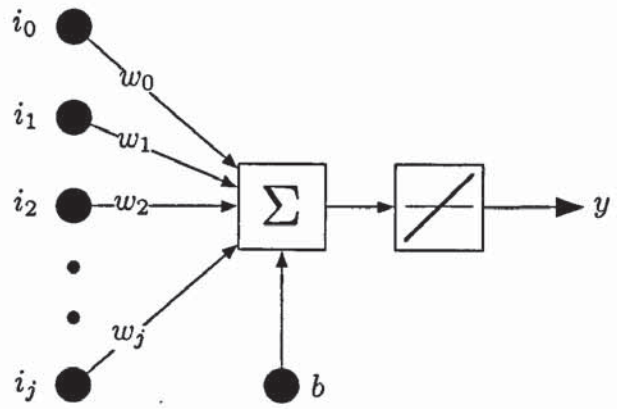

Figure 3.2: The Adaptive Linear Element (ADALINE) calculates the biased sum of a set of weighted inputs.

This forms one of the fundamental building blocks of neural networks known as the neuron, and is classed as part of the perceptron family. It draws its inspiration from biological neurones and consists of a summing junction summing each of the synaptic inputs as scaled by their respective weights. The output is linear with respect the the summation due to the linear activation function which follows the summing node.

The usage of this model is primarily for adaptive filtering, due to its similarity to traditional FIR filter models. However the use of a linear transfer function allows linear least square regression to be used as the training method which can be beneficial in some situations.

Multi-Layer Perceptrons

Whilst single layered architectures are useful, they cannot be used to model any arbitrary function. Despite the capability to use non-linear activation functions, the output is still generated by a linear function of the input. Multi-Layer Perceptrons (Fig. 3.3) on the other hand have been proven to have the capability and flexibility to approximate any model [66].

The architecture consists of a minimum of three layers (including the input layer). The

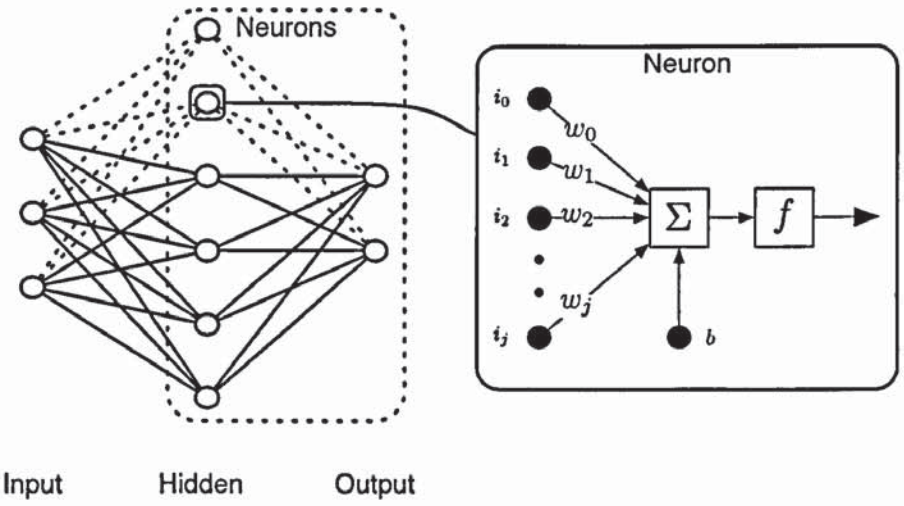

Figure 3.3: The Multi-Layer Perceptron network comprises interconnected layers of neurons, each calculating the biased weighted sum of their inputs, scaled by an activation function.

input nodes are non-computational, with outputs connected to each and every neuron in the next layer[1].

The second layer is a layer of neurons, each consisting of a summation of weighted inputs followed by a (typically non-linear sigmoidal) activation function. This layer is known as the hidden layer because neither its inputs or outputs are connected to the real world. There can be successive hidden layers however it has been proven theoretically unnecessary as a three layer model can approximate any function[2].

The final layer is another layer of neurons and processes the results of the hidden layer(s).

Typically for function approximation neurons in the hidden layer would have sigmoidal activation functions, whilst neurons in the output layer would use linear functions. This is known to assist the training process as it assists gradient calculation [66]. As such pattern detection and processing is performed in the hidden layer, whilst the output layer

[1]Methods to prune some of these connections for efficiency purposes exist, however are not considered in this thesis

[2]It should be recognised that extra hidden layers can however encourage generalisation in otherwise large networks

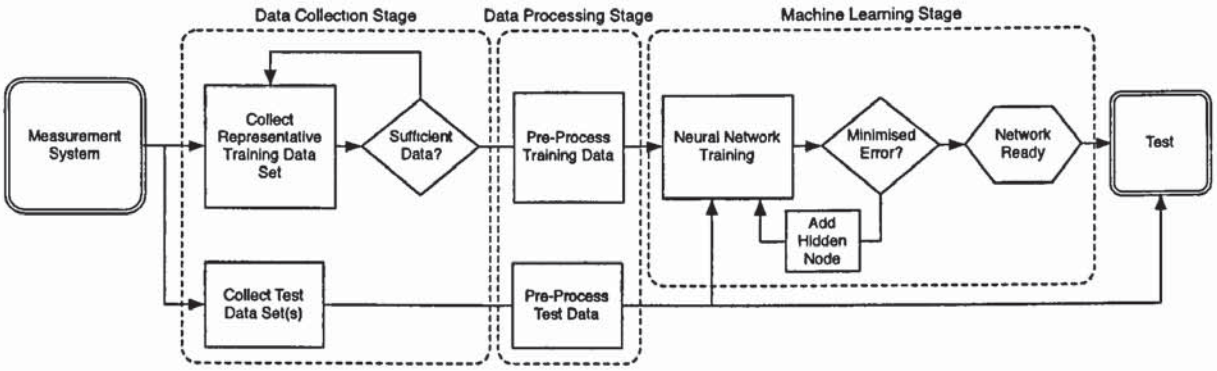

Figure 3.4: The training cycle for Multi-Layer Perceptron networks. Separate test and training data is collected, pre-processed to emphasise or normalise the data characteristics, the network trained and iteratively manipulated to find the optimal architecture.

provides a linear response relative to their computation.

Figure 3.4 shows the typical approximation workflow required for MLP approximation. It can be seen as essentially the same workflow as described in section 3.1.

The collection of data representative of the system is the first step in the learning process. Many training methods require an additional set of data for cross-validation purposes so typically three sets of data is the minimum requirement. This data then requires scaling such that all inputs are of the same variance. This is so that the training / error minimisation stage can follow the correct path of minimisation. The network is first initialised to a simple configuration of a few hidden nodes and the training algorithm calculates the correct weights from the training set.

Following completion of training the model is tested, the networked changed, and the new model trained. This process works the same as that shown in Figure 3.1(b), however instead of adding extra polynomial terms to the model we are adding extra neurons to the hidden layer. Once the error from the test data set has reached a minimum, the model is deemed optimal.

Training

Due to the non-linearity and increased model complexity the difficulty in training a neural network is a limiting factor. Whilst the architecture itself is inherently flexible, it is not always possible to reach that optimal configuration. Subsequently training algorithms are wide, varied, and under continuous research.

The problem with training multilayered networks is that there is no visibility of the correct output from each node in the hidden layer. This means that the network must be analysed behaviourally and iteratively, and the network's weights adjusted accordingly.

Backpropagation is the standard technique used for such training and is a generalisation of the previously described least squares method. It can be thought of as a two pass process through the network; a forward pass and a backward pass [68].

In the forward pass the training data propagates through the network in the conventional manner, from input to output identifying the error between the network output and the correct result for the given input condition. In the backward pass the errors from this forward pass are passed back through the network, from the outputs towards the inputs, in the form of error gradients. This being the error scaled by the synaptic weight and activation function. All of the weights are adjusted proportionally to inverse of this error gradient, which is measured at each and every synaptic weight. The proportion at which the weights are changed is known as the learning rate parameter. The ultimate aim is to reduce the error gradient for each synaptic weight to zero by iteration.

This method is known as the gradient descent training method. Whilst it does work and is relatively easy to understand it is a heavily iterative and computationally expensive task and is one that is difficult to optimise, because if the learning rate parameter is set too high the network will oscillate and if too low the network will not converge. There are also problems where the network appears optimal however is actually at a localised minima, as such usage of this algorithm requires repetition to ensure that is not the case.

There are other backpropagation methods that are faster to use, most notably being the scaled conjugate gradient descent method [69] which is method using the second derivative of the error function to efficiently determine optimal weight manipulation, and also application of the Levenberg-Marquardt algorithm [70] which has been proven to be the fastest method by a sizeable margin.

It is however the application of Bayesian statistics to the backpropagation problem that has particular relevance for function approximation. Whilst each of the aforementioned training methods can control and improve generalisation through means of additional independent data sets providing early stopping information, or including noise into the data set [71], MacKay [65] incorporated a probabilistic interpretation of backpropagation and weight change. This method makes maximum use of a single training data set and does not require additional verification data set to perform early stopping to the training. Instead it modifies the previously described gradient descent method to include objectivity drawn from the distribution of data and the network behaviour by statistical methods, and the weighting at each synapse is changed in accordance with this. Importantly the technique does not further complicate the training process from a user's point of view, instead the entire process is simplified because the network training only requires one single data set and does not require any parameters such as the aforementioned learning rate parameter. It is a true *black-box* method requiring only the data and the number of iterations the algorithm should make.

This method addresses problem areas of backpropagation with the ultimate aim of producing a network that is well generalised, and not simply the network with the least error for a given training set. It specifically ensures that each node is well utilised such that no dominant behaviour occurs, and the use of such a network discourages the blind use of oversized networks.

Radial Basis Function Networks

Radial Basis Function Networks (RBFNs) differ from the MLP model in that the neuron does not perform a weighted summation of the input data, instead it outputs a weighted sum of the Euclidean distance between the inputs and set of prototype vectors providing a non-linearity. For k outputs this can be expressed as [66]:

$$y_k(x) = \sum_{j=1}^{N} w_j \phi_j(\mathbf{x}) + w_{k0} \tag{3.7}$$

Although not always the case, the basis function usually takes the form of a Gaussian function:

$$\phi_j(\mathbf{x}) = \exp\left(\frac{\|\mathbf{x} - \mu_j\|}{2\sigma_j^2}\right) \tag{3.8}$$

Where $\mathbf{x}$ is the input vector, and μ contains the basis centres.

The standard training method is to set the vector μ to the input data and given that this is a linear model it can be solved using the linear least squares method described in section 3.2. As the architecture requires no iteration the model only require the setting of the basis function width σ, which effectively determines the smoothness of the output.

This is an effective training method showing excellent promise for approximation applications. However, it does have one major drawback; it doesn't scale well for large data sets.

Alternative training methods offer a different approach and select a subset of these basis functions, based upon their contribution towards the target function. Notable methods for this are the orthogonal least squares approach [72] which takes a measured approach to assess the contribution of each individual basis function to the target output, and that of Orr [73] who concentrates upon function generalisation by including a cross-validation factor to enable early stopping.

One modified architecture analogous to the RBFN is the General Regression Neural Network (GRNN) [74]. This method has the same first layer as the full RBFN including all the training data as basis functions however, it differs in that it neither performs a least square fit on the data to generate weighting nor does it perform any basis function pruning. Instead it uses an extra special layer containing a vector based upon the probability density of the training data. This is used to scale a regular summation node from the basis layer. This method has been shown to be very effective in non-linear filtering applications [75, 76] and is very fast and non-iterative in its training.

3.3 Conclusions

We have presented an overview of different machine-learning and neural network techniques paying specific attention to the application of function approximation. We have outlined major models and learning methods in the field, and have attempted to describe the underlying processes used throughout this thesis.

All of the methods and models presented within this chapter are readily available in both commercial and non-commercial software implementations; however, the author makes explicit use of the Matlab Neural Network Toolbox (Version 5.0.1) and the NETLAB toolbox [77].

Chapter 4

Low Resolution Spectral Analysis

High precision wavelength resolution of a fibre Bragg grating's wavelength is the fundamental objective for sensing applications. Picometre precision is desired in order to compete on a level plane with more mature technologies.

Spectral processing is an area of research that has significant impact upon fibre Bragg grating sensing. In particular the application of sub-pixel processing techniques [78, 79] has brought significant gains for many areas of fibre optic sensing, and has introduced a level of accuracy and stability that has enabled commercial realisation.

In this chapter we start by presenting an overview of spectral processing for fibre Bragg grating sensors. Concentrating upon two common sub-pixel measurement techniques and highlighting the benefits and limitations of their use with respect to low resolution measurement. We then introduce two novel processing methods and present theoretically simulated operation over a variety of conditions. Finally we apply these techniques to a temperature measurement system to display the resolution enhancement methods in practice.

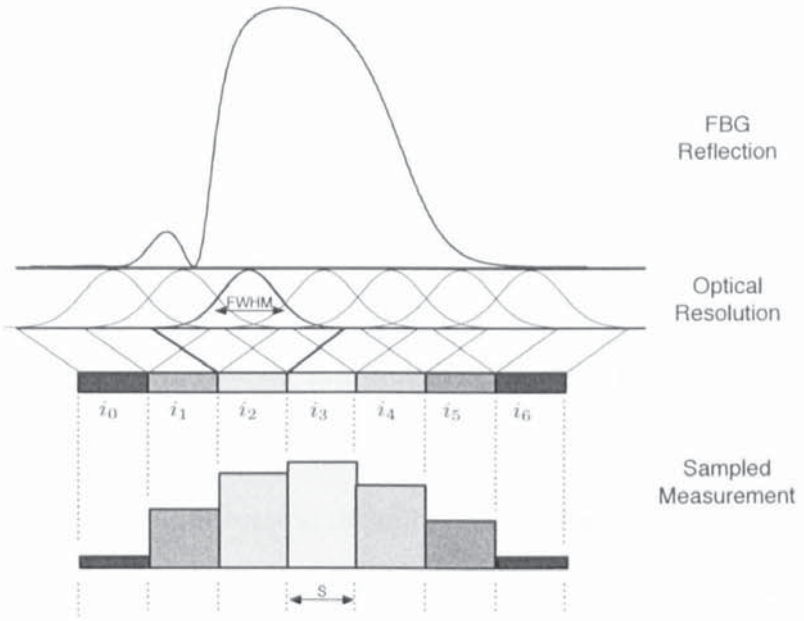

Figure 4.1: The generic spectral sampling model. The spectrum is sampled at discrete wavelengths, each sample measuring a specific optical range.

4.1 Measurement of FBG spectra

Most interrogation schemes for FBG sensors rely upon a discrete representation of the FBG reflection spectra. The nature of the sampled spectra varies between different measurement methods, however we can generalise this to the model shown in Figure 4.1 where different wavelengths are sampled at a regular interval with an optical resolution determined by the Full-Width-Half-Maximum (FWHM) measured relative to the sample period s.

Optical Spectrum Analysers (OSAs) allow a high degree of control to their sampling model which proves optimal in a laboratory environment, however for a dedicated measurement system consisting of FBGs the sampling reliability, linearity, and resolution of tuneable lasers have shown to be the preferred sampling method [55].

Low cost alternatives to these sampling systems often have less desirable characteristics. Typical problems that might be encountered include low optical and sample resolution, resulting in a low-resolution 'smeared' spectrum image; poor linearity both in terms of

sample period to wavelength and also wavelength to power conversion sensitivity; finally measurement noise may be significant.

Diffraction grating spectrometers are low cost fixed sampling devices that use a diffractive element to project an image of the spectrum across an image sensor. They are designed primarily for spectroscopy applications and exhibit many of the problems described. However it has been shown that with appropriate processing they can be used in practical FBG sensing systems [60].

The application of image processing techniques has shown great promise with respect to increasing the accuracy of these low resolution systems and overcoming systematic limitations. The methods have allowed the development of novel low cost implementations including those operating at extended wavelength ranges [61], and devices with very poor optical resolution [62].

The development and application of image processing techniques to be used for fibre Bragg grating sensor measurement enhancement is an important enabler for low cost implementation.

Sub-pixel resolution

Since a FBG grating's reflection covers multiple neighbouring samples we are able to use signal processing to identify the position of the grating. This has two benefits; firstly by processing multiple measurements we increase the noise immunity, and secondly we are able to increase the resolution of the measurement to sub-pixel[1] accuracy levels.

The processing techniques can be loosely split into two categories; filtering where the data is processed in parallel by a filter kernel, and regression where the data is approximated to a function by statistical methods.

[1]The use of the the word pixel (Picture Element) stems from the application of image processing techniques to process the spectral 'picture'. One pixel can be regarded as one sample from the spectrum

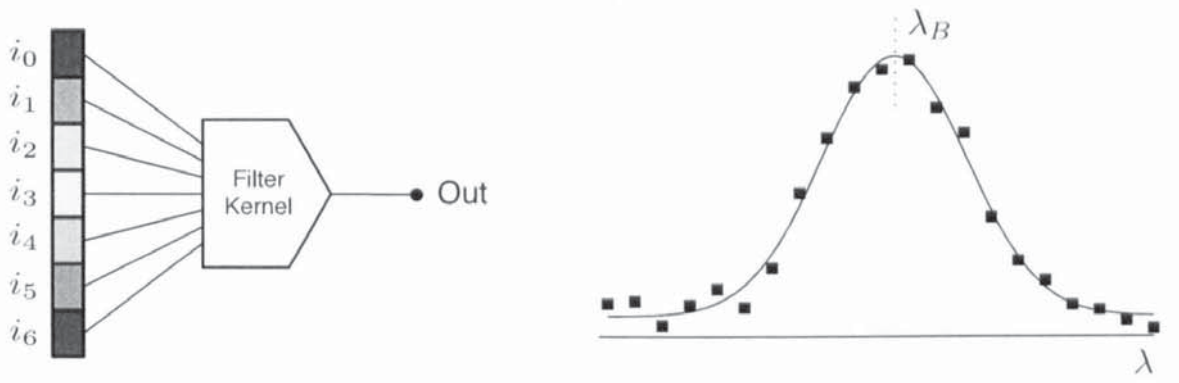

(a) Filter (b) Regression

Figure 4.2: The two different methods of processing the discrete sampled reflection from fibre Bragg gratings to find the peak position. Filter methods 4.2(a) calculate the peak directly from the sampled data using a kernel, and regression based methods 4.2(b) fit a mathematical model to the data and calculate the peak position from the model.

Filter based methods process the measurement directly (Fig. 4.2(a)), returning a result relative to the position of the data with respect to the position of the filter. Different kernels can be applied to directly calculate the Bragg wavelength [78], scan for the peak [80, 81, 82], or pre-process the spectra [83] to remove background noise.

Regressive methods attempt to approximate the data to a mathematical function using machine learning and statistical methods (Fig. 4.2(b)). Once a function has been identified the peak can be identified mathematically or using iterative methods. Polynomial [79], and Gaussian [55] models are particularly well known, however neural network models have shown promise in certain applications [84].

4.2 Evaluation of processing methods

Ultimately this study shall be applied to a real measurement system measuring FBG sensors using a CCD Spectrometer. However in order to evaluate these techniques over a wide range of resolutions and noise levels we must simulate with a flexible general model.

For evaluation and simulation purposes we simplify the problem to one of identifying

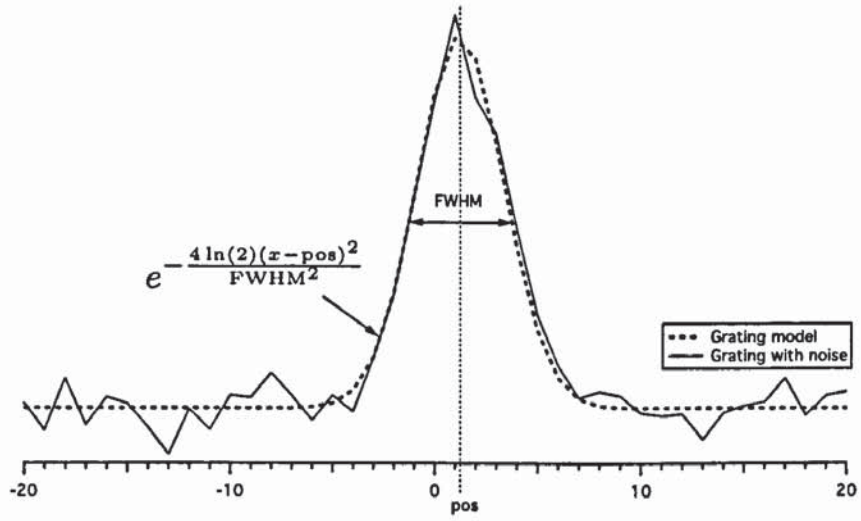

Figure 4.3: The Gaussian function fibre Bragg grating model used to evaluate each processing method.

the exact position of a sampled Gaussian function (Fig. 4.3). This simulated spectrum has Gaussian distributed noise added, which is given as a Signal-to-Noise Ratio (SNR) figure measured relative to the peak amplitude. This model allows flexibility to change both the SNR and the sample period, measured with respect to the peak's Full-Width-Half-Maximum (FWHM) value, which for a Gaussian function can be given by:

$$R(x) = e^{-\frac{4\ln(2)(x-pos)^2}{FWHM^2}} \tag{4.1}$$

where 'pos' represents the peak position.

Using this model we are able to evaluate the effectiveness of different algorithms in determining the peak position to a sub-pixel accuracy at different SNR levels for different sampling resolutions. Before presenting any novel techniques we shall investigate the two most popular methods; the Centroid Detection Algorithm, and the Least-Square Quadratic fit.

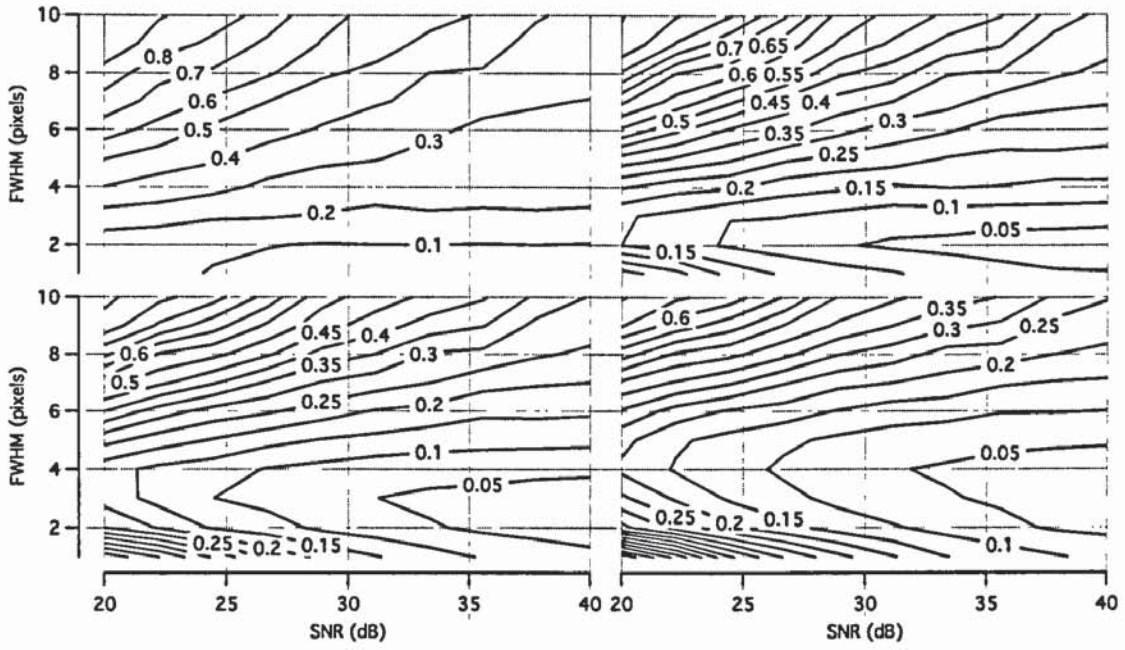

Figure 4.4: Centroid Detection Algorithm (CDA) evaluation: Contour plots of the R.M.S. error measured relative to the sample spacing, for different grating widths and noise levels. 4 different sample set sizes are presented (Top row from left; contour plots for 3, and 5 samples. Bottom row from left; contour plots for 7, and 9 samples). Optimal behaviour (minimum error) can be seen at a constant grating width for a given sample set size, independent of noise level.

Centroid Detection Algorithm

$$\lambda_B = \frac{\sum_j \lambda_j i_j}{\sum_j i_j} \tag{4.2}$$

The Centroid Detection Algorithm (CDA) method (4.2) [78] is a weighted mean calculation to determine the centre of gravity for the reflected peak. This filter calculates the first moment of an array of samples of intensity i_j at wavelengths λ_j. Whilst this only returns the exact peak of the reflection for a symmetric peak, so long as the reflection is of stable shape it does calculate a stable measurement for the Bragg wavelength.

In addition to resolving the Bragg wavelength, this algorithm has found use in applications where the reflection shape change requires quantification [85].

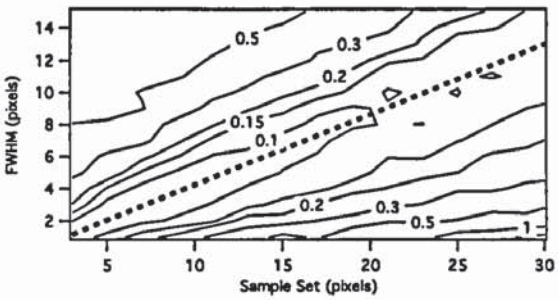

(a) Contour plot of the RMS error with respect to sample set size and grating width for the CDA method (SNR = 30dB). Dashed line approximates the valley of optimal sample set size to grating width ratio

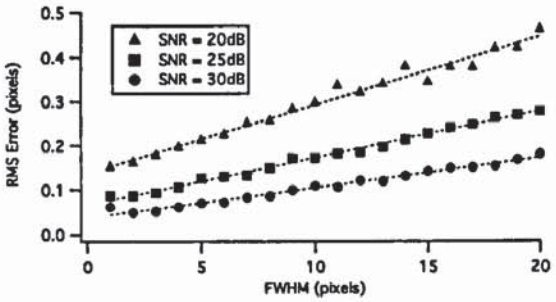

(b) RMS error with respect to grating width for optimised CDA processing at different noise levels. Sample set size is a function of grating width (= (2 × FWHM) + 1)

Figure 4.5: Optimisation of Centroid Detection Algorithm usage. From the observation of an optimal sample set size to grating width ratio (4.5(a)), we can determine the optimal characteristics of the Centroid Detection Algorithm (4.5(b))

The effectiveness of the Centroid Detection Algorithm method can be determined through simulation of the previously described model, measuring the error in resolved position for different sample set sizes (the number of data point used in the calculation) centred on the grating's measured peak value. With repetitive processing of the grating centred in different positions, the RMS error at different noise levels can be calculated relative to the grating width (measured relative to the sample spacing), for different sample set sizes (Fig. 4.4).

From the contour plots presented in Figure 4.4 we notice there to be a definite valley of minimal error for each sample set size, displaying an optimal width of grating for that particular sample set size which is independent of nose level. We can explore this further by plotting the relationship between grating width and the size of the sample set for a fixed level of noise on a separate contour plot (Fig. 4.5(a)).

From Figure 4.5(a) we can see that there is a clear linear relationship between grating width and sample set size with respect to minimal output error. Making the general approximation that sample set size N is optimal at $N = (2 \times \text{FWHM}) + 1$ we can plot the RMS error for different resolutions at different noise levels (Fig. 4.5(b)). It is clear from

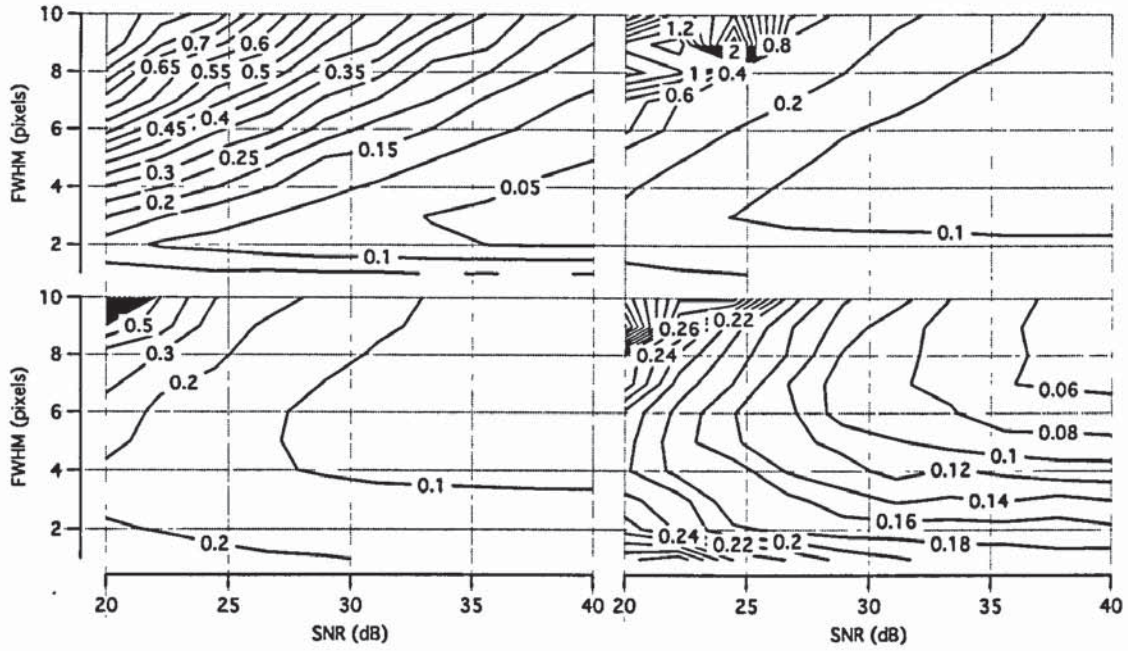

Figure 4.6: Least-Square Quadratic fit (LSQ) evaluation: Contour plots of the R.M.S. error measured relative to the sample spacing, for different grating widths and noise levels. 4 different sample set sizes are presented (Top row from left; contour plots for 3, and 5 samples. Bottom row from left; contour plots for 7, and 9 samples). Optimal behaviour (minimum error) can be seen to shift to wider grating widths as the signal-to-noise ratio increases, for a given sample set size

this that when optimised in this manner, use of Centroid Detection Algorithm method can determine the grating position to an accuracy of less than the sample spacing with low uncertainty.

Least-Square Quadratic fit

The Least-Square Quadratic fit (LSQ) method [79] is a regressive technique that fits a quadratic function to the data using a linear least-square fit. The use of a polynomial as the regression function allows a linear fit, which means that we can solve the regression *absolutely* and can do so with high precision using Singular Value Decomposition (SVD) to calculate the pseudo-inverse matrix [67]. The use of a quadratic polynomial guarantees a single peak.

This method has previously been shown to have superior accuracy and noise suppression characteristics compared to the Centroid Detection Algorithm technique [79, 55]. Repeating the same test used for the Centroid Detection Algorithm; calculating the positional error for different sample set sizes, grating widths, and noise levels (Fig. 4.6) we see that again there is a definite valley in the contour plot, indicating a specific window of optimal accuracy. However unlike the Centroid Detection Algorithm method we can see that the relationship between optimum accuracy and the sample set size to grating width ratio changes with noise level (Fig. 4.7(a)), with the peak accuracy shifting to wider gratings at lower noise levels. If we compare the results from this Least-Square Quadratic fit technique with those of the optimised Centroid Detection Algorithm detailed in the preceding section, we find there to be little benefit (Fig. 4.7(b)).

Furthermore we can see from Figure 4.8 where we analyse the error relative to the peak position for both the Centroid Detection Algorithm and Least-Square Quadratic fit methods, that the error from the LSQ method is more systematic than that of the Centroid Detection Algorithm. There is a periodicity to the mean error matching the movement of the peak position relative to the sampling points. This indicates that there is an offset to the resolved position generated by the sampling distribution. It therefore precludes the Least-Square Quadratic fit method from serious recommendation, as a greater level of uncertainty will always be present despite output filtering.

4.3 Novel processing methods

Approximation

We have shown that a significant portion of the error associated with the Least Square Quadratic fit method is systematic. In order to try and remove this noise source we shall

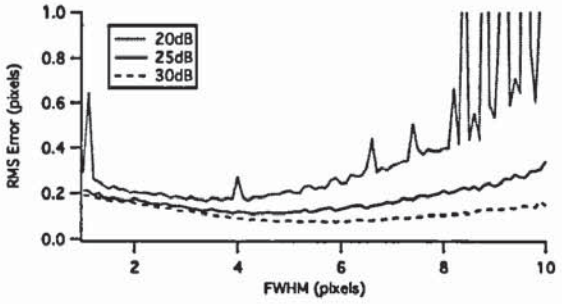

(a) Effect of noise on LSQ processing for a constant sample set size (7 samples)

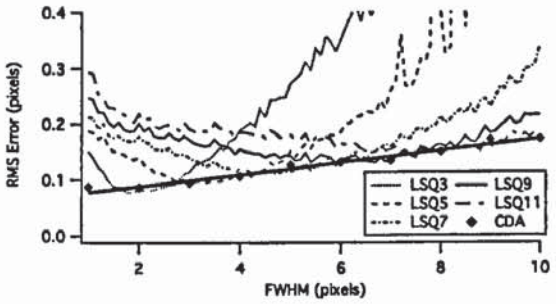

(b) Accuracy comparison against the optimised CDA method for a constant noise level (SNR = 25dB)

Figure 4.7: Analysis of Least-Square Quadratic fit accuracy: Figure 4.7(a) demontrates the shift of peak accuracy to wider grating widths at lower noise levels, and Figure 4.7(b) demonstrates there to be limited benefit of Least-Square Quadratic fit usage of over an optimised Centroid Detection Algorithm method

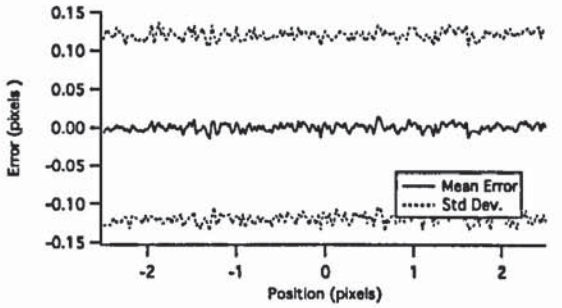

(a) Centroid Detection Algorithm (11 samples)

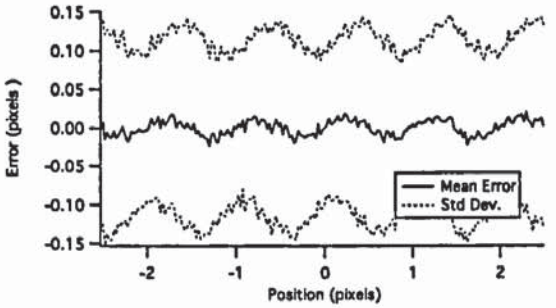

(b) Least Square Quadratic fit (7 samples)

Figure 4.8: Analysis of Positional Error (FWHM = 5, SNR = 25dB). As the peak position is moved relative to the samples we see that unlike the results from the Centroid Detection Algorithm, the error for the Least Square Quadratic fit method introduces a systematic error offset dependent upon the peak position relative to the sampling

determine whether an improved function agnostic regression technique has any bearing over system performance.

Paterno et al. [84] introduced a method using the sampled spectra as training data for a one-input / one-output Radial Basis Function Network (RBFN). This network was trained to approximate the reflection power for a given input wavelength. Following successful training the network has become a mathematical model of the FBG reflection and can be sampled to any arbitrary resolution. This method was designed to eliminate

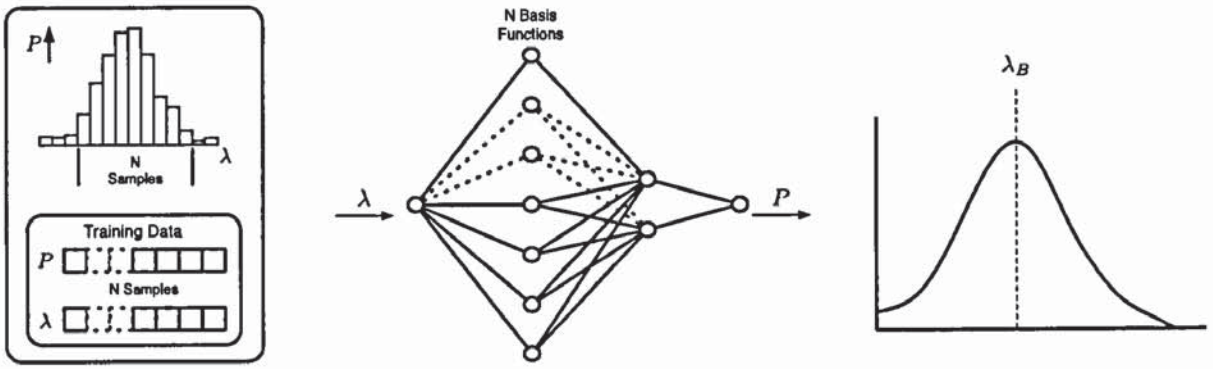

Figure 4.9: A General Regression Neural Network (GRNN) can be used to approximate FBG reflection spectra to a smooth mathematical model. The structure of the network is dependent on the number of samples used and their probability distribution.

noise and decrease uncertainty for high resolution spectra however, resolution gain for low resolution spectra is a conceivable application.

The specific network model and training method chosen for this technique relied on two factors; the basis width parameter which operates as a smoothing factor to the model, and a cross validation figure which acts as a qualitative control preventing the model from over training. However this particular method is computationally expensive and heavily based upon iteration.

The General Regression Neural Network (GRNN) [74] has been proven as an optimal method for noise suppression and function regression over most alternative methods [75, 76]. It is similar to the Radial Basis Function Network however doesn't require any iterative training. Instead its architecture is based upon the probability distribution of the training data, the data itself, and a smoothing parameter which defines the width of the network's basis functions. This makes it very fast to train, and it is guaranteed to have an optimal architecture without any need to retrain.[2]

Using this network in place of the Radial Basis Function Network (Fig. 4.9) allows regression to an optimal fibre Bragg grating model, which can be subsequently sampled

[2]Many iterative training methods contain (pseudo)-random generated numbers which means that you may not get the same model consecutively with the same data

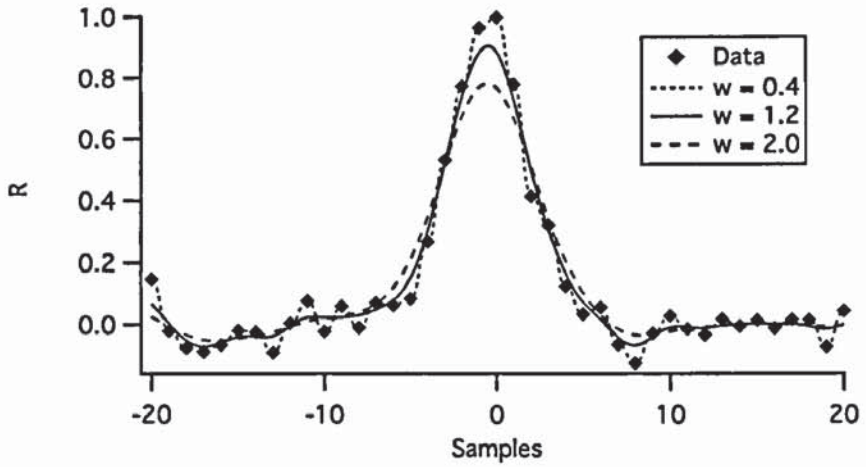

Figure 4.10: The effect of basis width w (measured in number of samples) in pixels on the approximation of a noisy sampled Gaussian function by a General Regression Neural Network (SNR=25dB)

to an arbitrary resolution in order to determine the grating peak.

Figure 4.10 illustrates this approximation in practice for a noisy sampled Gaussian function, demonstrating the effect of the radial basis width with respect to regression to an optimal waveform.

From Figure 4.10 we can see that the function smoothing (basis width) has a significant effect upon the resolved function. This clearly will have a resultant effect on the accuracy and performance of this method to identify the grating peak. Calculating the RMS error using different values of basis and grating width, for different sample set sizes (Fig. 4.11) we are able to explore the relationship between these three parameters. We can see there to be no common optimal basis width for all different sample set sizes, instead the optimal width increases with sample set size at smaller set sizes before appearing to approach an optimal value of approximately 1.8 samples for larger sample set sizes.

Using the optimal basis widths observed in Figure 4.11, we are able to calculate the positional error for different sample set sizes, grating widths, and noise levels (Fig. 4.12).

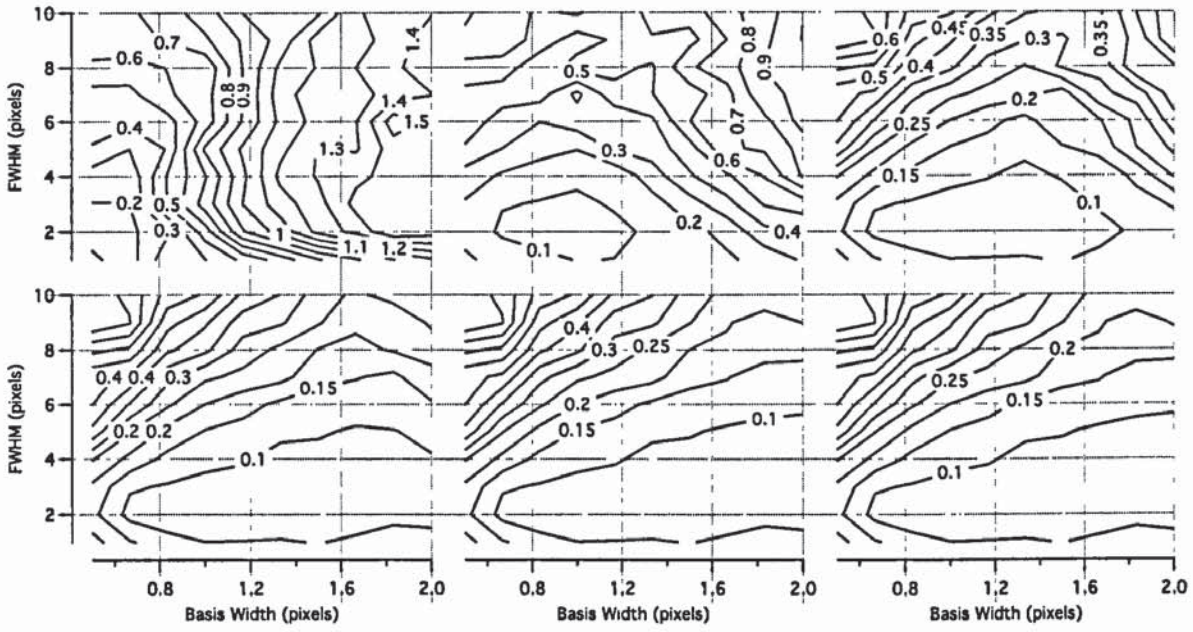

Figure 4.11: Optimal basis width evaluation for the General Regression Neural Network processing method: Contour plots of the R.M.S. error measured relative to the sample spacing, for different grating and basis widths at a constant signal-to-noise ratio (SNR = 25dB). 6 different sample set sizes are presented (Top row from left; contour plots for 3, 5, and 7 samples. Bottom row from left; contour plots for 9, 11, and 13 samples). Optimal behaviour (minimum error) can be seen for narrower gratings, and shifts to wider basis widths as the sample set size increases

We find that the General Regression Neural Network method is similar to the preceding Least Square Quadratic fit method in terms of operating window shapes, with optimal accuracy shifting to wider gratings at lower noise levels.

However the General Regression Neural Network technique can be seen to perform better than the Centroid Detection Algorithm method at low resolutions (Fig. 4.13(a)), and the systematic error seen with the Least Square Quadratic fit method has been eliminated (Fig. 4.13(b)).

Filtering

Dyer et al. [55] argue that the increased accuracy gained through approximation techniques such as the Least Square Quadratic fit, Gaussian function fits, or our General

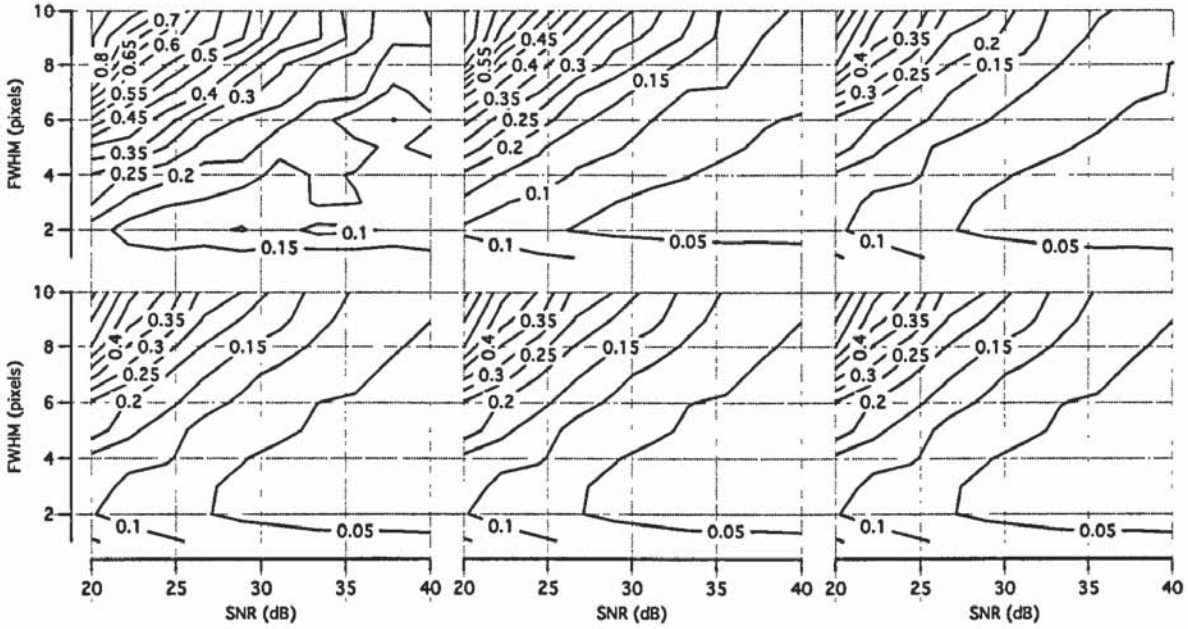

Figure 4.12: General Regression Neural Network evaluation: Contour plots of the R.M.S. error measured relative to the sample spacing, for different grating widths and noise levels. 4 different sample set sizes are presented (Top row from left; contour plots for 3 (w=0.65), 5 (w=1.0), and 7 (w=1.4) samples. Bottom row from left; contour plots for 9 (w=1.7), 11 (w=1.8), and 13 (w=1.8) samples). Optimal behaviour (minimum error) can be seen to shift to wider grating widths as the signal-to-noise ratio increases, for a given sample set size

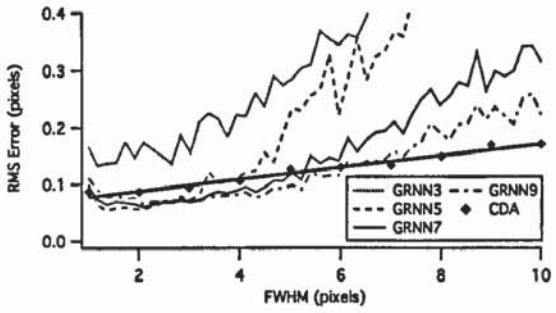

(a) Comparison with optimal CDA accuracy (SNR = 25dB)

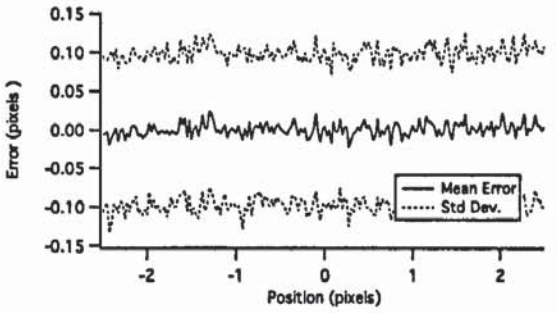

(b) Analysis of Positional Error (FWHM = 5, sample set size = 9, SNR = 25dB)

Figure 4.13: Analysis of General Regression Neural Network accuracy: The General Regression Neural Network can be seen to perform better than the Centroid Detection Algorithm method at low resolutions (Fig. 4.13(a)), and has eliminated the periodic error offset seen with the Least Square Quadratic fit method (Fig. 4.13(b)

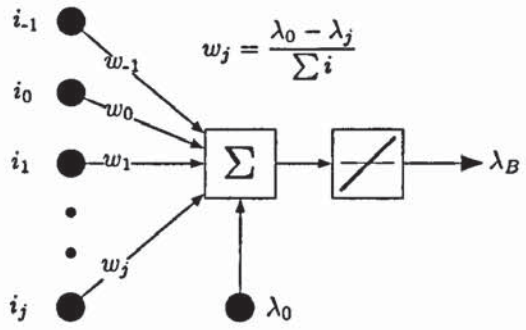

Figure 4.14: The graphical representation of the Centroid Detection Algorithm resembles an Adaptive Linear Element (ADALINE)[1]

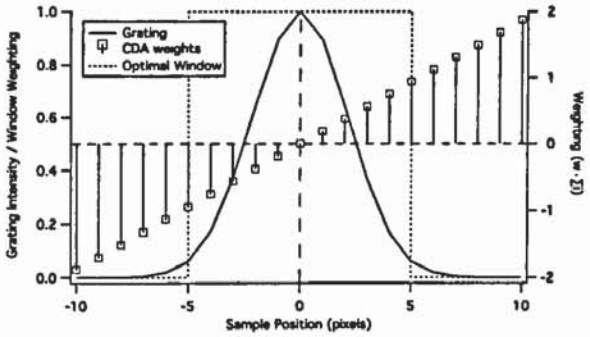

Figure 4.15: The relationship between grating, weighting, and optimal weighting window for the Rectangular Windowed Centroid Detection Algorithm (RWCDA)

Regression Neural Network method do not justify the cost of implementation. It was proposed that averaging the calculated position from less accurate filtering techniques would be more valuable.

In Section 4.2 we found there to be an optimal grating width for a particular sample size. It was found that centring the sample set on the grating and windowing it around the peak provided optimal noise suppression, as CDA_N was found to be optimal at $N = (2 \times \text{FWHM}) + 1$.

Since the Centroid Detection Algorithm is a linear calculation we can rewrite Equation 4.2 in the form:

$$\lambda_B = \lambda_0 + \sum_{j=1}^{N} w_j i_j \tag{4.3}$$

where

$$w_j = \frac{\lambda_0 - \lambda_j}{\sum i} \tag{4.4}$$

Which is the form of an Adaptive Linear Element (ADALINE)[1].

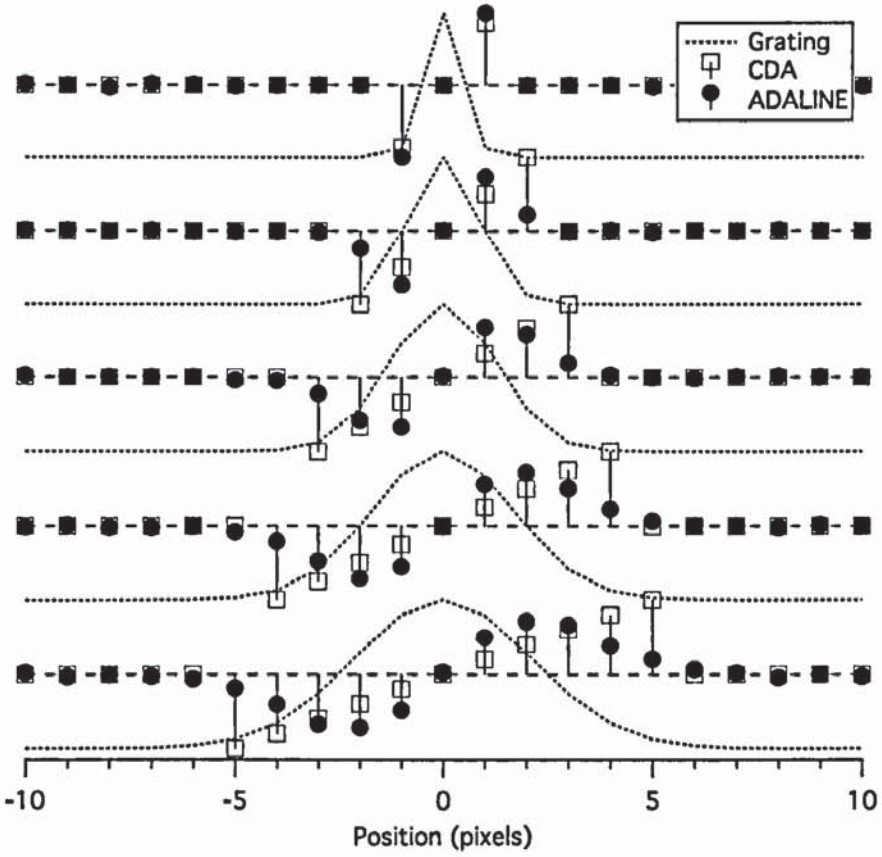

Figure 4.16: Comparison of weight distribution between optimal Rectangular Windowed Centroid Detection Algorithm and ADALINE filter kernels

Using this ADALINE visualisation of the CDA (Fig. 4.14) we can see that the synaptic weights increase linearly with distance from the bias point. Therefore in order to ensure that the weightings are kept small and that output noise is minimised we must ensure that the bias point is set to the centre of the sample. Windowing the sample set around the grating has a profound effect because the samples outside the grating peak have both high weighting and a low SNR. We denote this method as the Rectangular Windowed Centroid Detection Algorithm (RWCDA) (Fig. 4.15).

This ADALINE representation can be used as a tool to investigate the parallel filter topology further. Because it is a linear model we can perform a linear least squares fit and minimise the error function to the weighting vector required for calculating the peak position from sampled spectra for any grating shape.

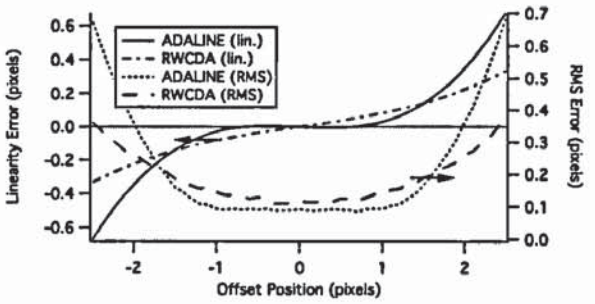

(a) Analysis of Measurement Linearity (FWHM = 5, RMS Error measured with SNR = 25dB)

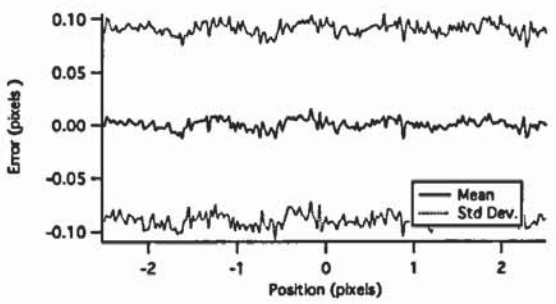

(b) Analysis of Positional Error (FWHM = 5, SNR = 25dB)

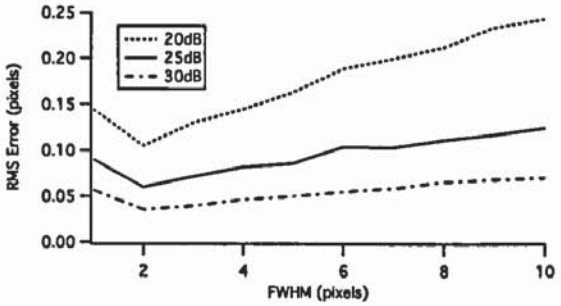

(c) RMS error with respect to function width

Figure 4.17: Analysis of optimised ADALINE filters: Figure 4.17(a) shows increased accuracy and noise suppression as the true peak deviates from the filter centre, Figure 4.17(b) displays a reduced noise level alongside a slight increase in systematic error, and Figure 4.17(c) illustrates the strong noise immunity and accuracy level offered by the technique.

Figure 4.16 shows the optimal weights for different width Gaussian functions found using a training set consisting of:

$$i_j = e^{-\frac{4\ln(2)(x_j - \mathrm{pos}_N)^2}{\mathrm{FWHM}^2}} + NF \tag{4.5}$$

where 'pos' is a vector of 10000 samples of normally distributed random numbers centred at 0 with a standard deviation of 1, and NF corresponds to a SNR of 25dB measured to the peak.

Using these calculated filter kernels we can see the optimal characteristics for the parallel filter architecture. Figure 4.17(a) displays the potential accuracy and noise suppression as the true peak deviates from the filter centre.

Figure 4.17(b) displays the introduction of slight systematic error over the Rectangular Windowed Centroid Detection Algorithm or General Regression Neural Network methods, however the surrounding noise level has been reduced. Overall we can see this to be the preferred method we have presented in terms of accuracy (Fig. 4.17(c)), especially when we start to consider speed of operation and hardware implementation.

Observing the shape of this optimal filter to be related to the underlying Gaussian function we compare the effect of using the same Gaussian function to window the CDA kernel against the optimal filter kernel predicted by the least squares fit. Iteratively we find that the optimal kernel can be approximated as:

$$w_j = \frac{2\,(\lambda_0 - \lambda_j)\,g_j}{\sum i.g} \quad \text{for} \quad \text{FWHM} \geq 1.5 \tag{4.6}$$

where g represents a sampled Gaussian fit to the grating shape. For grating width lower than this the Rectangular Windowed Centroid Detection Algorithm kernel would be preferable. The comparison between the two kernels can be seen in Figure 4.18(a). More interestingly we find that this Gaussian windowing function is near optimal for non-Gaussian profiles such as the sinc function given in Figure 4.18(b).

We denote this method as the Gaussian Windowed Centroid Detection Algorithm (GWCDA).

4.4 Temperature measurement system

In order to experimentally verify these findings and determine their effectiveness in measuring real FBG sensors we built a temperature measurement system (Fig. 4.19). For the measurement device we used an Ocean Optics HR2000 CCD Spectrometer. This was a spectrometer operating in the 800-900nm range with an approximate sample resolu-

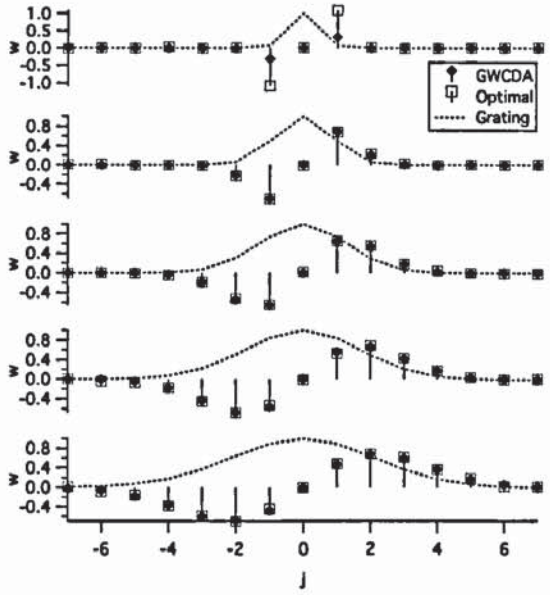

(a) GWCDA Weights for Gaussian profiled spectra

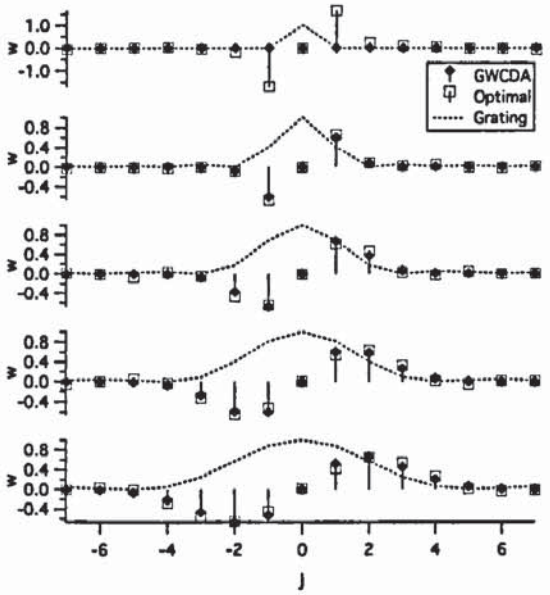

(b) GWCDA Weights for a Sinc profiled spectra

Figure 4.18: Comparison of Gaussian Windowed Centroid Detection Algorithm (GWCDA) kernels against optimised filter kernels predicted by the least square fit for different function widths / sampling rates

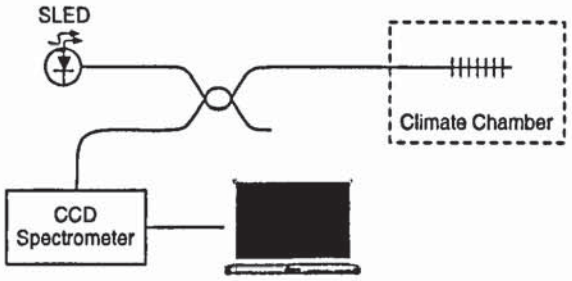

Figure 4.19: Experimental Apparatus: A superluminescent diode (SLD) acts as source for a fibre Bragg grating sensor housed in a climate controlled chamber. Reflected light is measure by a Spectrometer and processed by a personal computer

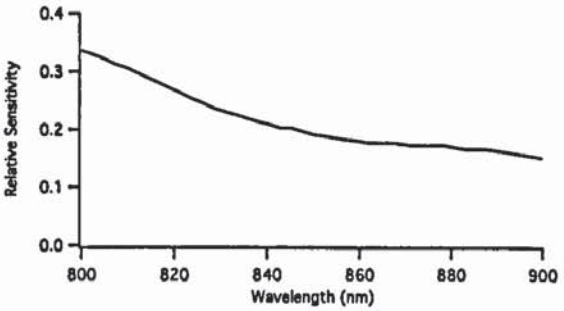

Figure 4.20: The sensitivity of the CCD imaging element used in the spectrometer (manufacturer's data)

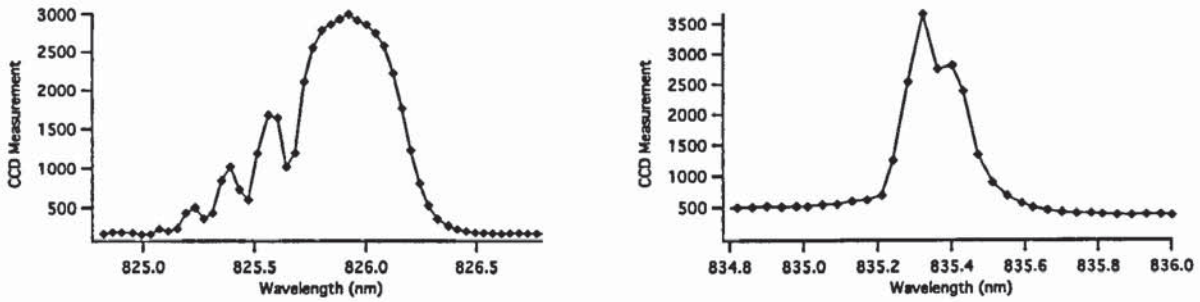

(a) Sensor A (50°C) (b) Sensor B (50°C)

Figure 4.21: FBG Temperature Sensors (as sampled by an Ocean Optics HR2000 CCD Spectrometer)

tion of 50pm. The exact wavelength linearity for the 2048 pixels was specified by the manufacturer as:

$$\lambda_n = -4.8623 \times 10^{-6} n^2 + 0.046445n + 799.087402 \quad \text{for } n = 0, 1, 2 \ldots 2047 \tag{4.7}$$

The sensitivity for the CCD detector in this range can be seen in Figure 4.20. The optical resolution is given as 5 pixels FWHM. Each measurement is sampled to 12bit precision. The device was controlled by a PC using custom software. This allowed direct access to the CCD array and control over integration and biasing. All spectral filtering was turned off, and the CCD was biased to compensate for the DC dark noise level.

The source was a SLD-381-HP superluminescent diode (SLD) manufactured by Superlum Diodes Ltd. This had a spectral centre at 822.5nm with a bandwidth of 22.2nm FWHM, and a ripple of 1.4%.

We used two different fibre Bragg gratings as the sensors. Both were inscribed using the holographic technique using a Gaussian beam approximately 5mm wide, and both were annealed to 120°C for over 48 hours. Sensor A (Fig. 4.21(a)) had a strong index profile, requiring a very short CCD integration time. Sensor B (Fig. 4.21(b)) had a weak index profile, requiring a longer integration time.

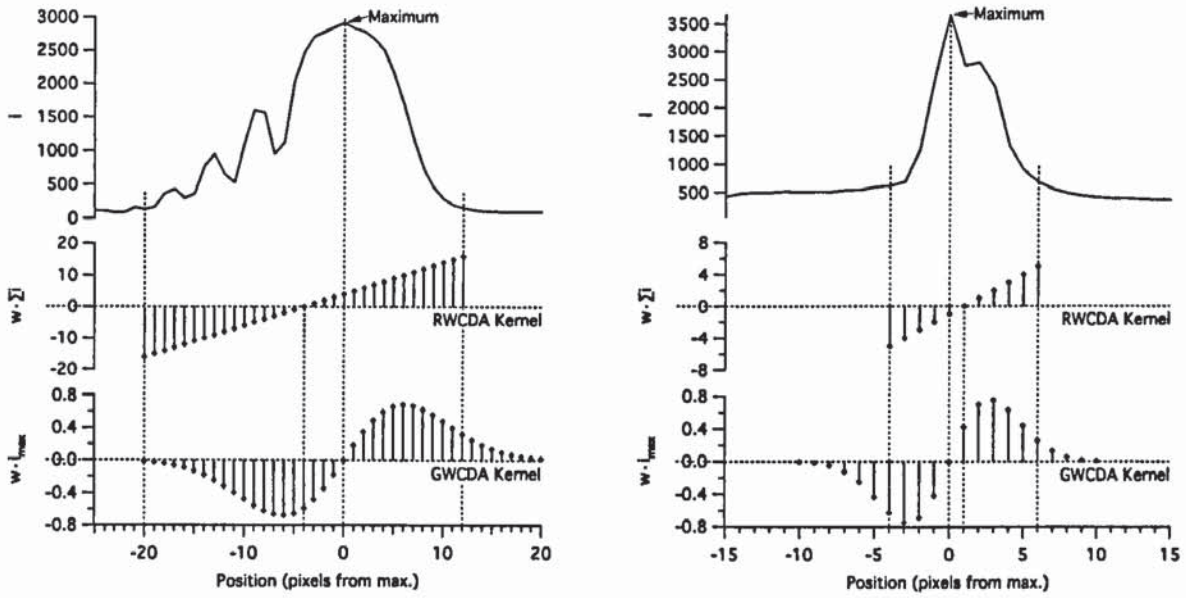

(a) Sensor A (b) Sensor B

Figure 4.22: Filter Design: The design of each filter kernel is made relative to each grating shape. Rectangular windowed filters are centred on and cover the entire reflection, Gaussian windowed filters are centred by and calculated from the least mean fit of a Gaussian function.

With the two gratings shapes known we can determine the filter kernels for the Rectangular Windowed Centroid Detection Algorithm method, and calculate those for the Gaussian Windowed Centroid Detection Algorithm filters based upon a least square fit of a Gaussian function to the grating reflection. The weightings for each of these can be seen in Figure 4.22.

Individually the gratings were placed in a Sanyo environmental chamber and the spectrum was measured at 5°C intervals between 0 and 100 °C. The spectrum was sampled 20 times for each measurement step.

In order to verify the optimal sample size for the Least Square Quadratic fit algorithm we process the reflected spectrum from this temperature testing using 5, 7, 9, and 11 sample set lengths, each centred upon the measured peak pixel. Shown in Figure 4.23 are the processed results for both sensors. Here we plot the mean resolved wavelength and the residual from a straight line linear least squares fit to the mean of the 20 readings

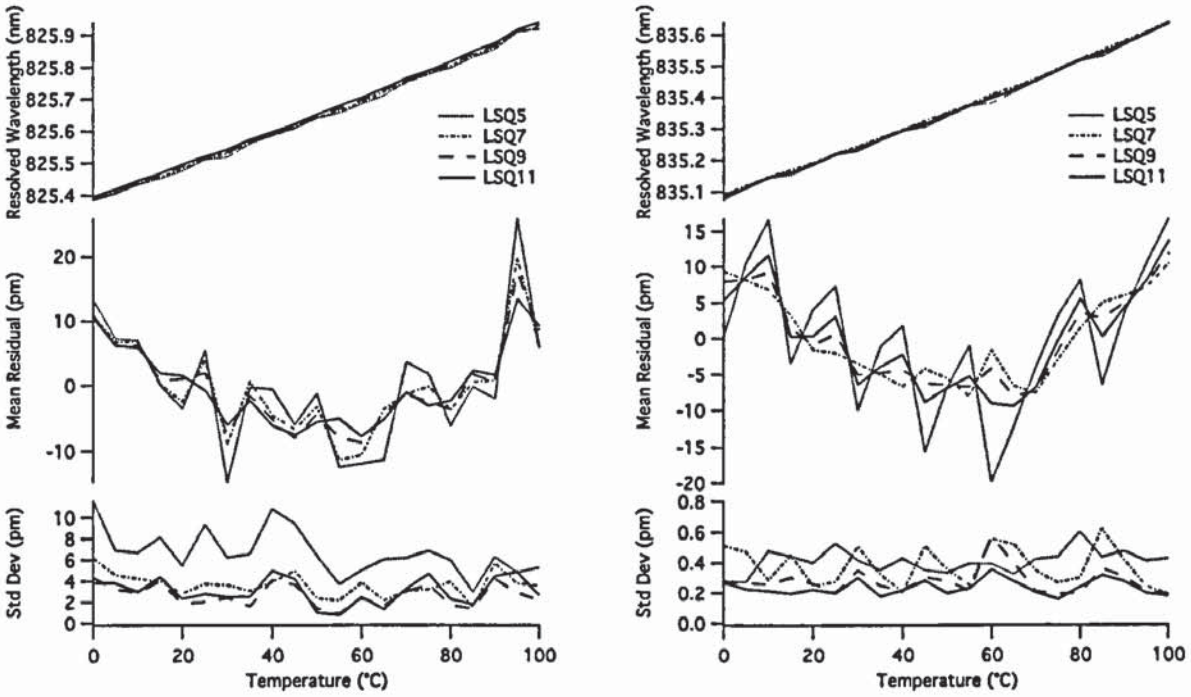

(a) Sensor A (b) Sensor B

Figure 4.23: FBG temperature sensing using the Least Square Quadratic fit processing method: Mean resolved wavelength is displayed with respect to temperature for different sample set sizes (Top), with the residual from a straight line fit shown in the centre plot and the measurement standard deviation in the lower plot. Optimal behaviour for sensor A occurs with a sample set length of 11 samples, whereas for sensor B the optimal length is 9 samples.

taken. In addition to this mean we plot the standard deviation of measurements in order to gain an insight into noise rejection capability. We can see clearly the fibre Bragg grating's thermo-optic non-linearity on both plots [86], and can see that the 11 sample Least Square Quadratic fit performs best with sensor A, whilst the 9 sample fit appears more accurate for sensor B though with a slightly increased uncertainty.

Repeating this to identify the optimal sample set length for Generalised Regression Neural Network processing (Fig. 4.24) shows the Generalised Regression Neural Network to perform best with a larger data set for both sensors A and B, both in terms of accuracy and uncertainty.

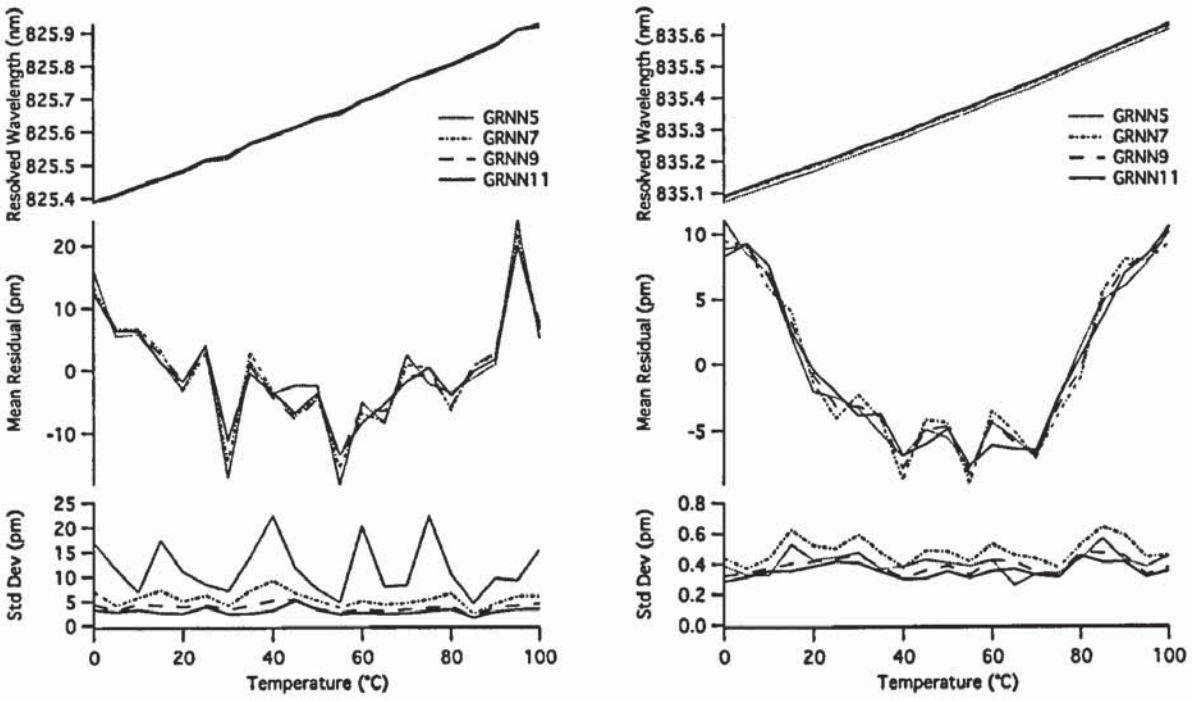

(a) Sensor A (b) Sensor B

Figure 4.24: FBG temperature sensing using the Generalised Regression Neural Network processing method: Mean resolved wavelength is displayed with respect to temperature (Top), with the residual from a straight line fit shown in the centre plot and the measurement standard deviation in the lower plot. Optimal behaviour for both sensors occurs with a sample set length of 11 samples.

Comparing the four algorithms together (Fig. 4.25) we can see the Gaussian Windowed Centroid Detection Algorithm technique to be clearly optimal for the larger stronger grating sensor A. For sensor B we find that the Generalised Regression Neural Network method is optimal in terms of mean accuracy, for a larger uncertainty. Against the other traces we can see that the Least Square Quadratic fit method is starting to demonstrate some of the systematic uncertainty illustrated in earlier simulations. If we consider uncertainty we find that it is again the parallel Gaussian Windowed Centroid Detection Algorithm which proves optimal of the 4 different methods.

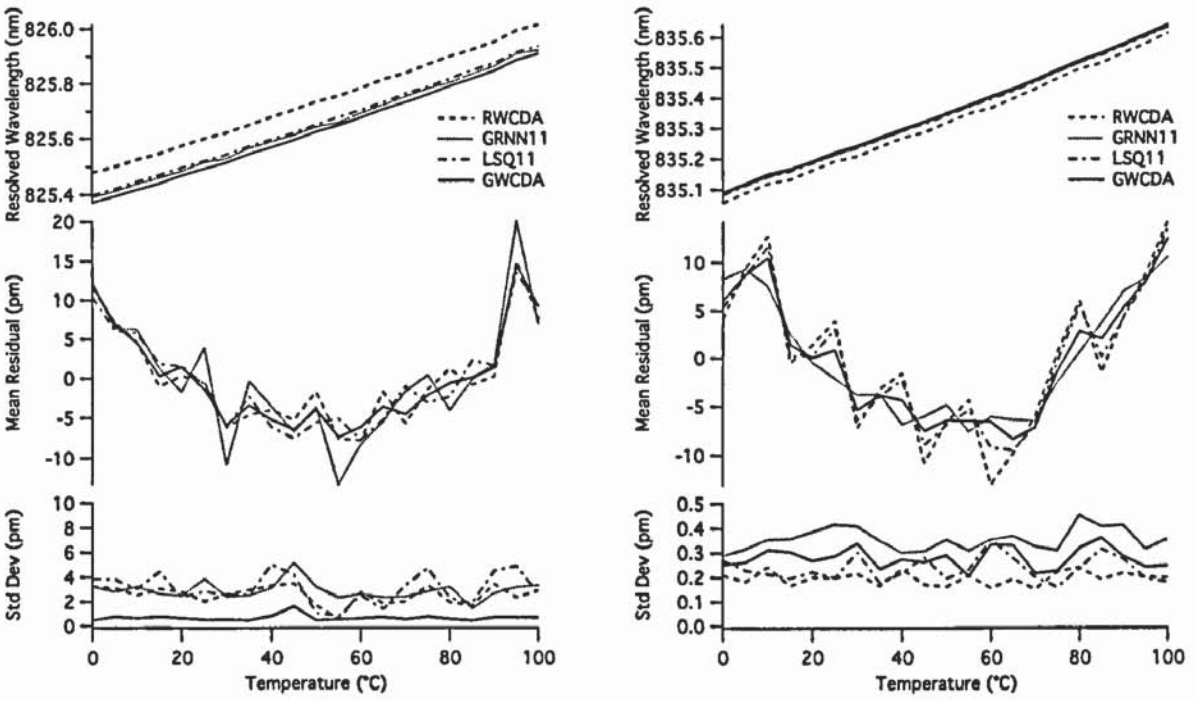

(a) Sensor A (b) Sensor B

Figure 4.25: FBG temperature sensing using RWCDA, GWCDA, LSQ and GRNN processing methods: Mean resolved wavelength is displayed with respect to temperature (Top), with the residual from a straight line fit shown in the centre plot and the measurement standard deviation in the lower plot. Optimal behaviour can be seen using the GWCDA method, given its high performance and high noise rejection (low standard deviation).

4.5 Conclusion

The benefits of applying image processing techniques to process fibre Bragg grating reflection spectra have been clearly demonstrated. Their usage for resolution enhancement and noise suppression has been comprehensively evaluated in a function and resolution agnostic manner.

We have evaluated two established processing techniques, showing benefits and limitations to their implementation, and from the evaluation of these methods have developed two novel processing techniques.

Using a Generalised Regression Neural Network (GRNN) to approximate and model the FBG reflection we are able to remove systematic errors induced by more restrictive fitting

methods such as the Least Square Quadratic fit method. This method proved to perform better than the Least Square Quadratic fit in both simulation and experimental testing with observing resolution gains of greater than 10× in the presence of high background noise.

However it is the application of windowing techniques to the Centroid Detection Algorithm that has demonstrated the most potential. Through the application of machine learning as a tool to investigate filter weighting we were able to demonstrate what is the statistically optimal parallel filter architecture for noise suppression. Further analysis showed that this was proportional to a Gaussian function fit of the reflection which we have denoted as the Gaussian Windowed Centroid Detection Algorithm.

This method has proven optimal in both simulation and practical testing, demonstrating low variance and optimal accuracy. With a working qualitative test now available, future work could focus on the development of a generalised window model for arbitrary grating shapes. Or given the parallel nature of the filter, work could focus on a discrete real-time practical implementation for use with an Arrayed Waveguide Grating (AWG) FBG interrogation scheme [87].

Chapter 5

Tactile Sensing Surface

A tactile sensor can be defined as *'a device or system that can measure a given property of an object or contact event through physical contact between the sensor and the object'*[88]. This illustrates that touch is a multifaceted sensation, and encompasses a wide range of quantifiable measurements and subsequently a wide range of measurement techniques.

In this chapter we shall concentrate upon measurement using a matrix of sensors in conjunction with a surface or skin, otherwise know as *cutaneous sensing.* First we will present an overview of cutaneous sensing methods, focusing on the evolution of efficient and scaleable methods. Secondly we present the development of a novel distributive strain sensor architecture using a network of fibre Bragg gratings. Finally we present the proof of principle study for this system as part of a tactile sensing surface.

5.1 Cutaneous sensing

Cutaneous sensors are possibly the most studied form of tactile sensor, primarily because the presence of a skin allows the conception of devices that mimic human touch. This distributive measurement of contact between a skin and an object is an area of great

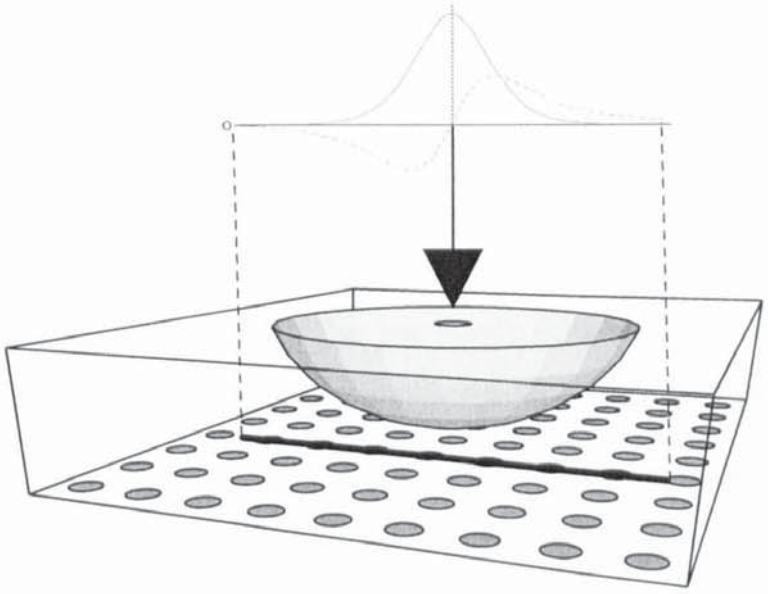

Figure 5.1: Cutaneous sensing: Extrinsic sensors measuring the radial strain distribution from a point load (shear and normal stress denoted by dashed and solid plots respectively [2])

interest for a variety of applications such as industrial manufacturing and minimal invasive surgery [88, 89], which lead to a wide range of possible implementations.

The field of cutaneous sensing can be further split into two predominant categories; intrinsic where the skin and sensors are integrated, and extrinsic where the skin forms a protective cover over a substrate mounted sensor matrix or the skin is the substrate to a sensor matrix. Extrinsic sensors carry the largest volume of research, as typically they are able to measure the finest feature size.

Small scale feature resolution is the driving force for most tactile sensing research. With the vast majority of sensor types being extrinsic sensors measuring force normal to the skin (Fig. 5.1), the limiting factor is the non-linearity between the deformation and the resultant measured force. Additionally since the internal stresses are radial from the point of deformation, the measurement 'image' from anything other than a point load suffers from a high level of measurement overlap due to stress dispersion. This is particularly so

with thick skins or materials with a high Poisson's ratio [90]. From this it is clear that it is the skin's material properties that predominantly govern the sensor's accuracy.

There has been a large amount of research into the best way to model the skin's behaviour when deformed. This includes traditional mechanics [91], Singular Value Decomposition (SVD) and Finite Element Analysis (FEA) [92], and Fourier decomposition [93]. One of the most successful methods has been to use neural networks to approximate the transfer function correctly. This has proven optimal on a number of occasions [94, 95, 94, 96], and is straightforward to implement for arbitrary systems.

Intrinsic sensors however try to limit the influence of stress superposition by measuring near surface strain. Embedded strain sensors measure the shear strain of the surface, and from this calculate the deformation profile. Optical fibre sensors such as fibre Bragg gratings are ideal for embedding within a surface structure. With this application in mind, Moiré Grating based strain sensors have been developed with very fine spatial accuracy [97].

In order to have a high strain coupling coefficient, the skin material needs to be fairly stiff, with a large Poisson's ratio. However the mechanical characteristics of the sensor dominate that of the skin.

Distributive Tactile Sensing

Although most tactile sensing methods measure and process a distributed signal, the discipline of Distributive Tactile Sensing (DTS) focuses on a different aspect of tactile sensing; efficiency.

Distributive Tactile Sensing (DTS) [98] is an elegant measurement method utilising the crosstalk between a set of sensors to enhance measurement. This methodology is in direct contrast with the techniques described in the preceding section, where crosstalk and superposition would be considered as a noise source and ideally isolated from each

measurement. The specific benefit DTS has over other direct measurement techniques is that the required concentration of sensors for a specific accuracy is typically significantly lower.

The method presented by Ellis et al. [98] uses sparse localised strain measurements to calculate the deformation profile of a thin homogeneous surface. Its effectiveness is delivered by two factors; the surface should be thin and stiff, this ensures that the radiated stress covers a large distance (and thus multiple sensors), and the surface should be fixed such that the elastic deformation is repeatable with and predictable for each contact condition deformation. This type of mechanical system can be readily modelled by mechanical theory, and therefore by measuring the surface strain or deflection at different locations it is straightforward to calculate information about the contact condition from the mathematical model.

The use of these linear models do ultimately limit the potential system accuracy, since material defects, construction variance, and elastic non-linearity all have a potential impact on fine scale resolution [93]. Neural network approximation has been identified as a potential technique to overcome this limitation, and derive a system model purely through experimental measurement of the system. This methodology has proved successful for a variety of applications and sensor types [99, 100, 101], and removes the need to perform Finite Element Analysis (FEA) upon each measurement system.

DTS using optical fibre sensors

The value of optical fibre based sensors has already been recognised for use in conjunction with DTS, and has been explored in a number of experiments. Brett and Stone [99] used simple bend sensors whose transmission efficiency was proportional to the fibre curvature. Whilst low cost in implementation, this sensing topology does not scale as it requires dedicated fibres and receivers for each sensor. In addition to this the sensors

use mechanical alignment for the measurement condition, which raises both noise and reliability concerns.

Cowie et al. [101] introduced a more advanced topology based upon fibre Bragg gratings. This enabled a system which can multiplex the sensors in the wavelength domain. This method proved very successful in terms of accuracy, and gave an increased reliability level. However the technique is heavily reliant on fine-scale wavelength measurement, which significantly increases both cost and system response time.

5.2 Low cost optical implementation

The sensor measurement system used in [101] was based on a standard wavelength multiplexed design using an OSA for the spectral interrogation. To reduce the system cost we could replace the optical spectrum analyser with a low-resolution device such as a spectrometer, and apply the processing techniques described in Chapter 4. However this is still a rather expensive solution, and the speed of operation is hampered by the acquisition and conversion speed.

A different solution would be to base the system on the edge-filtering interrogation method described in Section 2.3. This would increase the measurement bandwidth considerably and reduce the cost further. Given the multiplexing requirement, implementations derived from those of Fallon et al. [102] were thought most suitable. However as a low-cost system there is a concern with respect to the ultimate scalability. Each sensor measurement is absolute, and requires a dedicated and stable filter arrangement to both separate the sensor response and also to resolve the sensor's measurement. The concern here is that the absolute accuracy is totally dependent upon the efficiency of this stabilisation which becomes more difficult to guarantee as the system scales. The filtering complexity also increases as the number of sensors increase.

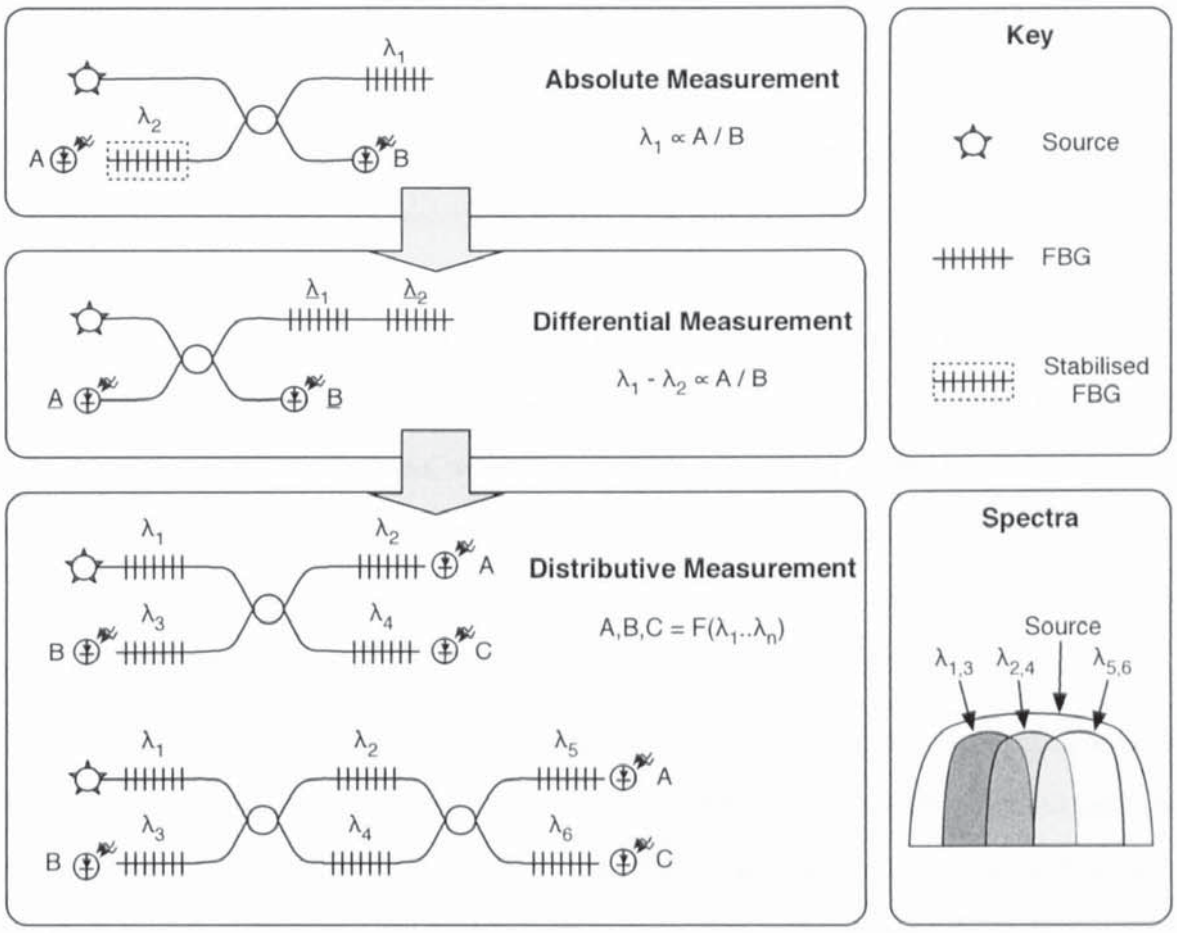

Figure 5.2: Evolution of the Overlapping Gratings Sensor Network (OGSN) topology: Edge filter fibre Bragg grating measurement [3] can be realised as a differential measurement between two sensors where the power measured at receivers A and B is directly proportional to the difference between sensors λ_1 and λ_2. This concept can be extended to include multiple gratings and multiple filter paths such that the receivers measure the response proportional to distributed measurement between sensors

Overlapping Gratings Sensor Network

Conceptual Development

Given that the DTS method uses a distributive measurement, it stands to reason that the measurement system does not need to make *absolute* measurements. We therefore designed a new topology based on and extending the edge-filter method's differential measurement mode, creating a new architecture that is both scalable and *distributive* in

measurement.

The evolution of this concept can be seen in Figure 5.2, where an implementation of the edge-filter topology using overlapping FBGs is shown in both absolute and differential modes. In both cases the measurement is given by the ratio between receivers A and B. Since the absolute measurement is not essential for this application, a differential measurement would return a more informative measurement measuring two locations *with the same number of FBG sensors.* In addition to this it negates the need for environmental stabilisation in situations where the two sensors are in close thermal contact for strain measurement applications such as a tactile sensor or have identical strain relief for temperature measurement systems. However this differential measurement cannot be extended to include a further gratings in series without loss of information.

The Overlapping Gratings Sensor Network (OGSN) topology extends the differential configuration further by creating multiple filtering paths to each of the different receivers thus creating a *distributive* response. In an OGSN system a shift in wavelength for one FBG sensor affects the power at multiple receivers simultaneously, with the ratio between receivers A,B, and C determining the distributed measurement. If the sensors are in thermal contact with each other and do not shift beyond the edges of the source, temperature will not effect the measurement of distributed strain[1].

Since the topology returns a ratiometric response relative to the distributed measurement it is analogous to the distributive measurement of a surface. Therefore by restricting the movement of the sensors like the DTS surface we should be able to apply the same techniques to calculate the distributive measurement. This restriction could be performed simply by fixing the OGSN network to a conventional (fixed) DTS measurement system, thus effectively convolving the two response functions together which in turn could be modelled or approximated by neural network regression.

Conventional edge-filter methods use a ratiometric measurement against the source

[1]This assumes a flat source spectrum

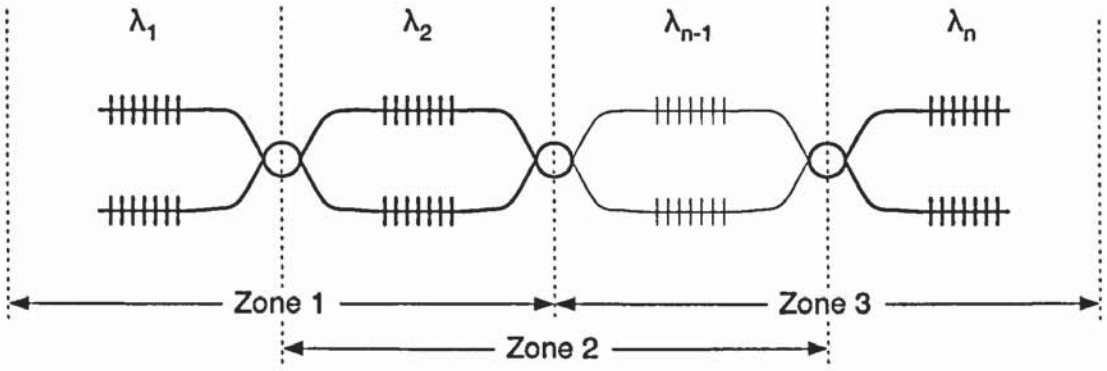

(a) 2x2 Coupler Network

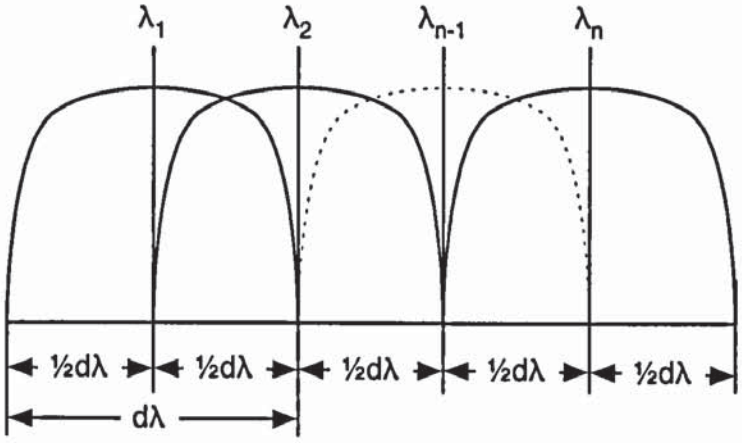

(b) OGSN Spectra

Figure 5.3: Overlaping Gratings Sensing Networks: The principle of the network is that interaction between sensors shall only occur within specified 'zones', which are centred upon the intersecting couplers (Fig. 5.3(a)). Limiting the sensor movement such that wavelength shift and spacing between sensors is limited to that of half the grating width (Fig. 5.3(b)), ensures that interaction only happens inside each zone

strength to mitigate any change in signal strength not attributed to the measurement. It was envisaged that with suitable training data the OGSN neural network could be trained to identify and compensate for change in source strength.

There are an infinite number of possible implementations of an OGSN, and whilst not necessary or practical to generate a generalised model we can describe the basic concept of operation. In figure 5.3 we present an example of an OGSN; a 2x2 coupler design with

the maximum number of sensors in place.

Each network is arranged into 'zones' where filter pairs act upon each other. These zones are centred upon each coupler such that gratings interact on either side of the coupler. Given that the sensors have an operational range of the overlap between sensors ($\frac{1}{2}$ grating width) interaction only occurs inside each zone.

The attenuation of the coupler also creates dominant signals within each zone. Signals reflected by multiple sensors are greatly attenuated in comparison with the primary signals. This contributes towards a conceptual structure much like the surface system this is driven by, where there is a high level of crosstalk between sensors and a level of attenuation for 'distant' sensors.

5.3 System Evaluation

In order to gauge the effectiveness of the OGSN method as part of a tactile sensing surface system, we evaluated against a set of specific performance attributes.

- Positional accuracy across the surface.
- Feature extraction
- Effectiveness against temperature variation
- Effectiveness against source strength variation

System Overview

The test system can be loosely split in two parts; the mechanical system, and the optical system.

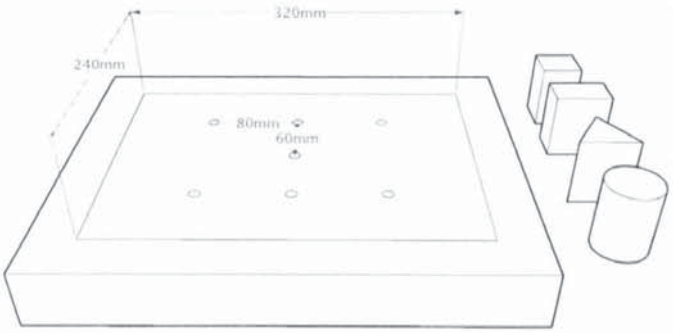

(a) Sensing Surface

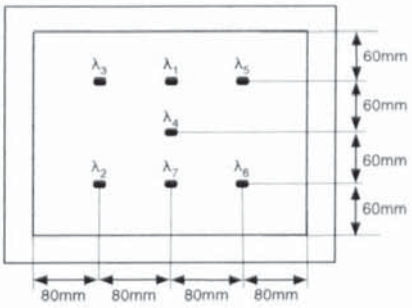

(b) Sensor Positions (from above)

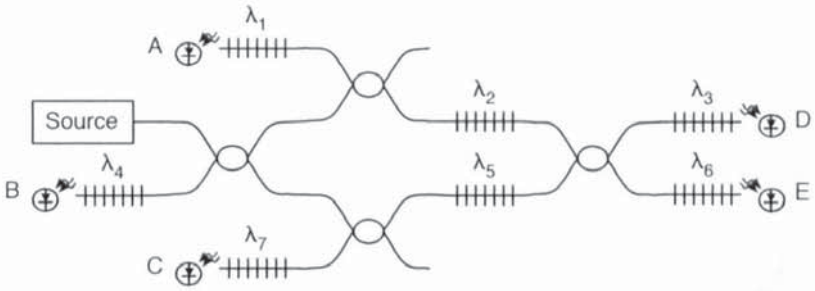

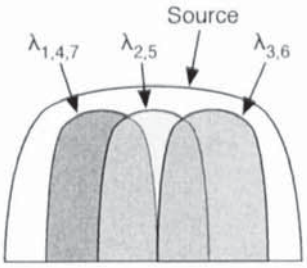

(c) OGSN network used with the surface experiment

Figure 5.4: Tactile surface system: A supported metal plate (Fig. 5.4(a) carries a seven sensor Overlapping Grating Sensor Network (Fig. 5.4(c)), each sensor measuring the point strain in line with the long edge of the plate. In order to create a distinctive measurement output function, the sensor layout was designed to minimise strain overlap between paralleled sensors (Fig. 5.4(b))

The mechanical system (Fig. 5.4(a)) comprised a rectangular 0.5mm thick steel plate, fixed and supported on all four sides by a 45mm wide framework to which the plate was bolted. The unsupported region measured 320x240mm with 7 sensors fixed to the bottom of the surface, arranged on a 60x80mm grid measuring strain in the direction of the long edge.

The optical system used in conjunction with this surface can be seen in figure 5.4(c). The seven sensor OGSN comprised 10mm long 1.5nm spectral width chirped fibre Bragg gratings (CFBG) sensors, each identically inscribed at the same wavelength[2] using the dithered pulse phasemask method described in section 2.2. These sensors had a peak

[2]The zero-strain Bragg wavelength tuning was to be performed by fixing the grating to the surface under strain in order to mitigate wavelength shift by inscription method or annealling

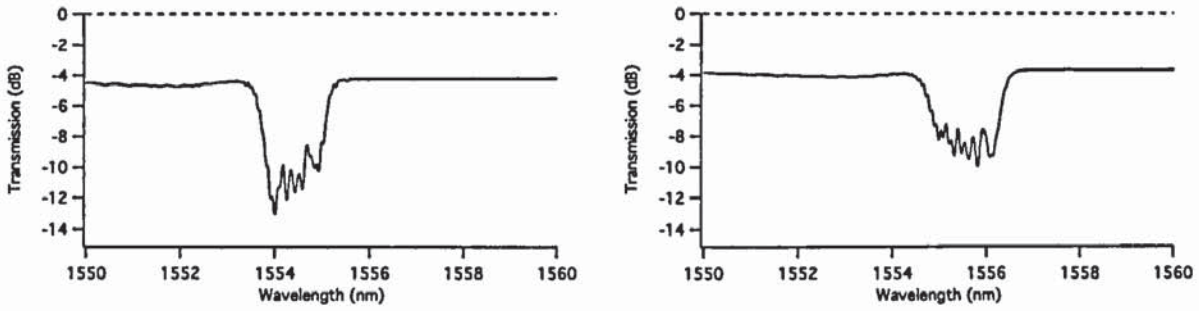

(a) λ_1 (b) λ_3

Figure 5.5: Fibre Bragg grating sensor spectra: The transmission spectra of two of the seven fibre Bragg gratings as fixed to the sensor surface (Transmission loss may be subject to a measurement system offset)

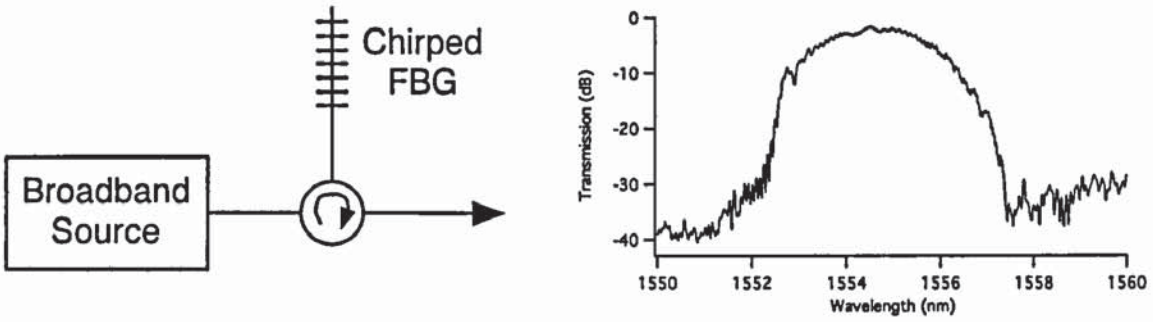

(a) Source Configuration

(b) Transmission spectrum of circulator and chirped fibre Bragg grating

Figure 5.6: Measurement system source: The source used for the seven sensor network consisted of a broadband source reflected off a chirped fibre Bragg grating. The transmission spectrum of the circulator and grating combination can be seen in Figure 5.6(b)

reflection strength of approximately 10dB, and had been annealed at 90°C for longer than 48 hours to ensure stability.

Each sensor was fixed with epoxy resin to the surface under strain in order to meet the individual wavelength criteria (Fig. 5.5). In order to create a distinctive measurement output function, the layout was designed to minimise strain overlap between paralleled sensors such as λ_2 and λ_5, or λ_3 and λ_6 (Figure 5.4(b)), ensuring that no two outputs had similar motion.

The source was implemented by reflecting light from a commercial erbium ASE source (AFC Tech. BBS1550) off a 7nm wide chirped grating centred at 1554nm (Fig. 5.6), again inscribed using the direct write inscription technique[3]. The photodiodes were low cost free space devices simply glued into position, and the couplers were low cost communication band devices.

Neural Network Training

The system performance and integrity is ultimately dependant upon the ability to create an efficient and well approximated neural network. For this proof of principle work we replicated the proven method demonstrated by Cowie et al. [101] (Figure 5.7).

The network architecture for all tests was a single hidden layer Multilayer Perceptron. The activation function used inside the network was a 'softmax' function [66] for the classification tests, and a linear function for all function regression tests.

The training was performed iteratively using a scaled conjugate gradient algorithm provided by the NETLAB MATLAB library [77]. Error minimisation against separate data was sought through the adjustment of hidden nodes, and the number of training iterations (Fig. 5.7).

Test Results

Positional Accuracy

In order to test the positional accuracy of the system, we moved a 1.6kg square mass with a contact area of 2500mm^2 over a central region measuring 240x160mm, collecting

[3]This arrangement was designed to simulate approximately the output from a low cost multimode diode laser

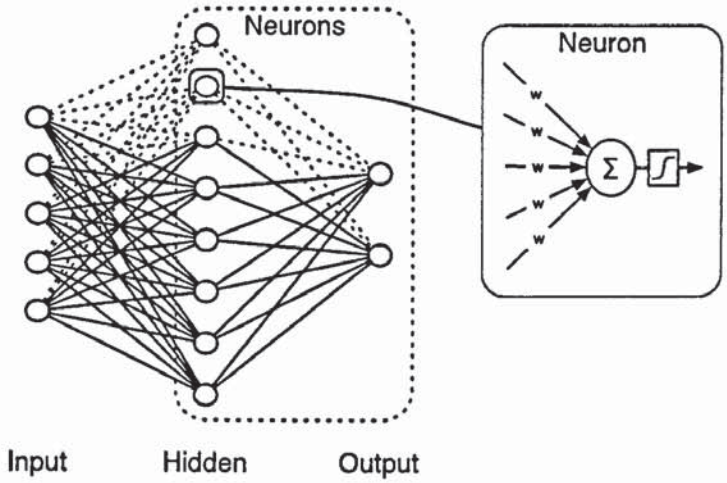

(a) Multilayer Perceptron

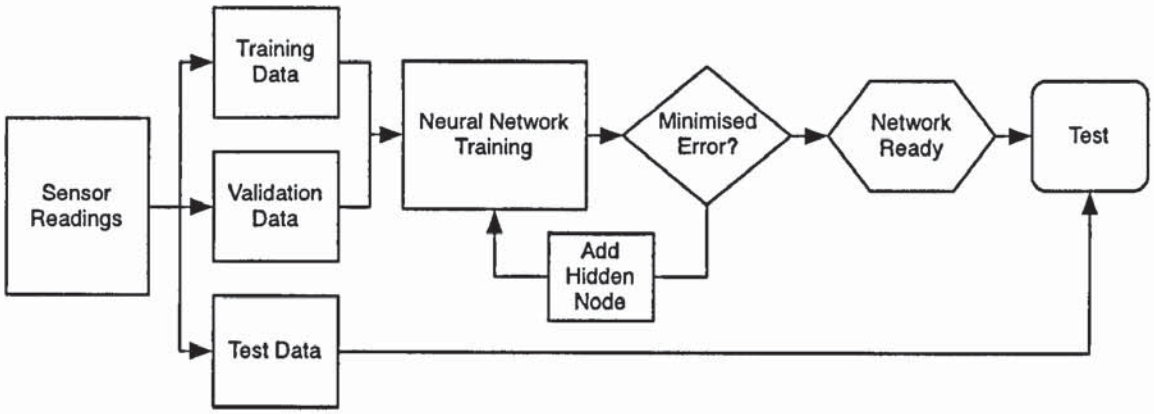

(b) Training Cycle

Figure 5.7: Neural Network Training: A single hidden layer Multilayer Perceptron network was used to process the data (Fig. 5.7(a)), with the optimal architecture determined iteratively from measured data (Fig. 5.7(b))

multiple set of data for the receiver level at each position. Training an MLP by the method shown in Figure 5.7 we found an optimal network with a single hidden layer of 49 nodes achieves an absolute position accuracy of 7.0mm (rms) for a shape placed anywhere on the surface. This accuracy is considerably better than the minimum sensor spacing of 60 mm. The distribution of the spatial accuracy as a function of position can be seen in Figure 5.8. This illustrates a fairly even accuracy across the entire surface which is slightly increased near gratings λ_3 and λ_5, and has an area of increased uncertainty near λ_6.

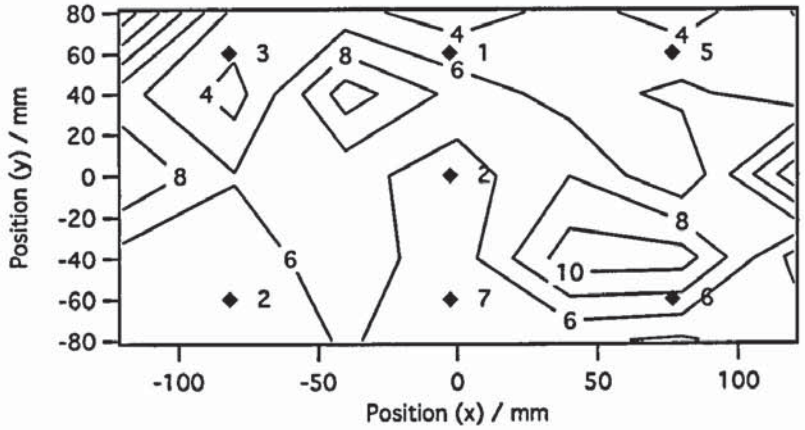

Figure 5.8: Positional accuracy for the OGSN surface system: Contour plot illustrating the RMS error (mm) with respect to position. Markers denote the fibre Bragg grating sensor positions.

Feature Resolution

Test	Circle	Square	Rectangle	Triangle
Shape Identification	100%	100%	100%	100%
Rotation RMS Error	-	6.6°	7.8°	7.3°

Table 5.1: Shape testing: Accuracy of shape classification, and RMS error in rotation resolution

The feature resolution was tested using four different shapes (circle, square, rectangle, and triangle) placed in the centre of the surface. Each of the four shapes were of solid steel, and were of equal surface area (2500mm^2) and mass (1.6kg). Parallel neural networks were trained to classify the shapes, and also to resolve the angle of orientation. Classification was achieved with 100% accuracy, and the angle of rotation to within 7 degrees for the square, triangular and rectangular objects (Table 5.1).

Stability Verification

To evaluate the potential for the signal processing to mitigate external influences, the position test was repeated at different times with different ambient temperatures (varying

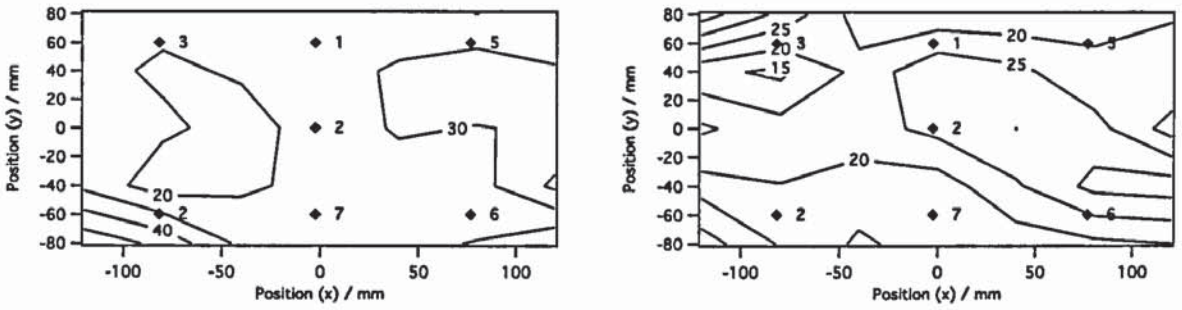

(a) System power variance by 50%

(b) Ambient temperature variance of 5°Celsius

Figure 5.9: Stability Accuracy: Contour plots illustrating the RMS error (mm) with respect to position. Markers denote the fibre Bragg grating sensor positions.

by 5°Celsius) and with different source power levels.

By retraining the same neural network configuration (49 hidden nodes) we obtained an average positional resolution of 27.4mm (rms) when exposed to source power fluctuations of greater than 50%. In a separate experiment, the retrained network returned a resolution of 23.4mm (rms) when exposed to ambient temperature changes of 5°Celsius. The effect of these changes can be seen in Figures 5.9(a) and 5.9(b) respectively.

Long Term Verification

Long term testing reduced the achievable accuracy of the system. It was found that the long term system drift caused a large variance on each of the receiver signals. This dramatically affected the neural networks performance, which were unable to minimise to a correct approximation solution. The most likely causes of drift was deemed to be temperature related, either from a temperature gradient over the sensing surface or from the source and sensor gratings not having 'top-hat' spectra.

OGSN	Cowie et al. [85]
7 FBGs (3 wavelengths)	9 FBGs (9 wavelengths)
Narrowband Source	Broadband Source
5 Photodiodes	Optical Spectrum Analyser
4 2x2 couplers	1 2x2 couplers4
Pre-Amplifier	Stable Temperature Reference
PC & DAQ	PC & GPIB

Table 5.2: Equipment requirements for FBG based DTS: The equipment cost is significantly less for the OGSN system since it has no requirement for spectral measurement or a dedicated temperature reference. Additionally the Bragg wavelength requirement has been proven achievable by mechanical strain of identical gratings, thus eliminating the cost of custom device manufacture.

5.4 Discussion and Conclusions

It can be seen that Overlapping Gratings Sensor Network has great potential as a distributed sensor. Used in combination with a system such as a Distributive Tactile Sensing surface, it was found to achieve significant improvements over our previous FBG based system interrogated using a high resolution optical spectrum analyser [101].

The primary benefit that this method has over the previous study is one of implementation cost. If we compare the two against each other (Table 5.2) we can see the dramatic difference in implementation cost. The only component of significant cost is the source, however this has potential to be replaced by a multimode laser with suitable spectra. In addition to this the PC and data acquisition could be replaced by discrete components in a commercial design.

Long term stability has been seen to be a problem, with the measurement drift noise preventing successful neural network design. Future work would be required to characterise this further and gain insight into stable long term operation. In particular studies within a controlled temperature environment may help identify problem areas.

Ultimately the proof of principle work contained in this chapter displays great promise for the technique. Within a tactile sensing application the Overlapping Gratings Sensor

Network demonstrates an accurate low cost solution for distributed fibre optic sensing. However more understanding of the system and its noise rejection capabilities are required for long term usage.

Chapter 6

Overlapping Gratings Sensor Network

Chapter 5 introduced a distributed FBG sensing network we named an Overlapping Gratings Sensor Network. This topology evolved out of the edge-filtering interrogation technique introduced by Melle et al. [3], adding multiple filter paths to create a complex response relative to the distributive measurement across all sensors.

The OGSN is specifically designed to operate in tandem with a distributive measurement system such as the distributive tactile sensing surface introduced by Ellis et al. [98]. These systems have limited degrees of freedom and as such restrict the response of the OGSN such that it can be modelled and interpreted.

In addition to clear benefits in terms of implementation cost and potential operation speed, we have shown potential for self-referencing. Edge filter techniques are particularly susceptible to environmental influence and require dedicated references and stabilisation. The OGSN architecture is designed such that factors such as source fluctuation and temperature drift have limited effect upon the resolved measurement.

In this chapter we simplify the system design to investigate the key characteristics and capabilities of measurement systems that employ an OGSN. We employ simulation techniques to evaluate the system and identify behavioural aspects of OGSNs before comparing these results against a practical implementation of the same system.

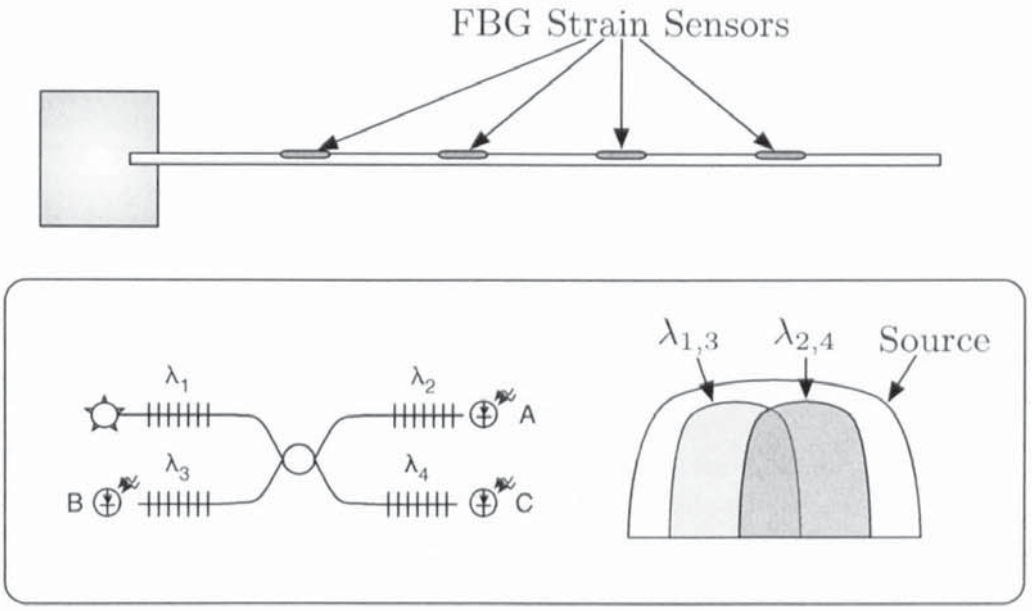

Figure 6.1: 1D tactile sensing system based on a cantilever beam, utilising a single coupler Overlapping Gratings Sensor Network (OGSN)

6.1 System Design

Our proof of principle investigation focused upon the validity and potential of the OGSN measurement technique. However the size and complexity of both mechanical and optical systems limit analysis beyond this point. Full analysis of 2D thin plate tactile sensors is difficult to model successfully [93], especially when convolved with the measurement network response.

In order to investigate the OGSN topology further and characterise its implementation, we must simplify both the OGSN and the measurement system to a model that allows us flexibility to characterise multiple system attributes.

We retain the thin plate tactile sensing method as the mechanical measurement system, however reduce the complexity to a 1D system in a cantilever beam configuration. This is to be measured by a four sensor OGSN, measuring the surface strain of the beam (Fig. 6.1) in order to identify the position of a single point load.

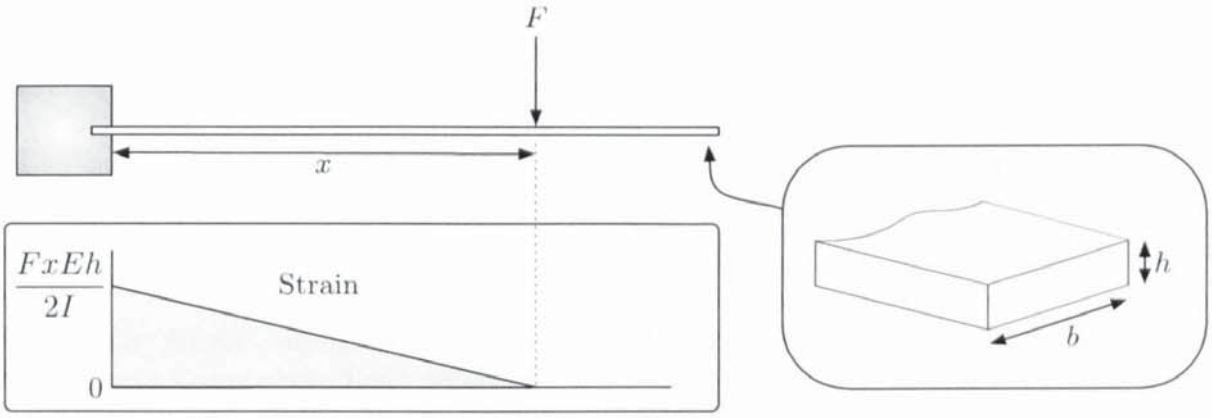

Figure 6.2: Strain distribution across a cantilever beam for a single point load: For a homogenous beam strain increases linearly from the point of contact towards the fixed end at a rate determined by the load strength, the beam's cross-sectional dimensions, and the beam's material properties

This combination allows freedom to investigate the approximation of the underlying measurement transfer function specifically allowing us to to investigate the impact of source fluctuation, training data, noise, and system stability.

Tactile System Design

A cantilever beam (Fig. 6.2) is a classical mechanical system. The strain at a given point on the beam can be modelled as [103]:

$$\epsilon_x = \frac{ME\frac{h}{2}}{I} \tag{6.1}$$

where M is the moment with respect to position, E is the Young's modulus of the beam material, and I is the moment of inertia of the structure which for a rectangular cross-section of width b and thickness h can be given as:

$$I = \frac{bh^3}{12} \tag{6.2}$$

Since only one end of the beam is fixed, there is only moment between the force and the fixed end. Therefore we can identify that the maximum strain is at the fixed point $(= \frac{FxE\frac{h}{2}}{I})$, and this decreases linearly to zero at the point of contact.

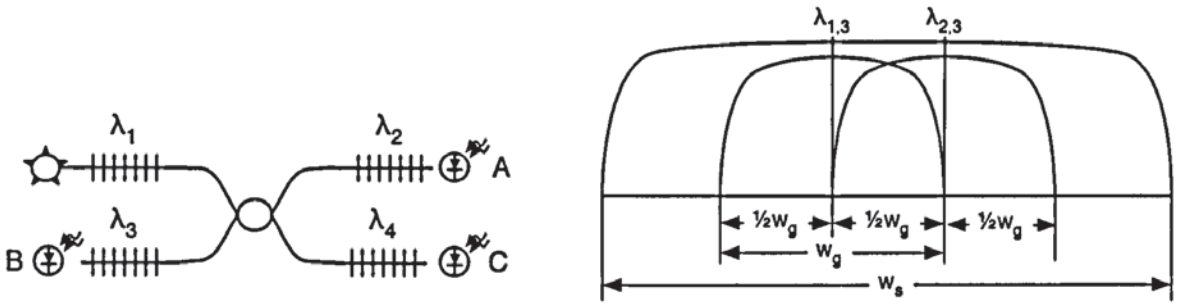

(a) Network (b) Spectra

Figure 6.3: Single coupler OGSN: A fully populated single coupler OGSN has four FBG sensors and three photodiode receivers, with a single interaction zone between the left hand sensors (λ_1 and λ_3), and the right hand sensors (λ_2 and λ_4)

Minimal OGSN design

A fully populated single coupler OGSN has four FBG sensors and three photodiode receivers (Fig. 6.3). The light levels at each of the receivers can be given by:[1][2]

$$P_A = \int \frac{S}{2}(1-R_1)(1-R_2) + \frac{S}{8}(1-R_1)(1-R_2)R_3R_4 \quad d\lambda \tag{6.3}$$

$$P_B = \int \frac{S}{4}(1-R_1)R_2(1-R_3) + \frac{S}{4}(1-R_1)(1-R_3)R_4 \quad d\lambda \tag{6.4}$$

$$P_C = \int \frac{S}{2}(1-R_1)(1-R_4) + \frac{S}{8}(1-R_1)R_2R_3(1-R_4) \quad d\lambda \tag{6.5}$$

where R_n represents the reflection spectrum of the nth grating, and S is the source spectrum.

Neural Network Design

Function approximation with neural networks is key to this distributive architecture. Without some level of machine learning it would not be possible to accurately identify

[1] this assumes the transmission spectrum is the exact inverse of the reflection spectrum

[2] Highly attenuated paths such as $P_A = \int \cdots + \frac{S}{8}(1-R_1)R_2(1-R_2)R_3 \quad d\lambda$ are omitted for clarity, and do not exist for 100% reflective gratings with 'top-hat' profiles

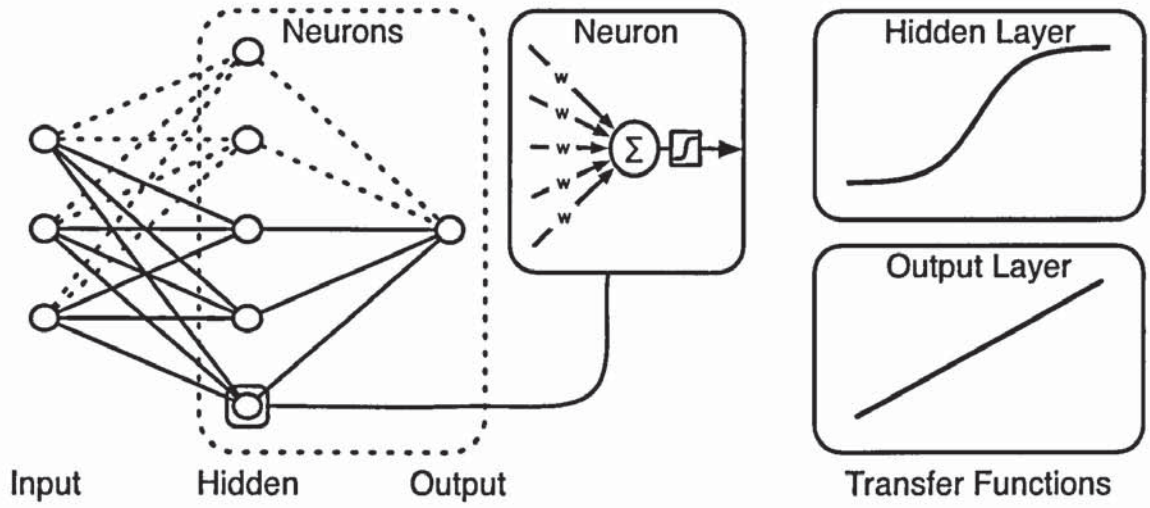

Figure 6.4: OGSN neural network processing architecture: The network used was based on the Multilayer Perceptron (MLP) model, with a single layer of hidden nodes utilising sigmoidal activation functions feeding linear output nodes. Network complexity was controllable be varying the number of hidden nodes.

the measurement transfer function of a practical system because manufacturing tolerances both with the optical and physical system would skew any generalisation of the architecture.

In the preceding chapter we used a Multilayer Perceptron (MLP) neural network architecture to approximate the measurement function. The optimal architecture was decided by increasing the network complexity until the error in a secondary and independent data set was minimised. Since it has been demonstrated that a single hidden layer MLP is capable of regression to any arbitrary function [66], this complexity is increased or decreased by adding or removing hidden nodes respectively.

Here we shall retain the MLP architecture (Fig. 6.4), however we shall incorporate some key differences. The linear transfer functions for the neurons in the hidden layer have been replaced by *tansig* functions, equivalent to the hyperbolic tangent of the input. The use of sigmoidal functions in the hidden layer(s) improves the statistical training process, and the tanh transfer function is known to increase training speed [66].

We also change the training method. In place of the scaled conjugate gradient descent

method, we shall use the Bayesian weight training method introduced by MacKay [65], and described in Chapter 3. This method is proven to provide the optimal generalised network for the function regression of a set of data, and significantly it has been implemented within the Mathworks Matlab Neural Network Toolbox (Version 5.0.1), which shall be used for all network modelling in this section.

6.2 System Evaluation

The fundamental measurement of this system's performance is the accuracy at which we can resolve the position of an applied load. This can be primarily attributed to that of the neural network, either in terms of training ability, or functional stability. Within this however there are certain key factors which should be addressed.

Sensor Position Outputs from the OGSN are a composite measurement of more than one sensor. It is highly probable that the positioning of the sensors relative to each other has some effect upon system performance.

Training Data Spread The use of Bayesian regression in the learning process assigns heavier weighting on sparse data. This may potentially lead to overfitting of sparsely sampled systems and as such it is therefore important to understand the minimal sampling level required to achieve correct approximation.

Noise Susceptibility Noise can influence the system performance in multiple ways. Whilst a degree of training set noise is known to be beneficial with respect to noise suppression [71], there are several noise sources that can influence the measurement system.

Source Fluctuation The performance of source fluctuation is critical to the system integrity and must be characterised and proven.

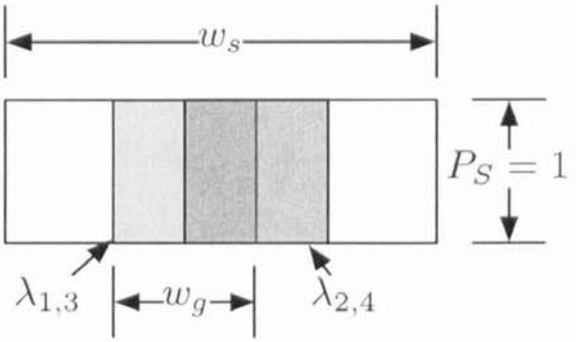

Figure 6.5: OGSN spectra model: The single coupler spectral model can be simplified by using gratings which reflect 100% of the light, with a rectangular footprint, and a source with no ripple that covers the entire sensing range

Signal Level Different weights change the underlying measurement function. This changes both the function shape and signal to noise ratio.

To investigate these attributes we evaluate the system in two stages. Firstly we use a simulation model to examine the limits of operation, and secondly we use a practical implementation to verify these findings.

Simulative Evaluation

Model

The primary mode of operation for an OGSN is for the wavelength shift to be limited to the width of the overlap between gratings. For maximum range this is deemed to be half the grating width w_g for unipolar operation, or $0.25w_g$ for bipolar use. Whilst conceivable, operation outside this range is highly dependent upon the relative shift of all the gratings since gratings must overlap.

For the purpose of simulation we consider the source is of unit amplitude ($P_S = 1$) with a width w_s equal to $3w_g$, centred on the grating spectra (Fig. 6.5). This source spectrum

is rectangular in shape, as is each grating. Using this nomenclature we can consider the power at each receiver in terms of w_g

Therefore the optical model can be given by:

$$P_A = \frac{P_S}{2}\left[(\delta\lambda_1 - \delta\lambda_2) + Z\right] + \mathrm{NF} \tag{6.6}$$

$$P_B = \frac{P_S}{4}\left[(\delta\lambda_2 - \zeta) + (\delta\lambda_4 - \zeta) + w_g\right] + \mathrm{NF} \tag{6.7}$$

$$P_C = \frac{P_S}{2}\left[(\delta\lambda_1 - \delta\lambda_4) + Z\right] + \mathrm{NF} \tag{6.8}$$

where

$$\zeta = \begin{cases} \delta\lambda_1 & \text{if } \delta\lambda_1 > \delta\lambda_3 \\ \delta\lambda_3 & \text{if } \delta\lambda_3 > \delta\lambda_1 \end{cases} \tag{6.9}$$

$\delta\lambda_n$ represents the measurement of the respective grating, and Z is the zero-strain leakage from the light not reflected by the gratings given as:

$$Z = w_s - 1.5w_g \tag{6.10}$$

The system noise figure (NF) represents the cumulative system noise. It is Gaussian distributed and measured relative to the source strength, allowing consideration of noise susceptibility independently of the source level.

This OGSN is measuring the surface strain of a beam top shown in Figure 6.6. The position of the load is measured in units relative to the spacing of the sensors, which are spaced equidistantly along the beam. Since we know that strain increases linearly between the point of contact and the fixed end (Fig. 6.2), no measurement is made with the load positioned 'before' FBG_A. Additionally we can see there is no differential change between sensors for load positions 'beyond' FBG_D, and therefore we do not evaluate for positions between the sensor and the free end.

We consider four different grating configurations for evaluation, given in Table 6.1. The maximum grating shift can be seen to be between FBG_1 and FBG_4, and since the system

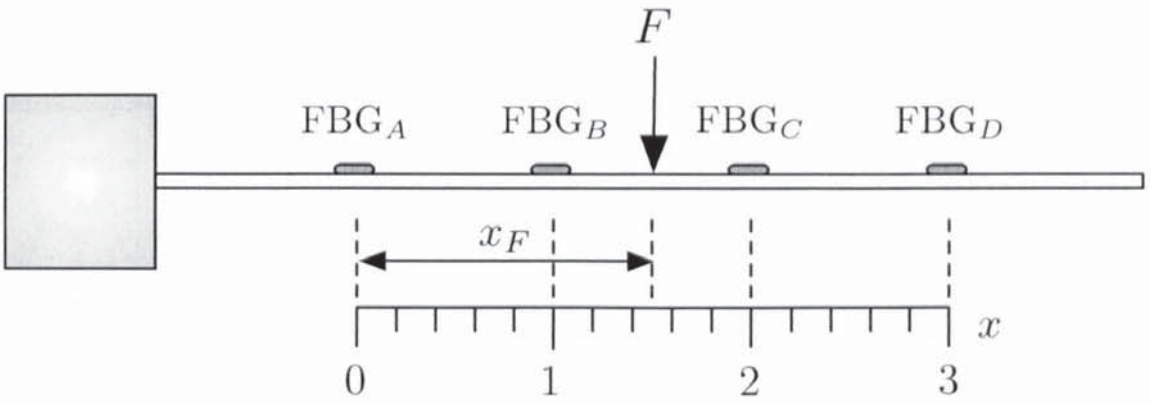

Figure 6.6: Evaluation model for a cantilever beam: A load F acts at a position x_F on the beam. The sensor are evenly spaced along the beam, measuring the topmost surface strain. The evaluation range is confined between sensors A and B, measured in units of sensor spacing distance

Config	FBG$_A$	FBG$_B$	FBG$_C$	FBG$_D$
A	FBG$_1$	FBG$_2$	FBG$_3$	FBG$_4$
B	FBG$_1$	FBG$_3$	FBG$_2$	FBG$_4$
C	FBG$_4$	FBG$_3$	FBG$_2$	FBG$_1$
D	FBG$_4$	FBG$_2$	FBG$_3$	FBG$_1$

Table 6.1: FBG Sensor Position Configurations

is unipolar in operation the maximum load we can use across the entirety of the beam $F_{\max}$ is $\frac{1}{6}xw_g$.[3]

Inside this range the shift at position x caused by a single point load at x_F can be given by:

$$\delta\lambda = \begin{cases} F(x_F - x) & \text{if } x_F > x \\ 0 & \text{otherwise} \end{cases} \tag{6.11}$$

Using the model given by equations 6.6 through 6.11, we can determine the receiver output for each of the sensor position configurations given in Table 6.1. Figure 6.7 shows the relationship between each of the receiver levels for a load of $F_{\max}$ at different positions along the beam.

[3]units measured relative to the grating width and grating spacing

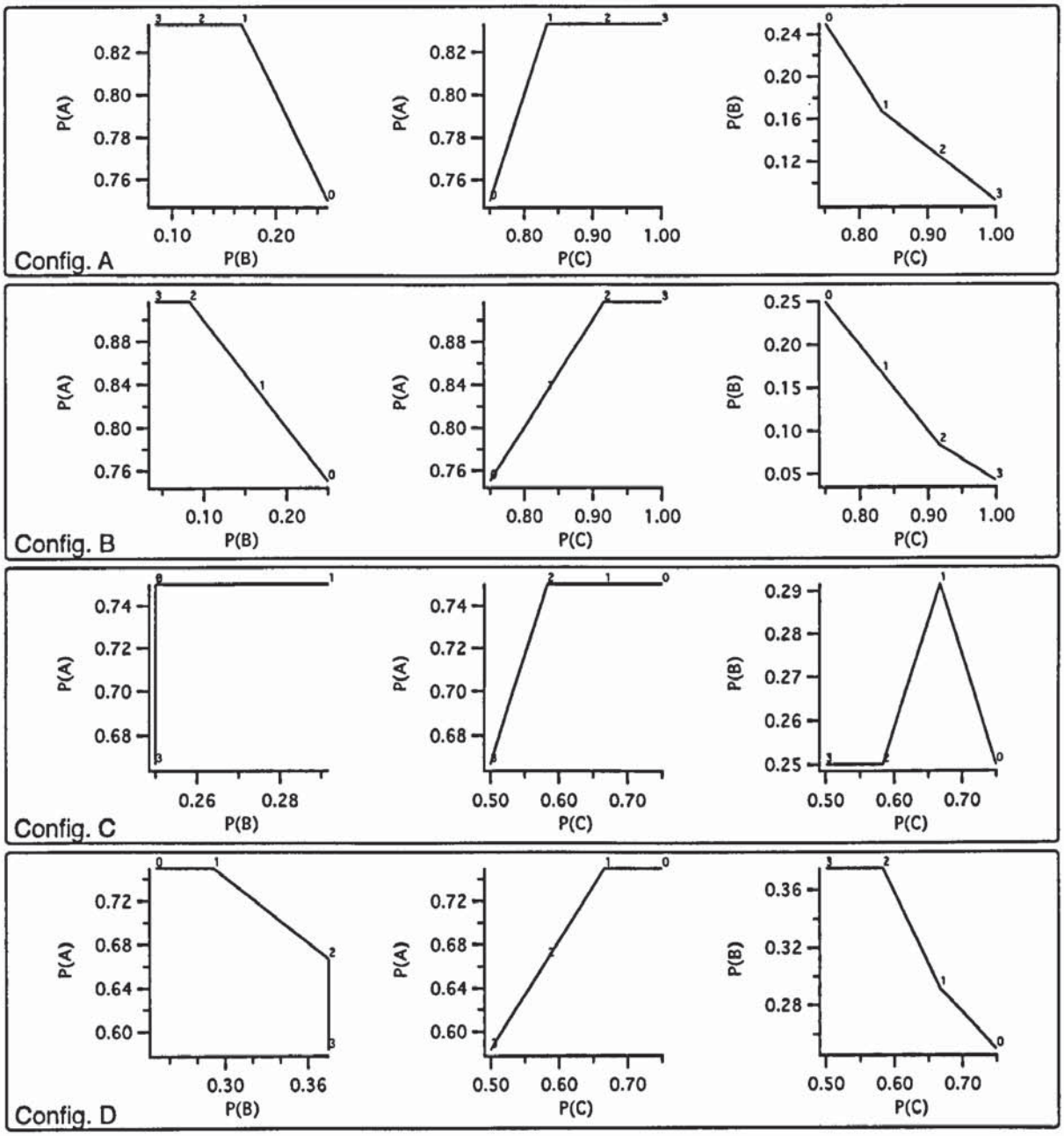

Figure 6.7: Cantilever beam simulation model: Simulated output powers for different load positions (indicated by marker value) calculated at receivers P_A, P_B, P_C, and P_D for sensor configurations A, B, C, and D (top to bottom respectively) as given in Table 6.1. A single point load of $F_{\max}$ $(= \frac{1}{6} x w_g)$ is considered in different positions, and the power at each receiver is calculated using equations 6.6 through 6.11. Of all the configurations, configuration 'B' shows significant promise because of the large level of simultaneous movement on all receivers.

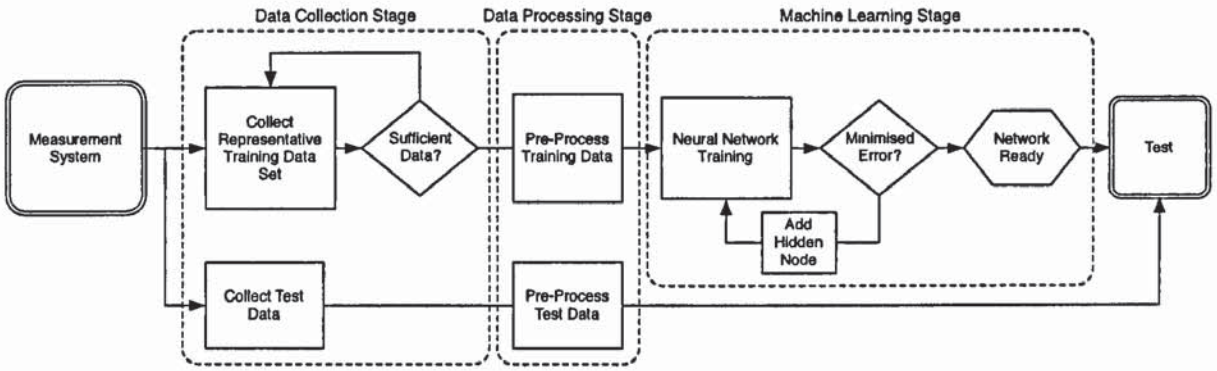

Figure 6.8: Training/sampling process for an OGSN measurement system: Following collection and pre-processing of independent data from the measurement system, the network complexity is iteratively changed to determine the optimal processing architecture

Ultimately we wish to train a neural network to resolve position from an input condition given by the combination of receiver levels, and therefore we can immediately see potential difficulties with configuration C since the path is complex with little simultaneous movement on all receivers, and it is not well separated between dimensions (receiver levels). In contrast to this configuration B immediately appears attractive since there is a simultaneous change on all three receivers between positions '0' and '2', and change on receivers B and C between positions '2' and '3'. This is clearly well separated between dimensions, with a smooth continuos path that has a high potential for noise rejection.

Training Data Evaluation

Ultimately an OGSN is trained and calibrated in-situ. Whilst it may be possible to know some characteristics in advance, it is necessary to collect data from the system. The constitution of this data is of great significance since we wish to have optimal system performance with the minimum amount of data.

Figure 6.8 shows the general sampling and training process for OGSN based systems. Within this process we only truly have control over the data collection and processing stages. The mechanical and optical system is fixed, with specific transfer function and a

specific noise level. The machine learning stage is automated beyond the initial choice of learning algorithm and network type. However we have two controllable inputs to the data collection stage; sampling density and sample set size, and we are also able to process this collected data such that any features within the data set are scaled appropriately for the machine learning stage. Typically this scaling is a simple normalisation process ensuring that the data range between inputs are similar, however for more complex data sets requiring specific feature extraction other techniques may be considered [64].

We can consider the impact of sampling attributes by looking at the performance with respect to positional accuracy at different system noise levels. It is not possible to eliminate all noise sources from the system, and in particular slow drift of both mechanical and optical measurement is of significant concern. Therefore we must consider the operation and training inside a noisy environment, and the effect that both sample rate with respect to the sensor spacing and training sample set size in terms of repetitions have upon the system uncertainty.

It can be seen from Figure 6.9 that an increase in sample set size does show improvement with more data. However the effectiveness of extra data decreases as the sample set gets larger. We can also see there to be a marginal accuracy improvement for sensor configurations B and D over configurations A and C.

Sample spacing (Fig. 6.10) plays a more profound role, with overall accuracy improving with increased measurement density. By measuring the error at different positions along the beam over several repetitions we can determine both the mean and the RMS error for that specific location when the training data is sampled at different resolutions. Figure 6.11 shows there to be clear distinctions between the different sensor configurations. Configuration B can be seen to perform well at all samples rates, whereas configurations A and C appear to have systematic accuracy problems evident at low sample rates by

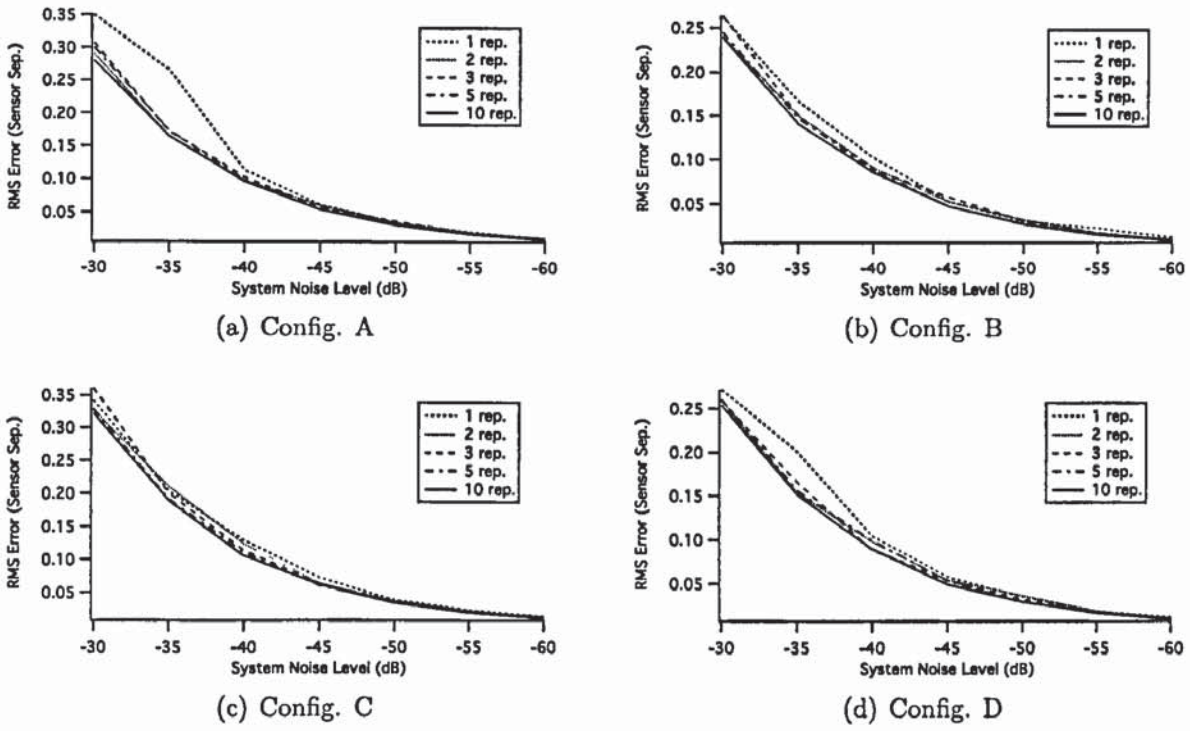

(a) Config. A (b) Config. B

(c) Config. C (d) Config. D

Figure 6.9: Effect of training data set size (repetitions of data sets covering the length of the beam) has upon system accuracy measured by the overall RMS error relative to the sensor spacing (Load $F = F_{\max}$, Sample rate = 5 samples per sensor). Increasing the number of data sets used to train the neural networks whilst keeping the sampling spacing constant improves the system performance (presented in terms of noise rejection capability).

their mean error.

If we consider the results of testing the effect of both sample density and number of sample set repetitions in the training data set, it is clear that configuration B and D perform better and make more efficient use of the training data training data.

Source Fluctuation

Edge-filter interrogation is significantly affected by source power variation. Other edge-filter based methods nominally use a dedicated receiver to monitor the unfiltered light in order to compensate for source fluctuation [3, 59, 58]. The OGSN is specifically designed with source fluctuation compensation integral to operation.

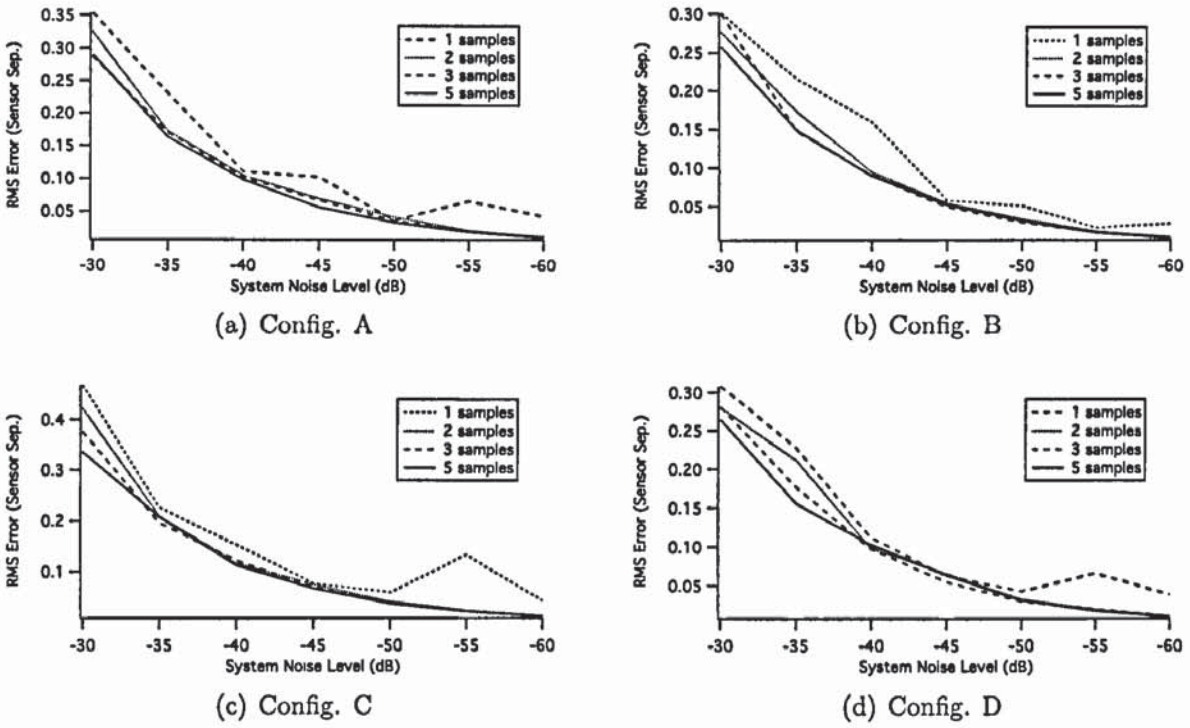

(a) Config. A (b) Config. B

(c) Config. C (d) Config. D

Figure 6.10: Effect that sampling density (samples per sensor spacing) has upon system accuracy measured by the overall RMS error relative to the sensor spacing (Load $F = F_{\max}$, Sample set size = 3). Increasing the number of samples taken between each fibre Bragg grating sensor for the neural network training data improves the system performance (presented in terms of noise rejection capability).

We have seen that performance of the approximation is significantly dependent upon sufficient sampling of the measurement model, and this is likely to extend to the fluctuation compensation performance being dependent upon power level sample distribution. By measuring the error relative to source level and beam position for networks trained with data sets of varying sampling density, both in terms of position and source power level, we are able to determine the effectiveness of each sensor configuration to provide this compensation.

Figure 6.12 shows that the sample distribution does have a significant affect on the complete operation of an OGSN. Evidently each configuration performs differently and it becomes clear that configuration C show particularly poor performance, whereas configuration B displays a clear readiness to train and displays good accuracy at sparse sampling

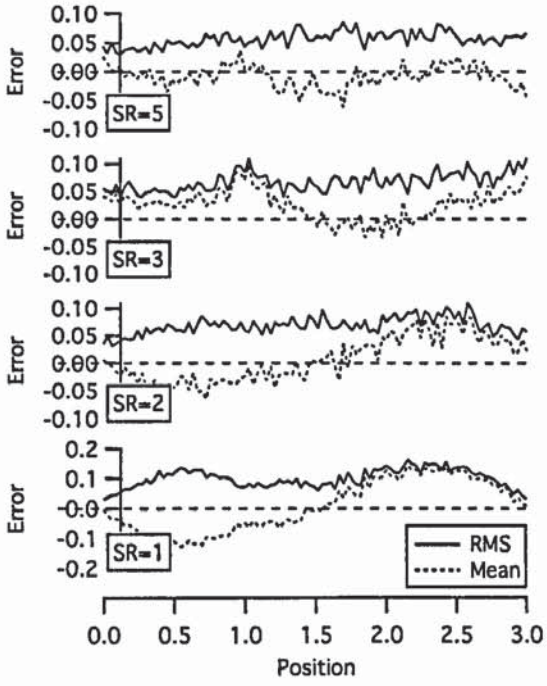

(a) Config. A

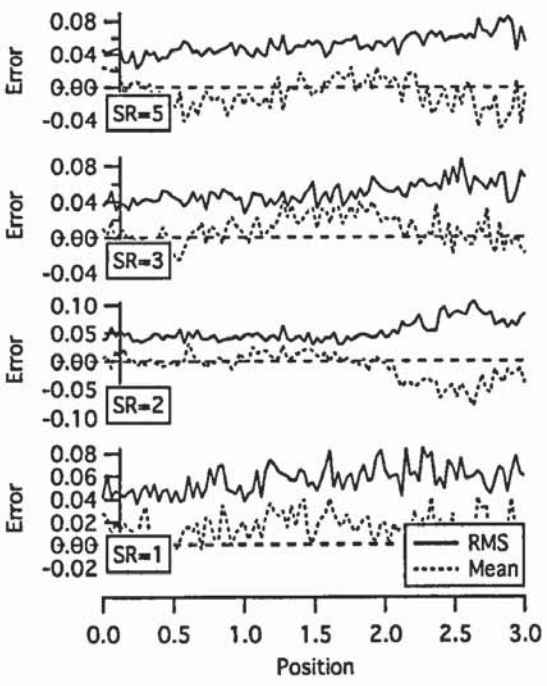

(b) Config. B

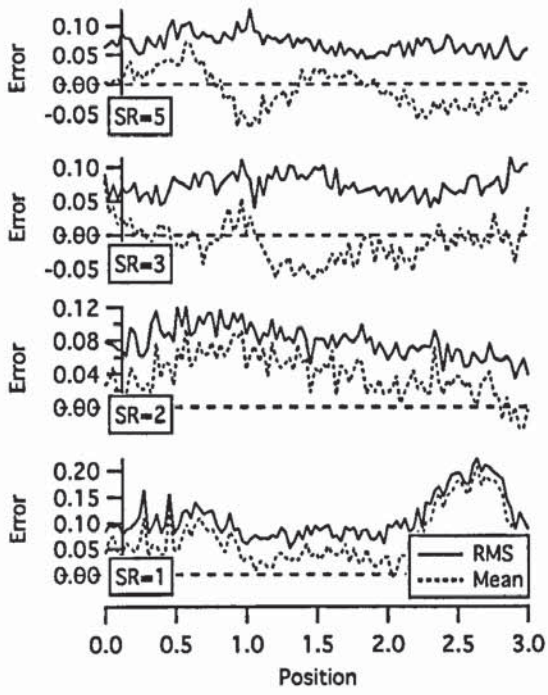

(c) Config. C

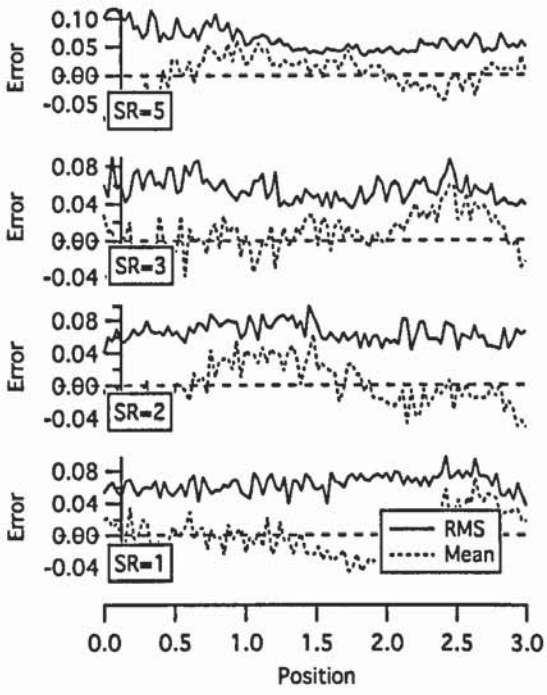

(d) Config. D

Figure 6.11: Effect that sampling density (samples per sensor spacing, denoted as *SR*) has upon the system positional accuracy measured as mean and RMS error (Noise level = -45dB,Load $F = F_{max}$, Sample set size = 3): Increasing the number of samples taken between each fibre Bragg grating sensor for the neural network training data improves the system performance. Configurations A and C appear to have more systematic accuracy problems evident by the mean error at low sample rates.

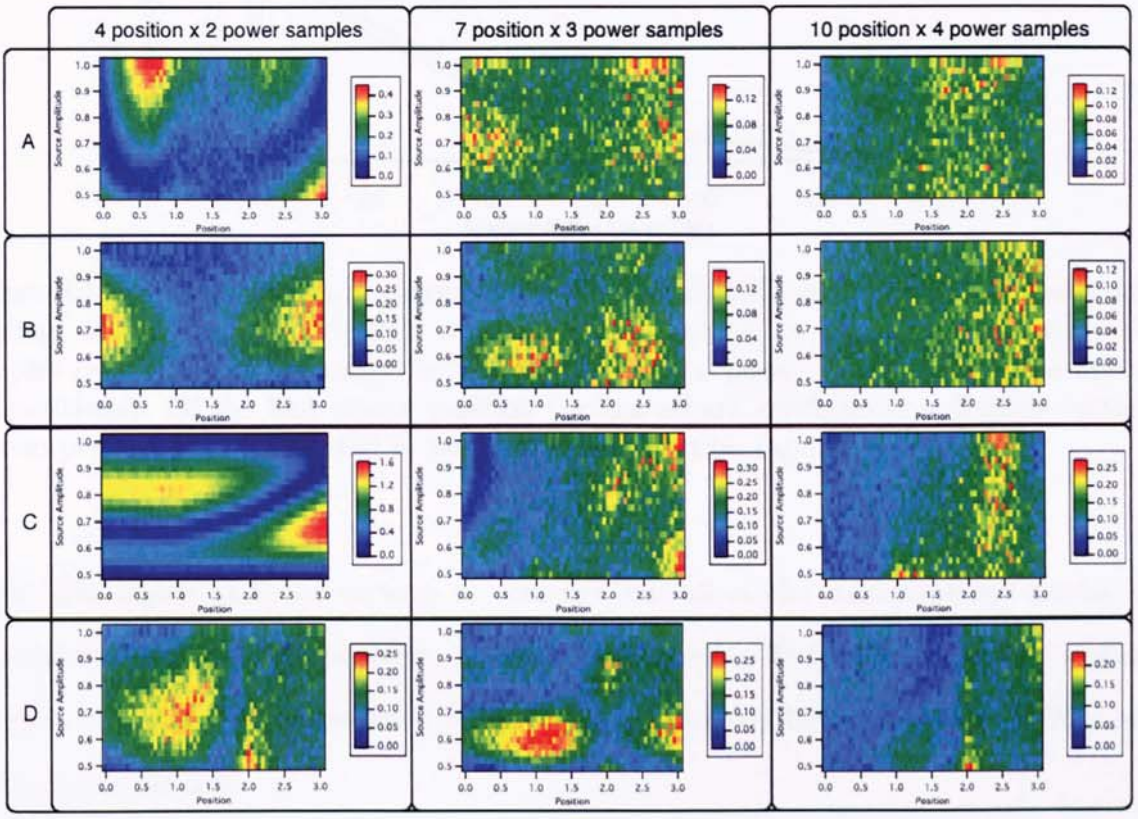

Figure 6.12: Effect that sampling density (increasing left to right, measured by number of samples taken along the beam and the number of samples taken at different powers for those position) has upon the system positional accuracy as an RMS error figure displayed as the colour intensity (In order to highlight patterns within the results, each plot has its own colour scale indicating the RMS error), measured relative to the beam position and source intensity (Noise level = -45dB,Load $F = F_{\max}$, Sample set size = 3): Increasing the number of samples taken between each fibre Bragg grating sensor alongside the number of power levels tested over the full range for the neural network training data improves the system performance. Configuration C performs significantly poorly in comparison with the other three configurations displaying significant systematic accuracy problems at low sample rates, which at higher sample rates becomes increased error as the position increases. Configuration D also displays systematic errors, with a prominent in line with the third grating (position 2). Configurations A and B appear to be less systematic in error, with B being the optimal sensor placement configuration

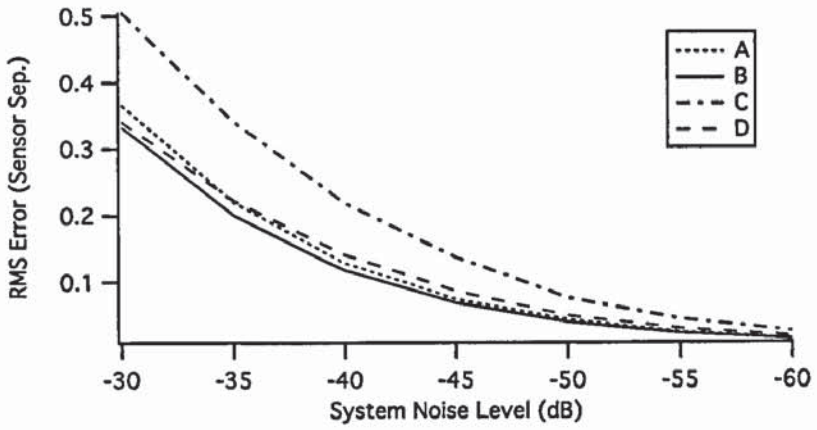

Figure 6.13: System accuracy measured by the overall RMS error relative to the sensor spacing, tested over the 25-100% source power range ($F = F_{\max}$, Sample rate = 16 samples over the position range by 7 samples over the power range, Sample set size = 3 repetitions). Of the four sensor position configurations, configuration B gives optimal system performance (presented in terms of noise rejection capability)

levels. For highly sampled systems we can see that all of the configurations display an uncertainty increase with position, however configuration D begins to display a sharp increase in systematic uncertainty when the load is placed between sensors FBG_C and FBG_D (position 2-3).

Clearly a high sample density can give a greater accuracy over the full operating range, however sensor positioning has a greater impact upon the accuracy and the efficiency of the training data used to train the respective processing neural network.

Simulation Results Discussion

It is clear from these results that the position configuration has a significant effect upon the an OGSN's performance. It dictates the level of system sampling that is required and with sufficient sampling dictates the ultimate system performance (Fig. 6.13). If we consider the measurement model given in Figure 6.7, the increase in systematic behaviour appears to be related to function complexity and optimal accuracy can be found for relationships with simultaneous movement across all inputs (Config. B, positions 0-2).

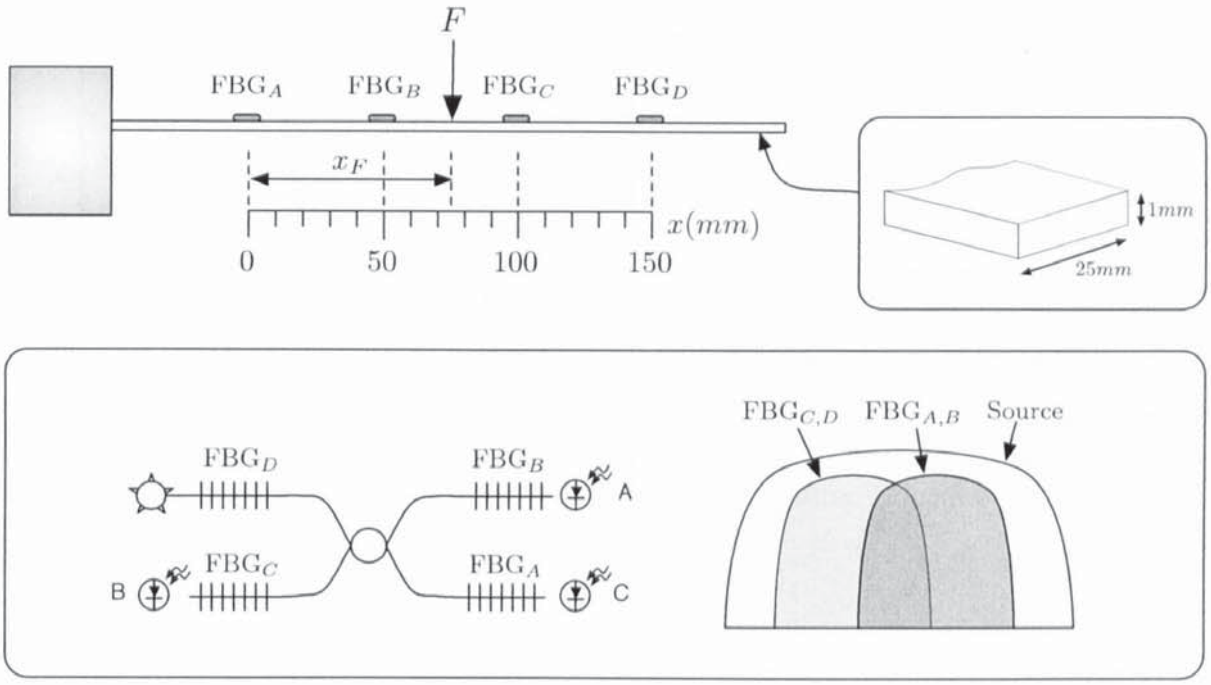

Figure 6.14: Experimental apparatus used for system evaluation: A rule which was fixed at one end was used to mount the 4 sensor gratings, arrange as 'configuration D' from the preceding section

We also can see that the level of sampling required could be found experimentally. We have seen results indicative of an optimisation limit both in terms of sample set size and sampling density, which could be approached iteratively.

We have seen throughout this section that signal level (or noise level as we have provided here) is significant to the operation of an OGSN implementation. In addition to the results contained within this work the author has on numerous occasions attempted to create a system capable identifying the position of any arbitrary sized load using the same trained model. This has not been successful and as such not presented, however it is a definite area for future study.

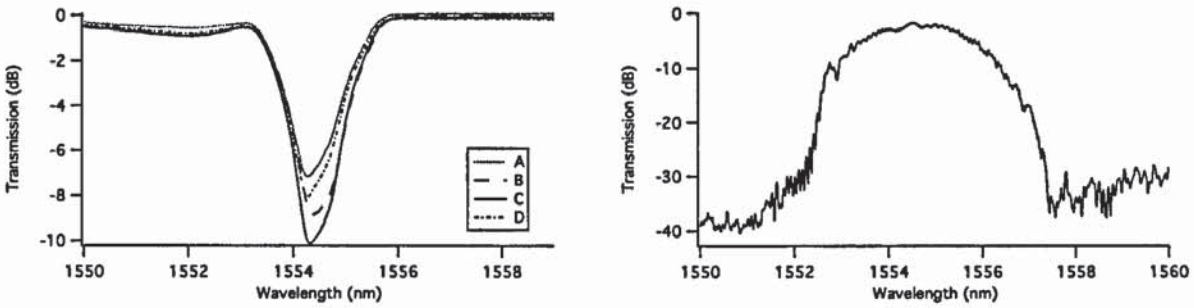

(a) Sensing gratings

(b) Source grating and circulator

Figure 6.15: Grating transmission spectra for the OGSN test system: Four identical chirped fibre Bragg gratings were inscribed for the sensor gratings (Fig. 6.15(a)), whilst a chirped grating and circulator were used to create the source (Fig. 6.15(b))

Experimental Evaluation

Our practical implementation used a 25mm wide, 1mm thick steel rule with a measurement surface of length 150mm (Fig. 6.14). In order to gain both a measurement of potential accuracy and an insight into the prominence of systematic noise the sensors were positioned as simulation configuration D.

Each FBG sensor was inscribed with a length of 10mm at a central wavelength of 1554.5nm (Fig. 6.15(a))[4] and a 1.2nm chirp, using the dithered pulse phasemask method to create the chirp. Following annealing at 90°C for over 48 hours to ensure stability, they had approximates strengths of 9dB.

A further chirped grating was inscribed to be used with a broadband source and circulator to create a narrowband source (Fig. 6.15(b)). This grating had a length of 30mm with an inscribed central wavelength of 1554.5nm and a 7nm chirp. Following the same 90°C annealling process it had a strength of 30dB and was fixed to a large metal mass such that the central wavelength was 1555nm. A current stabilised Erbium Doped Fibre Amplifier (EDFA) was used as the broadband source.

[4]The zero-strain Bragg wavelength tuning was to be performed by fixing the grating to the surface under strain in order to mitigate wavelength shift by inscription method or annealling

The sensors were glued into position on the top surface of the rule. Each was fixed under strain such that they were approximately centred upon the source using a measurement overlap of 0.5nm.

The photodiodes were low cost free space devices simply glued into position. Since high speed operation was not an objective, each photodiode was connected in a zero-bias configuration to custom low noise pre-amplifier circuits in order to reduce dark current. The pre-amplifiers were in turn measured by a National Instruments NI USB-9201 Data Acquisition card (DAQ) connected to a Labview PC terminal.

System Characterisation

To characterise the measurement transfer function we measured the positional system response for an applied load over a period of 6 days. During this period we measured the voltage as we moved a 2.5N load along the sensing surface with the source delivering a constant 49.7μW off the source grating.

We can see from Figure 6.16 that the path differs from the simulation model between sensors FBG_C and FBG_D (100-150mm) on both receiver B and C, and that there is a low signal to noise ratio on all three receivers. Receiver A appears to fall slightly between 140 and 150mm, receiver B decreases considerably between 100 and 150mm, and receiver C decreases between 120 and 150mm. The likely cause of output A falling between 140 and 150mm is from a positioning error in the fixation of sensor FBG_D, whereas the deviation of output B and C are likely to be caused by the lack of ideal 'top-hat' shaped grating spectra and the amount of overlap between grating filter pairs.

There is however a clear measurement function without any overlap in measured noise, and this has distinct potential for approximation. We can also use this data to investigate the learning characteristics of the system. Specifically we are interested in the level of sampling required to approximate the measurement function.

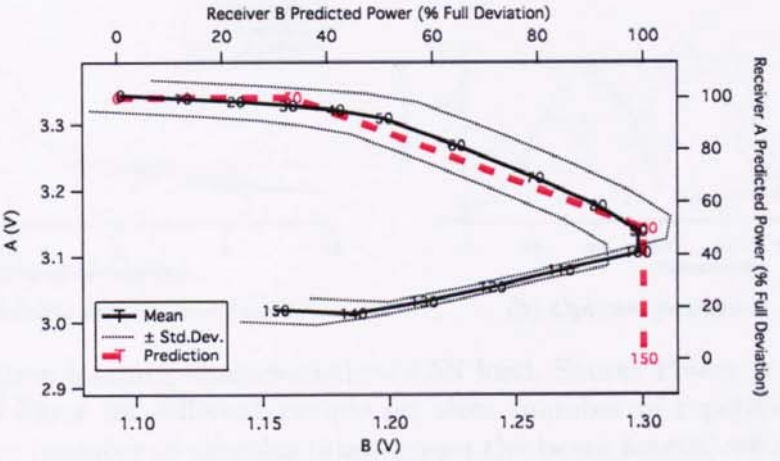

(a) Receivers A vs B

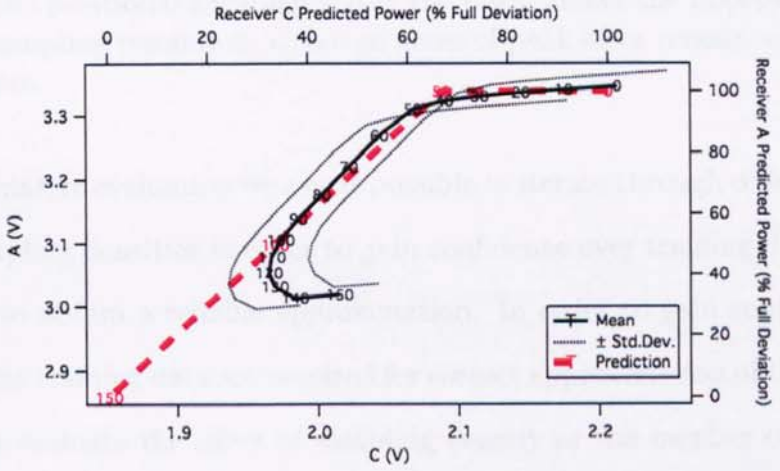

(b) Receivers A vs C

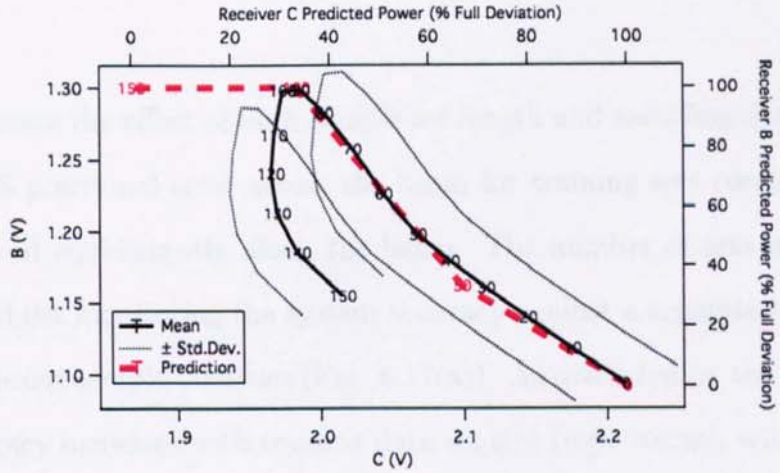

(c) Receivers B vs C

Figure 6.16: Experimental system measurement characteristics: Measured output powers for different positions of a 2.5N load (indicated by marker value in millimetre), as measured by receivers A, B, C, and D (Source Power = 49.7μW): Measurements for the practical system can be seen to loosely fit the predicted response from Figure 6.7 (top and right axis), deviating primarily at positions greater than 100mm, for receivers B and C.

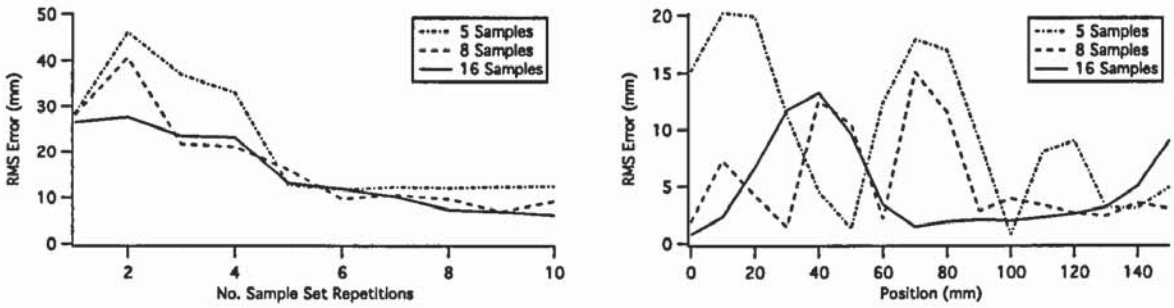

(a) Effect of sample set size and density

(b) Optimal positional accuracy

Figure 6.17: System learning characteristics (2.5N load, Source Power = 49.7μW): Measuring the RMS Error for different sample set sizes (number of repetitions in the data set) and densities (number of samples taken across the beam length) we can see there to be optimal sample set sizes for each sampling density (Fig. 6.17(a)). Using this optimal sample set size the positional accuracy across the beam shows the improvement given by the increase in sampling resolution, although areas of peak error remain at approximately 40mm and 150mm.

From our simulative evaluation we saw it possible to iterate through different sample set lengths and sampling densities in order to gain confidence over training data distribution and the ability to obtain a reliable approximation. In order to gain confidence over the distribution of the training data set required for correct approximation of the experimental system we must evaluate the effect of sampling density or the number of samples taken across the beam length, and also the number of these repetitions required for the training data set.

Figure 6.17 shows the effect of both sample set length and sampling density, measuring the overall RMS positional error across the beam for training sets comprising 5, 8, and 16 samples spaced equidistantly along the beam. The number of sets used for training was increased whilst monitoring the system accuracy against a separate independent test data set for different sample densities (Fig. 6.17(a)). As predicted by the simulations, the positional accuracy increases with training data set size (repetitions), with each sampling density approaching an optimal size for set lengths greater than 5 repetitions.

When we examine the positional accuracy along the beam for each sampling density using the optimal training data set lengths found in Figure 6.17(a) (Fig. 6.17(b)), we

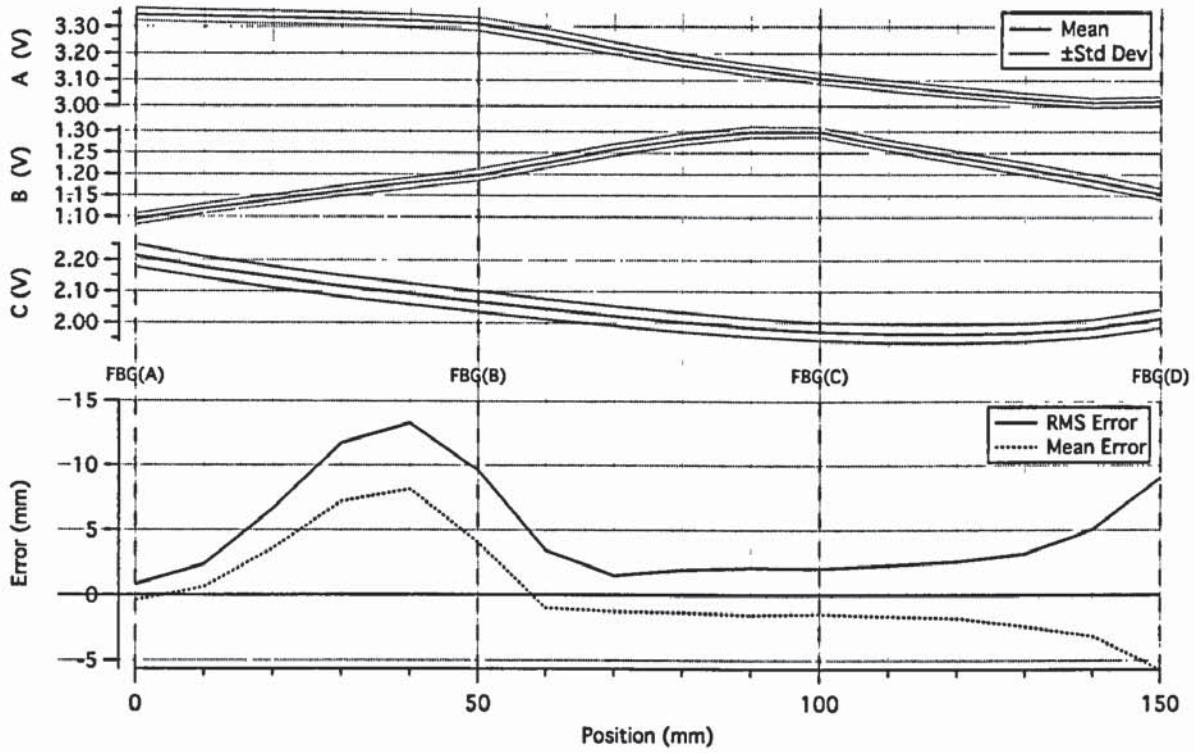

Figure 6.18: System accuracy characteristics (Training set = 10 sets of 16 samples, Optimal network has 5 hidden nodes): Aligning the measured voltage (top three traces) with the positional error we find a correlation between positions of low gradient of A and high levels of uncertainty.

find that a high sampling density of 16 positions (every 10mm) is required to achieve a smooth, well resolved neural network. In addition, as predicted by the simulations, this positional accuracy uncertainty appears to contain systematic uncertainty for a fully optimised network.

When we look at the the accuracy characteristics in full, aligned with the OGSN response (Fig. 6.18), we see an apparent reliance upon receiver A for optimal accuracy. We can see that positions of low gradient of A coupled with the high level of measurement uncertainty on receiver C has a distinct effect upon the accuracy in specific positions. From these results we find a specific region between 70mm and 130mm where measurement is optimal which loosely matches the results seen in Figure 6.11(d) for the same sample rate.

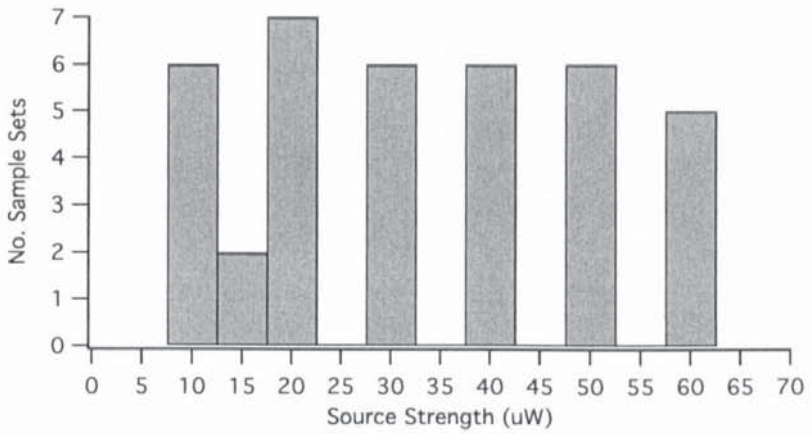

Figure 6.19: Training set distribution for full system testing

Measurement Stability

When we consider long term measurement stability we must consider the two primary factors; immunity to source fluctuation, and noise rejection. Source fluctuation is straightforward to instigate in the system, as we can control the EDFA current. Because drift and creep noise sources can be slow, sporadic, and difficult to quantify it is necessary to manipulate the signal to noise ratio by using different weights. This in addition to source variation enables us to increase the noise figure and gain an insight into operational limits.

We collated a training data set from measurements made at different points in the day, at different source strength, with different loads, over a full period of 19 days. A representative selection of data measured at different power levels (Fig. 6.19) was separated into training sets for 1N, 2N, 3N, and 4N loads. The test data set contained samples measured at source levels of 11.6, 21.0, 29.9, 40.7, and 50.5μW.

Figure 6.20(a) shows how the system behaves at different signal levels, which follows a similar profile to that of Figure 6.13. Looking at this uncertainty with respect to position (Fig. 6.20(b)) we can see that for low signal levels the accuracy is dominated by the region of low uncertainty identified in Figure 6.18 with a minimum at approximately 100mm. As the signal level increases the network is able to generalise and cover more of the beam,

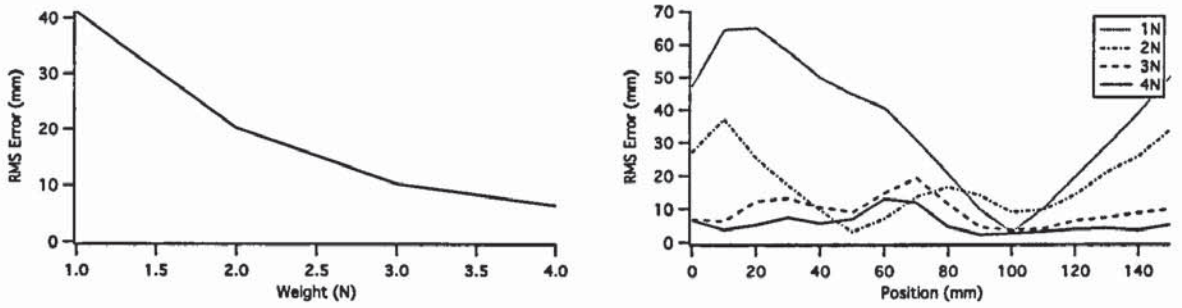

(a) Effect of load (signal strength) upon system performance

(b) Positional accuracy for different load sizes

Figure 6.20: System performance over the source range 11.6 - 50.5μW for different size loads: As the load or signal level is increased, the accuracy increases accordingly

ultimately identifying a region of inaccuracy to a localised area near 65mm.

If we expand the results from Figure 6.20(b) further to illustrate the effect of source level for each of the different loads (Fig. 6.21), we can see a similarity with the simulations shown in Figure 6.12 which showed the effect of sampling density upon system accuracy. Low signal testing has the same uncertainty signature as the simulations performed with low density training data, whereas our heavier load testing matches the results from the medium data density tests.

It is very clear from these results that signal level (size of load) has an effect upon system accuracy and the ability to train a correctly generalised processing network. However it is more significant that regions of uncertainty found by system simulation correlate to those found in the practical measurement system, highlighting the benefit of thorough system evaluation prior to manufacture.

With this in mind we performed long term analysis with a static load of 2.5N positioned at FBG_C (100mm), which was found to be a specific position of uncertainty in our simulations. The results shown in Figure 6.22 highlight this position as having greater susceptibility to noise compared to the same load in a different position, which we had previously shown in Figure 6.18 to have a similar positional error for the same 2.5N load.

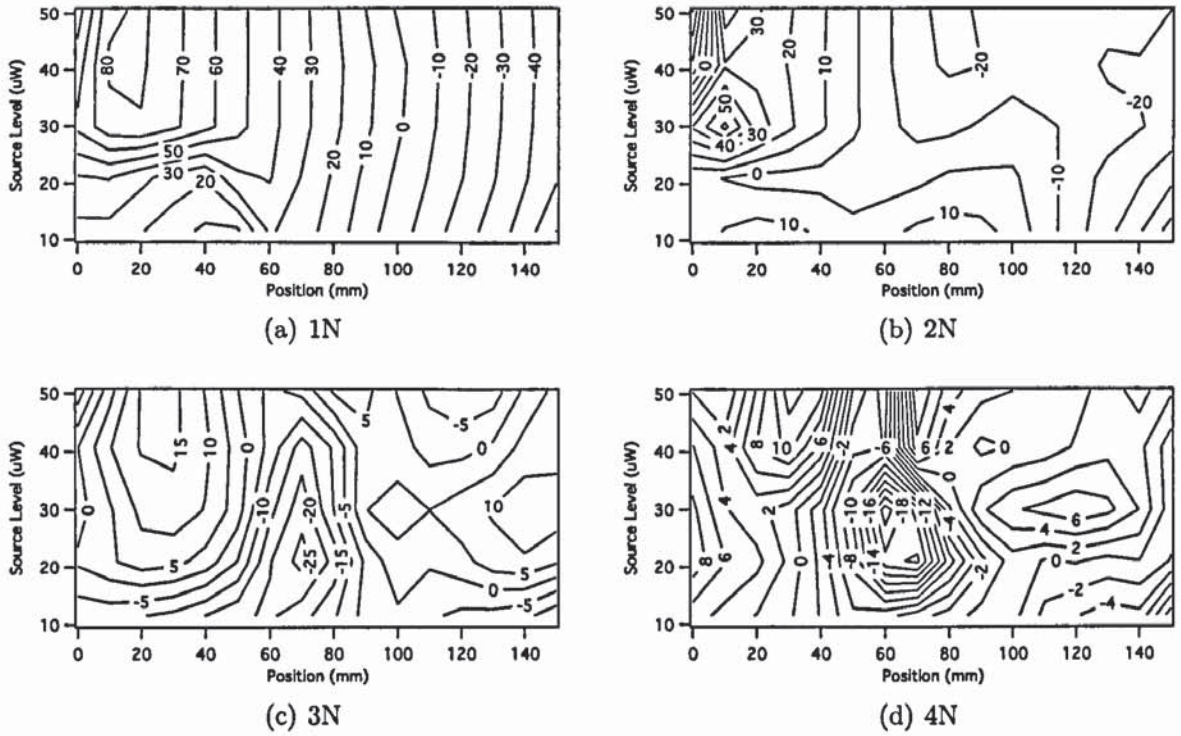

(a) 1N (b) 2N

(c) 3N (d) 4N

Figure 6.21: Contour map illustrating the RMS positional error (mm) measured relative to the beam position and the source level over the source range 11.6 - 50.5μW for different size loads: As previously seen in Figure 6.12 there are definite signatures for the accuracy measured relative to the source level and beam position. As a larger signal is used a prominent feature develops at a position of approximately 70mm for a source level of approximately 25μW.

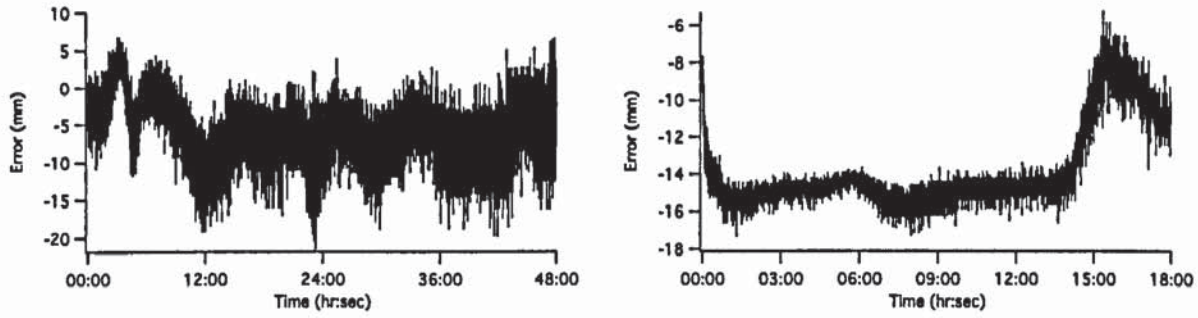

(a) 48hour test with a static load at 100mm (b) 18hour test with a static load at 130mm

Figure 6.22: Long term stability measurement with a static 2.5N load: Despite the presence of drift on the 18 hour test at a load position of 130mm, greater measurement noise can be seen with the load positioned at 100mm

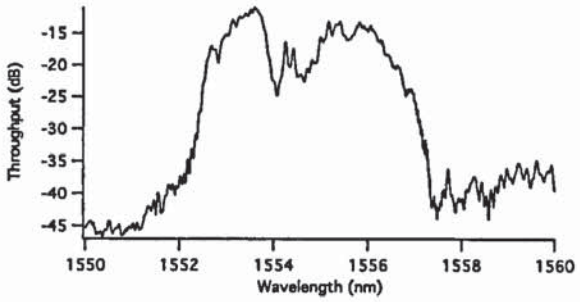

(a) Output A

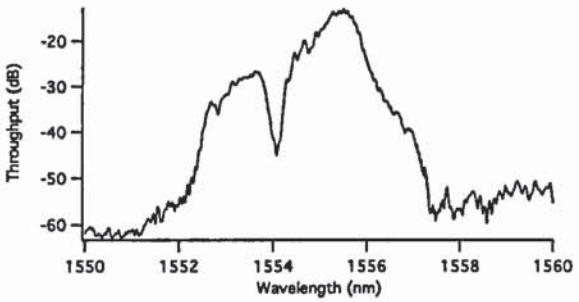

(b) Output B

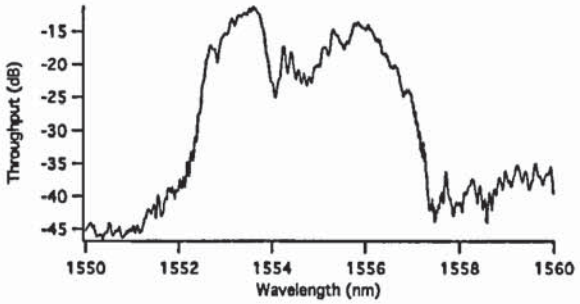

(c) Output C

Figure 6.23: OGSN system and source grating spectra measured with a tuneable laser: Measuring the spectra seen at each receiver we can see the deviation from the ideal 'top-hat' chirped fibre Bragg gratings used for system design and simulation

These long term tests do present issues with drift. Figure 6.22(b) displays an overnight measurement displaying a clear indication of temperature susceptibility, correlating with the drop in ambient temperature expected in such test conditions. Since ideal rectangular shaped spectra should not exhibit such dramatic movement we attribute this to the non-ideal shapes of both source and sensor gratings shapes caused by the self apodisation effect from the inscription beam [29, 31]. This can been seen in Figure 6.23 where the spectrum at each output is measured with no system load by a tuneable laser scanning system (EXFO IQ-12004) with a 5pm step resolution. We also notice that the spectrum measured at receiver B contains light outside the range of λ_B or λ_D which is indicative of back-reflection from one or both of the other two receivers.

6.3 Discussion and Conclusions

The OGSN method continues to display tremendous promise as a low cost optical fibre sensor measurement system. Whilst the 1D tactile sensor presented in this chapter was not designed for a specific application, it clearly demonstrates good measurement accuracy for very few basic components, and is able to measure with low short term uncertainty to dimensions far smaller than that of the sensor separation.

It is however necessary to pay significant attention to the quality of these components for optimal system performance. This is particularly important with respect to grating manufacture. It has been seen that long term stability would be dramatically improved if gratings with ideal 'top-hat' responses were used in place of those used in this test. Commercial implementation could provide this requirement using a single chirped phasemask covering the full range.

One factor that has arisen from this work is the importance of sensor placement in determining system integrity. The motion of the measurement transfer function with respect to measurand can be seen to determine optimal accuracy, with transfer functions of low complexity and simultaneous output movement proving the most successful.

Through the judicial use of a sensor positioning configuration that displayed specific systematic uncertainty signatures with respect to positional accuracy (Config. D, Fig. 6.12), we were able to prove the validity of our simulations by demonstrating the same behaviour in our experimental system. This is significant as it demonstrates the use of a simplified model is useful as a pre-planning tool in neural network applications, and as a result we were able to locate a specific location of increased uncertainty not seen during any other experimental test (Fig. 6.22(a)).

Introducing this training behaviour as a qualitative tool in system design opens up potential for future work in automated design implementations. We have seen that a simplified model exhibits very similar training and accuracy characteristics to a real world

system, despite having a different underlying measurement function. Using this method and monitoring for 'problem areas' indicated by training signatures, we would be able to apply genetic algorithms to determine parameters such as sensor position [104, 105], sampling distribution [106], and potentially the OGSN architecture itself.

Clearly there is a limited dynamic range offered by the measurement system, as the signal is generated by the relative strain between overlapping gratings. Since the signal size has a significant effect upon system accuracy the grating width and position must be optimised for a specific load, so that maximum movement of overlap can be achieved. Again this would be an ideal candidate for optimisation using genetic algorithms [104, 105, 106].

Other additional areas of study could address the issue of different signal levels (load sizes). This could potentially be solved using kernel mode principal component analysis (PCA) [64] utilising a model of the single load measurement function in the pre-processing stage, or through the use of different advanced network topologies containing feedback paths [68]. As well as increasing the system functionality and integrity, because of the additional training data available to the network this is likely to increase accuracy over the full dynamic range.

It is perhaps dynamic systems that offer the greatest potential for utilisation of this technology. Elliott et al. [107] have demonstrated the potential of DTS as a dynamic system measuring load movement on a surface using signal processing. However it the area of structural health monitoring (SHM) [108, 109] that could see the most benefit from OGSN systems. Because of the inherent scalability to the network, coupled its real-time capabilities this topology has direct relevance to acoustic monitoring of structures for damage and fatigue. As a precursor to large scale implementation the four sensor fibre Bragg grating strain gauge rosette [110] would be easily realisable by a fully populated single coupler OGSN as presented in this Chapter.

In conclusion we have presented techniques for implementing and designing Overlapping

Grating Sensor Network systems, and have found it to have great potential for future designs. The cost of implementation is far reduced from other fibre Bragg grating systems, and given ideal manufacture of sensor and source has the potential to rival most for both accuracy and stability.

Chapter 7

Thesis Summary and Conclusions

The overall objective of this thesis was to develop low cost fibre Bragg grating based sensing systems. We have focused on the use of novel processing techniques to analyse and enhance proven methods and extend them where possible. As a result we have presented two novel systems, both shown to outperform existing methods on a number of attributes.

Low Resolution Spectral Analysis

We first looked at the area of resolution enhancement for fibre Bragg grating interrogation using a low resolution discretely sampled spectrum. Through careful evaluation of two existing processing techniques we were able to propose two enhancements.

The first method was based upon the Least Square Quadratic fit (LSQ) [79]. Whilst shown to have good accuracy this method was observed to have a significant level of systematic noise where the mean output error would vary relative to the position of the peak. This was assumed indicative of a poor fit between the quadratic function and the grating shape. We implemented a technique based using the approximation of a specific type of neural network; the General Regression Neural Network (GRNN). This

approximation was found to be optimal over the LSQ approximation for both simulative and experimental tests.

Our second method was based upon the Centroid Detection Algorithm (CDA) [78]. We found that windowing the sample set around the grating produced optimal accuracy. By treating the CDA as a neural network problem we calculated an optimal architecture for both noise suppression and accuracy. This was further analysed to be equivalent to the CDA algorithm, windowed relative to the Gaussian fit of the grating's reflection. As such we denoted the method as the Gaussian Windowed Centroid Detection Algorithm (GWCDA). This method was found to be optimal over all other methods for both simulative and experimental tests.

Overlapping Gratings Sensor Network

As part of an evaluation of Tactile Sensing methods we envisaged the application of Distributive Tactile Sensing (DTS) methods [98] to extend the operation of traditional edge-filter interrogation [3]. In doing so we created a low-cost scaleable architecture that is inherently environmentally stable and uses very few components.

We named this architecture the Overlapping Gratings Sensor Network, and over some basic proof of principle testing found it to be a very attractive measurement system. Subsequent evaluation with a simplified implementation proved the technique and established the concept of using the behaviour of neural network training with respect to sampling distribution to evaluate the system as a whole, and identify problems.

7.1 Future Work

There is great potential for future work in both these systems.

Firstly with respect to the Gaussian Windowed Centroid Detection Algorithm (GWCDA) future work could focus on the development of a generalised window model for arbitrary grating shapes. Or given the parallel nature of the filter, work could focus on a discrete real-time practical implementation for use with an Arrayed Waveguide Grating (AWG) FBG interrogation scheme [87].

Since this is the only work performed with the OGSN architecture there are huge possibilities for future work. In terms of the architecture work could focus upon the application of genetic algorithms to determine parameters such as sensor position [104, 105], sampling distribution [106], and potentially the OGSN architecture itself.

With respect to applications it is perhaps dynamic systems that offer the greatest potential for utilisation of this technology. Elliott et al. [107] have demonstrated the potential of DTS as a dynamic system measuring load movement on a surface using signal processing. However it the area of structural health monitoring (SHM) [108, 109] that could see the most benefit from OGSN systems. Because of the inherent scalability to the network, coupled its real-time capabilities this topology has direct relevance to acoustic monitoring of structures for damage and fatigue. As a precursor to large scale implementation the four sensor fibre Bragg grating strain gauge rosette [110] would be easily realisable by a fully populated single coupler OGSN.

Chapter 8

Publications

A. S. Main and D. J. Webb. "Low cost FBG based temperature sensing system for turbine generator monitoring". In *In-Fibre Bragg Gratings and Special Fibres.* Institute of Physics, 2005. **(Oral Presentation)** [111]

A. S. Main, B. M. Cowie, and D. J. Webb. "Low cost distributive sensing smart surface". In *18th International Conference on Optical Fiber Sensors*, FA5, 2006 **(Oral Presentation)** [112]

B. M. Cowie, A. S. Main, D. J. Webb, P. N. Brett. "Distributive tactile sensing using fibre Bragg grating sensors". In *Third European Workshop on Optical Fibre Sensors*, volume 6619, pages 66193T–4, Napoli, Italy, July 2007. SPIE. **(Poster Presentation)** [113]

A. S. Main and D. J. Webb, "Windowing and the accuracy of the centroid detection algorithm applied to fibre Bragg grating interrogation", *Optics Communications*, in preparation.

A. S. Main and D. J. Webb, "Novel fibre Bragg grating sensing network for distributive tactile sensing", *Measurement Science and Technology*, in preparation.

Not included in this thesis

T. Allsop, M. Dubov, H. Dobb, A. Main, A. Martinez, K. Kalli, D. J. Webb, I. Bennion. "A comparison of the spectral properties of high temperature annealed long-period gratings inscribed by fs laser, uv, and fusion-arc". In *Reliability of Optical Fiber Components, Devices, Systems, and Networks III*, volume 6193, pages 61930M–9, Strasbourg, France, April 2006. **(Oral Presentation)** [44]

K. T. O'Mahoney, A. S. Main, D. J. Webb, A. Martinez, D. A. Flavin. "Implications of high power losses in IR femtosecond laser inscribed fiber bragg gratings". In *Reliability of Optical Fiber Components, De- vices, Systems, and Networks III*, volume 6193, pages 61930Z–7, Strasbourg, France, April 2006. **(Oral Presentation)** [45]

Bibliography

[1] B. Widrow and M.A. Lehr. 30 years of adaptive neural networks: perceptron, madaline, and backpropagation. *Proceedings of the IEEE*, 78:1415–1442, 1990. ISSN 0018-9219. 9, 43, 65

[2] Gabor Vasarhelyi, Maria Adam, Eva Vazsonyi, Istvan Barsony, and Csaba Ducso. Effects of the elastic cover on tactile sensor arrays. *Sensors and Actuators A: Physical*, 132:245–251, 2006. 10, 77

[3] S.M Melle, K Liu, and R.M Measures. A passive wavelength demodulation system for guided-wave Bragg grating sensors. *IEEE Photonics Technology Letters*, 4:516–518, 1992. 11, 37, 81, 93, 105, 124

[4] A. Othonos and K. Kalli. *Fiber Bragg Gratings: Fundamentals and Applications in Telecommunications and Sensing (Boston, MA: Artech House)*. Artech House, 1999. 16, 20, 26, 33

[5] Y Rao. In-fibre Bragg grating sensors. *Meas. Sci. Technol*, 8(4):355–375, 1997. 16, 20, 35, 36

[6] Byoungho Lee. Review of the present status of optical fiber sensors. *Optical Fiber Technology*, 9:57–79, April 2003. 17, 20

[7] A. D. Kersey, M. A. Davis, H. J. Patrick, M. LeBlanc, K. P. Koo, C. G. Askins, M. A. Putnam, and E. J. Friebele. Fiber grating sensors. *Lightwave Technology, Journal of*, 15:1442–1463, 1997. 17, 20, 36, 37

[8] K Hill, Y Fujii, D Johnson, and B Kawasaki. Photosensitivity in optical fiber waveguides: Application to reflection filter fabrication. *Applied Physics Letters*, 32: 647, 1978. 20

[9] I. Bennion, J. A. R. Williams, L. Zhang, K. Sugden, and N. J. Doran. UV-written in-fibre Bragg gratings. *Optical and Quantum Electronics*, 28:93–135, 1996. 20

[10] T Erdogan. Fiber grating spectra. *Lightwave Technology, Journal of*, 15(8):1277–1294, 1997. 20, 22, 23, 25, 26

[11] A Yariv. Coupled-mode theory for guided-wave optics. *Quantum Electronics, IEEE Journal of*, 9:919–933, 1973. 22

[12] J Sipe, L Poladian, and C Sterke. Propagation through nonuniform grating structures. *J. Opt. Soc. Am. A*, 11(4):1307?1320, 1994. 24, 30

[13] M Yamada and K Sakuda. Analysis of almost-periodic distributed feedback slab waveguides via a fundamental matrix approach. *Appl. Opt*, 26(16):3474?3478, 1987. 25

[14] B. Malo, D. C. Johnson, F. Bilodeau, J. Albert, and K. O. Hill. Single-excimer-pulse writing of fiber gratings by use of a zero-order nulled phase mask: grating spectral response and visualization of index perturbations. *Optics Letters*, 18:1277?1279, 1993. 26

[15] A Martinez, I Khrushchev, and I Bennion. Direct inscription of Bragg gratings in coated fibers by an infrared femtosecond laser. *Optics Letters*, 31:1603–1605, 2006. 26, 33, 34

[16] P.J. Lemaire, R.M. Atkins, V. Mizrahi, and W.A. Reed. High pressure h2 loading as a technique for achieving ultrahigh uv photosensitivity and thermal sensitivity in geo2 doped optical fibres. *Electronics Letters*, 29:1191–1193, 1993. ISSN 0013-5194. 27

[17] T Erdogan, V Mizrahi, P Lemaire, and D Monroe. Decay of ultraviolet-induced fiber Bragg gratings. *Journal of Applied Physics*, 76:73, 1994. 28

[18] H Patrick, S Gilbert, A Lidgard, and M Gallagher. Annealing of Bragg gratings in hydrogen-loaded optical fiber. *Journal of Applied Physics*, 78:2940, 1995. 29

[19] S Baker, H Rourke, V Baker, and D Goodchild. Thermal decay of fiber Bragg gratings written in boron andgermanium codoped silica fiber. *Lightwave Technology, Journal of*, 15:1470–1477, 1997. 29

[20] B. Malo, K.O. Hill, F. Bilodeau, D.C. Johnson, and J. Albert. Point-by-point fabrication of micro-Bragg gratings in photosensitive fibre using single excimer pulse refractive index modification techniques. *Electronics Letters*, 29:1668–1669, 1993. ISSN 0013-5194. 29

[21] A. Martinez, M. Dubov, I. Khrushchev, and I. Bennion. Direct writing of fibre Bragg gratings by femtosecond laser. *Electronics Letters*, 40:1170–1172, 2004. ISSN 0013-5194. 29

[22] G Meltz, W Morey, and W Glenn. Formation of Bragg gratings in optical fibers by a transverse holographic method. *Opt. Lett*, 14(15):823–825, 1989. 29

[23] T Erdogan and J Sipe. Tilted fiber phase gratings. *J. Opt. Soc. Am. A*, 13(8): 296–313, 1996. 30

[24] K. O. Hill, B. Malo, F. Bilodeau, D. C. Johnson, and J. Albert. Bragg gratings fabricated in monomode photosensitive optical fiber by UV exposure through a phase mask. *Applied Physics Letters*, 62:1035, 1993. 30

[25] D.Z Anderson, V Mizrahi, T Erdogan, and A.E White. Production of in-fibre gratings using a diffractive optical element. *Electronics Letters*, 29:566–568, 1993. 30

[26] J Martin and F Ouellette. Novel writing technique of long and highly reflective in-fibre gratings. *Electronics Letters*, 30:811–812, 1994. 30

[27] P. E. Dyer, R. J. Farley, and R. Giedl. Analysis and application of a 0/1 order Talbot interferometer for 193 nm laser grating formation. *Optics Communications*, 129:98–108, August 1996. 32

[28] F Floreani, A Gillooly, L Zhang, I Bennion, X Shu, and K Sugden. A simple method for the fabrication of intrinsically apodized chirped fibre Bragg gratings. *Journal of Optics A: Pure and Applied Optics*, 5(4):S59–S62, 2003. 32

[29] W Loh, M Cole, M Zervas, S Barcelos, and R Laming. Complex grating structures with uniform phase masks based on the moving fiber-scanning beam technique. *Optics Letters*, 20:2051, 1995. 32, 119

[30] A Asseh, H Storoy, B.E Sahlgren, S Sandgren, and R.A.H Stubbe. A writing technique for long fiber Bragg gratings with complex reflectivity profiles. *Lightwave Technology, Journal of*, 15:1419–1423, 1997. 32

[31] I. Petermann, B. Sahlgren, S. Helmfrid, A. T. Friberg, and P. Y. Fonjallaz. Fabrication of advanced fiber Bragg gratings by use of sequential writing with a continuous-wave ultraviolet laser source. *Applied Optics*, 41:1051?1056, 2002. 32, 119

[32] Y Liu, JAR Williams, L Zhang, and I Bennion. Abnormal spectral evolution of fiber Bragg gratings in hydrogenated fibers. *Optics Letters*, 27(8):586–588, 2002. 33

[33] C Wei, C Ye, S James, R Tatam, and P Irving. The influence of hydrogen loading and the fabrication process on the mechanical strength of optical fibre Bragg gratings. *Optical Materials*, 20(4):241–251, Nov 2002. 33

[34] BC Stuart, MD Feit, S Herman, AM Rubenchik, BW Shore, and MD Perry. Nanosecond-to-femtosecond laser-induced breakdown in dielectrics. *Physical Review B*, 53(4):1749–1761, 1996. 33

[35] KM Davis, K Miura, N Sugimoto, and K Hirao. Writing waveguides in glass with a femtosecond laser. *Opt. Lett*, 21(21):1729–1731, 1996. 33

[36] D Homoelle, S Wielandy, AL Gaeta, NF Borrelli, and C Smith. Infrared photosensitivity in silica glasses exposed to femtosecond laser pulses. *Optics Letters*, 24(18): 1311–1313, 1999. 33

[37] S Mihailov, C Smelser, D Grobnic, R Walker, Ping Lu, Huimin Ding, and J Unruh. Bragg gratings written in all-SiO2 and Ge-doped core fibers with 800-nm femtosecond radiation and a phase mask. *Lightwave Technology, Journal of*, 22(1):94 – 100, Jan 2004. 33

[38] David Nikogosyan. Multi-photon high-excitation-energy approach to fibre grating inscription. *Measurement Science and Technology*, 18:R1–R29, 2007. 33

[39] A Martinez, Y Lai, M Dubov, I Khrushchev, and I Bennion. Vector bending sensors based on fiber Bragg gratings inscribed by an infrared femtosecond laser. *Lasers and Electro-Optics, 2005.(CLEO). Conference on*, 3, 2005. 34

[40] Y Lai, A Martinez, I Khrushchev, and I Bennion. Distributed Bragg reflector fiber laser fabricated by femtosecond laser inscription. *Optics Letters*, 31(11):1672–1674, 2006. 34

[41] E Wikszak, J Thomas, J Burghoff, B Ortaç, J Limpert, S Nolte, U Fuchs, and A Tünnermann. Erbium fiber laser based on intracore femtosecond-written fiber Bragg grating. *Optics Letters*, 31(16):2390–2392, 2006. 34

[42] L.B Fu, G.D Marshall, J.A Bolger, P Steinvurzel, E.C Mägi, M.J Withford, and B.J Eggleton. Femtosecond laser writing Bragg gratings in pure silica photonic crystal fibres. *ELECTRONICS LETTERS*, 41(11):638, Jan 2005. doi: 10.1049/el:20051083. 34

[43] A Martinez, IY Khrushchev, and I Bennion. Thermal properties of fibre Bragg gratings inscribed point-by-point by infrared femtosecond laser. *ELECTRONICS LETTERS*, 41(4):176–178, 2005. 34

[44] T. Allsop, M. Dubov, H. Dobb, A. Main, A. Martinez, K. Kalli, D. J. Webb, and I. Bennion. A comparison of the spectral properties of high temperature annealed long-period gratings inscribed by fs laser, UV, and fusion-arc. In *Reliability of Optical Fiber Components, Devices, Systems, and Networks III*, volume 6193, pages 61930M–9, Strasbourg, France, April 2006. SPIE. 34, 127

[45] K. T. O'Mahoney, A. S. Main, D. J. Webb, A. Martinez, and D. A. Flavin. Implications of high power losses in ir femtosecond laser inscribed fiber Bragg gratings. In *Reliability of Optical Fiber Components, Devices, Systems, and Networks III*, volume 6193, pages 61930Z–7, Strasbourg, France, April 2006. SPIE. 34, 127

[46] Kaiming Zhou, Yicheng Lai, Xianfeng Chen, Kate Sugden, Lin Zhang, and Ian Bennion. A refractometer based on a micro-slot in a fiber Bragg grating formed by chemically assisted femtosecond laser processing. *Optics Express*, 15(24):15848, Jan 2007. 34

[47] M.G. Xu, L. Reekie, Y.T. Chow, and J.P. Dakin. Optical in-fibre grating high pressure sensor. *Electronics Letters*, 29:398–399, 1993. ISSN 0013-5194. 35

[48] M.G. Xu, H. Geiger, and J.P. Dakin. Fibre grating pressure sensor with enhanced sensitivity using a glass-bubble housing. *Electronics Letters*, 32:128–129, 1996. ISSN 0013-5194. 35

[49] Boonsong Sutapun, Massood Tabib-Azar, and Alex Kazemi. Pd-coated elastooptic fiber optic Bragg grating sensors for multiplexed hydrogen sensing. *Sensors and Actuators B: Chemical*, 60:27–34, November 1999. 35

[50] A.D. Kersey, K.L. Dorsey, and A. Dandridge. Demonstration of an eight-element time-division multiplexed interferometric fibre sensor array. *Electronics Letters*, 24: 689–691, 1988. ISSN 0013-5194. 36

[51] David J. F. Cooper, Trent Coroy, and Peter W. E. Smith. Time-division multiplexing of large serial fiber-optic Bragg grating sensor arrays. *Applied Optics*, 40: 2643–2654, 2001. 36

[52] David J. F. Cooper and Peter W. E. Smith. Simple high-performance method for large-scale time division multiplexing of fibre Bragg grating sensors. *Measurement Science and Technology*, 14:965–974, 2003. ISSN 0957-0233. 36

[53] G.D. Lloyd, L.A. Everall, K. Sugden, and I. Bennion. Resonant cavity time-division-multiplexed fiber Bragg grating sensor interrogator. *Photonics Technology Letters, IEEE*, 16:2323–2325, 2004. ISSN 1041-1135. 36

[54] A.D. Kersey, A. Dandridge, and M.A. Davis. Code-division multiplexed interferometric array with phase noise reduction and low crosstalk. In *Optical Fiber Sensors Conference, 1992. 8th*, pages 266–269, 1992. 36

[55] S Dyer, P Williams, R Espejo, J Kofler, and S Etzel. Fundamental limits in fiber Bragg grating peak wavelength measurements (invited paper). *Proceedings of SPIE*, 5855:88, 2005. 37, 52, 54, 59, 63

[56] M. Volanthen, H. Geiger, M.G. Xu, and J.P. Dakin. Simultaneous monitoring of multiple fibre gratings with a single acousto-optic tunable filter. *Electronics Letters*, 32:1228–1229, 1996. ISSN 0013-5194. 37

[57] MA Davis and AD Kersey. Matched-filter interrogation technique for fiber Bragg grating arrays. *Electronics Letters*, 31(10):822 – 823, 1995. 37

[58] R Fallon, L Zhang, and L Everall. All-fibre optical sensing system: Bragg grating sensor interrogated by a long-period grating. *Measurement Science and Technology*, 9(12):1969–73, 1998. 37, 105

[59] R Fallon, L Zhang, and I Bennion. Multiplexed identical broad-band-chirped grating interrogationsystem for large-strain sensing applications. *Photonics Technology Letters, IEEE*, 9(12):1616–1618, 1997. 38, 105

[60] D. J. Webb, M. W. Hathaway, D. A. Jackson, S. Jones, L. Zhang, and I. Bennion. First in-vivo trials of a fiber Bragg grating based temperature profiling system. *Journal of Biomedical Optics*, 5:45, 2000. 38, 53

[61] A. G. Simpson, K. Zhou, L. Zhang, L. Everall, and I. Bennion. Optical sensor interrogation with a blazed fiber Bragg grating and a charge-coupled device linear array. *Applied Optics*, 43(1):33–40, 2004. 38, 53

[62] C. Jauregui and J. M. Lopez-Higuera. Interrogation of fibre Bragg gratings with a tilted fibre Bragg grating. *Measurement Science and Technology*, 15(8):1596–1600, 2004. 38, 53

[63] C. K. Madsen, J. Wagener, T. A. Strasser, D. Muehlner, M. A. Milbrodt, E. J. Laskowski, and J. DeMarco. Planar waveguide optical spectrum analyzer using a UV-induced grating. *Selected Topics in Quantum Electronics, IEEE Journal of*, 4 (6):925–929, 1998. 39

[64] C. M. Bishop. *Pattern recognition and machine learning.* Springer, 2006. 41, 104, 121

[65] D. MacKay. *Bayesian Methods for Adaptive Models.* PhD thesis, California Institute of Technology, 1992. 42, 48, 98

[66] C. M. Bishop. *Neural Networks for Pattern Recognition.* Oxford University Press, 1995. 43, 44, 45, 49, 87, 97

[67] W. H. Press. *Numerical Recipes in C: the art of scientific computing.* Cambridge University Press, 1992. 43, 58

[68] S. Haykin. *Neural Networks: A Comprehensive Foundation.* Prentice Hall PTR Upper Saddle River, NJ, USA, 1994. 47, 121

[69] M. F. Møller. A scaled conjugate gradient algorithm for fast supervised learning. *Neural Networks*, 6:525–533, 1993. 48

[70] M Hagan and M Menhaj. Training feedforward networks with the Marquardt algorithm. *Neural Networks, IEEE Transactions on*, 5:989–993, 1994. 48

[71] C. M. Bishop. Training with noise is equivalent to Tikhonov regularization. *Neural Computation*, 7:108–116, 1995. 48, 98

[72] S Chen, C.F.N Cowan, and P.M Grant. Orthogonal least squares learning algorithm for radial basis function networks. *Neural Networks, IEEE Transactions on*, 2:302–309, 1991. 49

[73] M. J. L. Orr. Regularisation in the selection of radial basis function centres. *Neural Computation*, 7(3):606–623, 1995. 49

[74] D Specht. A general regression neural network. *Neural Networks, IEEE Transactions on*, 2:568–576, 1991. 50, 61

[75] A. Zaknich. Introduction to the modified probabilistic neural network for general signal processing applications. *Signal Processing, IEEE Transactions on*, 46:1980–1990, 1998. ISSN 1053-587X. 50, 61

[76] A. Zaknich. *Neural Networks for Intelligent Signal Processing.* World Scientific, 2003. 50, 61

[77] I. Nabney and C. Bishop. Netlab toolbox release 3.3. URL `http://www.ncrg.aston.ac.uk/netlab/`. 50, 87

[78] C. G. Askins, M. A. Putnam, and E. J. Friebele. Instrumentation for interrogating many-element fiber Bragg grating arrays. *Proc. SPIE*, 2444:257–266, 1995. 51, 54, 56, 124

[79] A Ezbiri, S Kanellopoulos, and V Handerek. High resolution instrumentation system for fibre-Bragg grating aerospace sensors. *Optics Communications*, 150(1-6):43–48, 1998. 51, 54, 58, 59, 123

[80] T Zeh, H Schweizer, A Meixner, A Purde, and A Koch. Enhancement of detection accuracy of fiber Bragg grating sensors. *Proceedings of SPIE*, 5502:540, 2004. 54

[81] C Caucheteur, K Chah, F Lhomme, M Blondel, and P Megret. Autocorrelation demodulation technique for fiber Bragg grating sensor. *Photonics Technology Letters, IEEE*, 16:2320–2322, 2004. 54

[82] C Huang, W Jing, K Liu, Y Zhang, and G Peng. Demodulation of fiber Bragg grating sensor using cross-correlation algorithm. *Photonics Technology Letters, IEEE*, 19:707, 2007. 54

[83] C Chan, C Shi, W Jin, and D Wang. Improving the wavelength detection accuracy of FBG sensors using an ADALINE network. *Photonics Technology Letters, IEEE*, 15(8):1126–1128, 2003. 54

[84] A Paterno, J Silva, M Milczewski, L Arruda, and H Kalinowski. Radial-basis function network for the approximation of FBG sensor spectra with distorted peaks. *Measurement Science and Technology*, 17(5):1039–1045, 2006. 54, 60

[85] B Cowie, T Allsop, J Williams, D Webb, I Bennion, and M Fisher. An optical fiber Bragg grating tactile sensor. *Proceedings of SPIE*, 6585:65850I, 2007. 56, 91

[86] G.M.H. Flockhart, W.N. MacPherson, J.S. Barton, J.D.C. Jones, L. Zhang, and I. Bennion. Departure from linearity of fibre Bragg grating temperature coefficients. In *Optical Fiber Sensors Conference Technical Digest, 2002. OFS 2002, 15th*, pages 75–78 vol.1, 2002. 72

[87] Y Sano and T Yoshino. Fast optical wavelength interrogator employing arrayed waveguide grating for distributed fiber Bragg grating sensors. *Lightwave Technology, Journal of*, 21:132–139, 2003. 75, 125

[88] M Lee and H Nicholls. Tactile sensing for mechatronics - a state of the art survey. *Mechatronics*, 9(1):1–31, 1999. 76, 77

[89] M Lee. Tactile sensing: New directions, new challenges. *The International Journal of Robotics Research*, 19:636, 2000. 77

[90] M Shimojo. Mechanical filtering effect of elastic cover for tactile sensor. *Robotics and Automation, IEEE Transactions on*, 13:128–132, 1997. 78

[91] R Fearing and J Hollerbach. Basic solid mechanics for tactile sensing. In *Proceedings of the 1984 IEEE International Conference on Robotics and Automation*, volume 1, pages 266– 275, 1984. 78

[92] R.E Ellis and M Qin. Singular-value and finite-element analysis of tactile shape recognition. In *Proceedings of the 1994 IEEE International Conference on Robotics and Automation*, pages 2529–2535 vol.3, 1994. 78

[93] E.J. Nicolson and R.S. Fearing. The reliability of curvature estimates from linear elastic tactile sensors. In *Proceedings of the 1995 IEEE International Conference on Robotics and Automation*, volume 1, pages 1126–1133 vol.1, 1995. 78, 79, 94

[94] G Canepa, M Morabito, D Rossi, A Caiti, and T Parisini. Shape estimation with tactile sensors: a radial basis functions approach. In *Proceedings of the 31st IEEE International Conference on Decision and Control*, pages 3493–3495 vol.4, 1992. 78

[95] G Canepa, M Morabito, D Rossi, A Caiti, and T Parisini. Shape from touch by a neural net. In *Proceedings of the 1992 IEEE International Conference on Robotics and Automation*, pages 2075–2080 vol.3, 1992. 78

[96] K Tho, S Swaddiwudhipong, Z Liu, and J Hua. Artificial neural network model for material characterization by indentation. *Modelling and Simulation in Materials Science and Engineering*, 12:1055–1062, 2004. 78

[97] A.M Gillooly, L Zhang, and I Bennion. Quasi-distributed strain sensor incorporating a chirped Moiré fiber Bragg grating. *Photonics Technology Letters, IEEE*, 17:444–446, 2005. 78

[98] R Ellis, S Ganeshan, and S Lederman. A tactile sensor based on thin-plate deformation. *Robotica*, 12:343–351, 1994. 78, 79, 93, 124

[99] P Brett and R Stone. A technique for measuring contact force distribution in minimally invasive surgical procedures. *Proceedings of the Institution of Mechanical Engineers, Part H: Journal of Engineering in Medicine*, 211(4):309–316, 1997. 79

[100] P Brett and Z Li. A tactile sensing surface for artificial neural network based automatic recognition of the contact force position. *Proceedings of the Institution of Mechanical Engineers, Part I: Journal of Systems and Control Engineering*, 214 (3):207–215, 2000. 79

[101] B Cowie, D Webb, B Tam, P Slack, and P Brett. Fibre Bragg grating sensors for distributive tactile sensing. *Measurement Science and Technology*, 18(1):138–146, 2007. 79, 80, 87, 91

[102] R.W. Fallon, L. Zhang, and I. Bennion. Multiplexed identical broad-band-chirped grating interrogation system for large-strain sensing applications. *Photonics Technology Letters, IEEE*, 9:1616–1618, 1997. ISSN 1041-1135. 80

[103] F Beer, J Dewolf, and E Johnston. *Mechanics of materials.* McGraw Hill Higher Education, 2003. 95

[104] P Tongpadungrod, T Rhys, and P Brett. An approach to optimise the critical sensor locations in one-dimensional novel distributive tactile surface to maximise performance. *Sensors and Actuators A: Physical*, 105(1):47–54, 2003. 121, 125

[105] H Guo, L Zhang, L Zhang, and J Zhou. Optimal placement of sensors for structural health monitoring using improved genetic algorithms. *Smart Materials and Structures*, 13(3):528–534, 2004. 121, 125

[106] A.-M Cretu, E.M Petriu, and G.G Patry. Neural network-based adaptive sampling of 3D object surface elastic properties. In *Instrumentation and Measurement Technology Conference, 2004. IMTC 04. Proceedings of the 21st IEEE*, volume 1, pages 285– 290 Vol.1, 2004. 121, 125

[107] M Elliott, X Ma, and P Brett. Tracking the position of an unknown moving load along a plate using the distributive sensing method. *Sensors and Actuators A: Physical*, 138:28–36, 2007. 121, 125

[108] G. Zhou and L. M. Sim. Damage detection and assessment in fibre-reinforced composite structures with embedded fibre optic sensors-review. *Smart Materials and Structures*, 11:925–939, 2002. 121, 125

[109] D. C. Betz, G. Thursby, B. Culshaw, and W. J. Staszewski. Acousto-ultrasonic sensing using fiber Bragg gratings. *Smart Materials and Structures*, 12:122–128, 2003. 121, 125

[110] D.C. Betz, G. Thursby, B. Culshaw, and W.J. Staszewski. Advanced layout of a fiber Bragg grating strain gauge rosette. *Lightwave Technology, Journal of*, 24: 1019–1026, 2006. ISSN 0733-8724. 121, 125

[111] A S Main and D J Webb. Low cost FBG based temperature sensing system for turbine generator monitoring. In *In-Fibre Bragg Gratings and Special Fibres*. Institute of Physics, 2005. 126

[112] A S Main, B M Cowie, and D J Webb. Low cost distributive sensing smart surface. In *18th International Conference on Optical Fiber Sensors*, 2006. 126

[113] B. M. Cowie, A. S. Main, D. J. Webb, and P. N. Brett. Distributive tactile sensing using fibre Bragg grating sensors. In *Third European Workshop on Optical Fibre Sensors*, volume 6619, pages 66193T–4, Napoli, Italy, July 2007. SPIE. 126